POLITECNICO DI MILANO

School of Civil, Environmental and Land Management

Engineering Master of Science Degree in Civil

Wind Tunnel Experimental Campaign to Validate Aerodynamic Non-linearities in Long-Span Bridges

Supervisor:

Prof. Daniele Rocchi

Co-Supervisors:

Ing. Tommasso Argentini

Ing. Simone Omarini

Dissertation by:

Luis Fernando Abello

895595

Academic year 2019/2020

Abstract

The need to overcome obstacles on very long distances typically implies the design of streamlined bridge decks. The slenderness and lightness that characterize these structures make them sensitive to dynamic problems and special care must be put in the design against the wind action. Dealing with this aspect, many difficulties are encountered in the wind description and in the computation of the bridge response, making the definition of reliable numerical codes a fundamental issue.

Nowadays, numerical models for the design of long-span bridges are mainly linearized models carried out both in frequency and time domain. However, some non-linear models can be found in the time domain. These models are, in fact, more appropriate to describe all the complex aspects related to the aerodynamic forces generated by the high fluctuations of the angle of attack. Unfortunately, such models are strongly limited by their applicability range since they would be more appropriate only to describe the non-linearities associated with the low frequency fluctuations of the incoming wind turbulence. An attempt to also consider the non-linear contributions of the high frequencies is presented in this thesis where a new numerical approach based on the definition of rheological models has been proposed.

Specific wind tunnel tests have been carried out in order to better understand the non-linearities present in the definition of aerodynamic forces. The placing of a scaled train over a rigid sectional model deck allows us to magnify these non-linear effects, thus enabling us to propose an alternative numerical model able to describe these non-linearities.

The wind-tunnel tests were performed at Politecnico di Milano and were part of an international benchmark project conducted by the Politecnico di Milano and promoted by the International Association for Bridge and Structural Engineering (IABSE).

Table of Contents

List of Tables .....

List of Figures .....

Introduction **1**

1 Wind Actions on Bridges **4**

1.1 Introduction 4

1.1.1 Main Aspects of wind-bridge interaction 5

1.2 Definition of Aerodynamic Forces 9

1.2.1 Quasi-steady Theory 9

1.2.2 Linearized theory 12

1.2.3 Flutter derivatives and aerodynamic admittance functions 16

1.3 Band superposition approach 20

2 Wind Tunnel Testing **26**

2.1 Introduction 26

2.2 Wind Tunnel Laboratory (GVPM) 26

2.3 Experimental Setup 28

2.3.1 Instrumentation for Wind Flow Measurements 30

2.3.2 Instrumentation for Model Motion Measurements 32

2.3.3 Forcing System 34

2.3.4 Instrumentation for force measurements 35

2.4 Wind Tunnel Tests 38

2.4.1 Static tests 38

2.4.2 Dynamic Tests 43

2.4.3 Suspended model tests 59

2.4.4 Forced motion tests 64

3 Experimental Evidence of Non-Linearities 67

3.1 Introduction 67

3.2 Aerodynamic coefficients 68

3.3 Forced Motion Tests 79

3.4 New non-linear rheological model 92

4 Non-linear analytical approach 94

4.1 Introduction 94

4.2 Non-linear formulation 94

4.3 Rheological model approach 98

A. State-space formulation of the problem 108

1. Self-excited forces 108

2. Buffeting forces 115

Bibliography.....120

List of Tables

Table 2.1. QSTC coefficients to which the flutter derivatives converge at high V^*. 54

Table 2.2. QSTC values to which the flutter derivatives converge at high V^*. 54

Table 2.3. Lift flutter derivatives at V^*=25. 54

Table 2.4. Moment flutter derivatives at V^*=25. 55

Table 2.5. Modal parameters of the two configurations of the elastically suspended sectional model. 61

Table 2.6. (Continuation) Forced motion tests conducted over *configuration 1*. 66

Table 2.7. Forced motion tests conducted over *configuration 2*. 66

Table 3.1. QSTC coefficients to which the flutter derivatives converge at high V^*. 70

Table 3.2. Modal parameters of the two configurations of the elastically suspended BB3NT. 80

Table 3.3. Forced motion tests conducted over BB3NT. 81

List of Figures

Figure 1.1. The Yavuz Sultan Selim Bridge, or Third Bosphorus Bridge (BB3). 4

Figure 1.2. Aerodynamic forces in a generic deck section. 5

Figure 1.3. Wind turbulence components. 7

Figure 1.4. Aerodynamic forces on a generic deck section and its sign conventions. 9

Figure 1.5. Elastically suspended deck section. 11

Figure 1.6. Flutter derivatives $a2*$ (a) and $a3*$ (b) of the BB3 section without a train and of a flat plate (Theodorsen's theory) vs. V^* for 5 angles of attack (A. Pellegri 2017) 21

Figure 1.7. Band superposition approach: Simulation flow chart. 25

Figure 2.1. Overview of the flow circuit (http://www.wintunnel.polimi.it/facility n.d.). 27

Figure 2.2. Spires and roughness elements for the simulation of the atmospheric boundary layer (http://www.wintunnel.polimi.it/facility n.d.). 28

Figure 2.3. The sectional model supported on oil dynamic actuators in the Boundary Layer Test Section. 29

Figure 2.4. The sectional model suspended by means of steel cables on the Boundary Layer Test Section. 29

Figure 2.5. Pitot-static tube. 30

Figure 2.6. Installed Pitot tube. 31

Figure 2.7. Schematic diagram of a Cobra Probe. 31

Figure 2.8. Installed cobra probes, displayed inside the 4 green circles. 32

Figure 2.9. Lasers transducers below the deck sectional model. 33

Figure 2.10. Calibration of the laser transducers below pressure ring #3. 34

Figure 2.11. Implemented active turbulence generator: (a) array of 10 NACA0012 profile airfoils; (b) low frequency turbulence is generated in the incoming flow. 35

Figure 2.12. (a) Surface pressure distribution ; (b) Shear stress distribution ; (c) Lift Force F_L and drag force F_D over an airfoil profile 36
Figure 2.13. Sign convention of pressure and shear stress on a point of a body surface. 37
Figure 2.14. Aerodynamic forces, local and global reference systems. 39
Figure 2.15. Drag coefficient measurements at different mean wind speeds. 40
Figure 2.16. Lift coefficient measurements at different mean wind speeds. 41
Figure 2.17. Moment coefficient measurements at different mean wind speeds. 41
Figure 2.18. C_D, C_L and C_M at the Third Bosphorus Bridge deck sectional model with a train. . 42
Figure 2.19. K_D, K_L and K_M at the Third Bosphorus Bridge deck sectional model with a train. 42
Figure 2.20. Procedure to define the aerodynamic transfer functions for the z d.o.f. 45
Figure 2.21. Procedure to define the aerodynamic transfer functions for the θ d.o.f. 47
Figure 2.22. Polimi moment flutter derivative $a1*$. 48
Figure 2.23. Polimi moment flutter derivative $a2*$. 48
Figure 2.24. Polimi moment flutter derivative $a3*$. 49
Figure 2.25. Polimi moment flutter derivative $a4*$. 49
Figure 2.26. Polimi lift flutter derivative $h1*$. 50
Figure 2.27. Polimi lift flutter derivative $h2*$. 50
Figure 2.28. Polimi lift flutter derivative $h3*$. 51
Figure 2.29. Polimi lift flutter derivative $h4*$. 51
Figure 2.30. B_{1z}/B as a function of V^*. 52
Figure 2.31. $B_{1\theta}/B$ as a function of V^*. 53
Figure 2.32. Procedure to define the aerodynamic admittance functions 56
Figure 2.33. Vertical aerodynamic admittance function χzw; amplitude and phase. 57
Figure 2.34. Torsional aerodynamic admittance function $\chi\theta w$; amplitude and phase. 58
Figure 2.35. Suspended sectional model; the springs are observed attached to the steel cables. . 59
Figure 2.36. *Configuration 1:* damping ratios as a function of the incoming wind speed 61
Figure 2.37. *Configuration 1*: natural frequencies as a function of the incoming wind speed 62
Figure 2.38. *Configuration 2*: Damping ratios as a function of the incoming wind speed. 62

Figure 2.39. *Configuration 2*: Natural frequencies as a function of the incoming wind speed. 63
Figure 2.40. Harmonic oscillating wind velocity generated by an active turbulence generator. ..65
Figure 3.1. Static aerodynamic coefficients of the BB3 sectional models with a train and without a train. 68
Figure 3.2. Static aerodynamic coefficients derivatives of the BB3 sectional models with a train and without a train. 69
Figure 3.3 $a1*$ of the BB3 with a train and without it. 71
Figure 3.4 $a2*$ of the BB3 with a train and without it. 71
Figure 3.5 $a3*$ of the BB3 with a train and without it. 72
Figure 3.6 $a4*$ of the BB3 with a train and without it. 72
Figure 3.7 $h1*$ of the BB3 with a train and without it. 73
Figure 3.8 $h2*$ of the BB3 with a train and without it. 73
Figure 3.9 $h3*$ of the BB3 with a train and without it. 74
Figure 3.10 $h4*$ of the BB3 with a train and without it. 74
Figure 3.11. Modulus of *L-z* transfer function of the BB3 section with a train and without it. ..76
Figure 3.12. Modulus of *L-θ* transfer function of the BB3 section with a train and without it. ..76
Figure 3.13. Modulus of *M-z* transfer function of the BB3 section with a train and without it. ..77
Figure 3.14. Modulus of *M-θ* transfer function of the BB3 section with a train and without it. 77
Figure 3.15. Amplitude of Lift admittance function for the BB3 section with a train and without it. 78
Figure 3.16. Amplitude of Moment admittance function for the BB3 section with a train and without it. 79
Figure 3.17. Incoming wind turbulence; tests NT-1 and 1-1. 82
Figure 3.18. α_{LF}, z_{HF}, and θ_{HF}; tests NT-1 and 1-1. 83
Figure 3.19. $C_{L,LF}$, and $C_{M,LF}$; tests NT-1 and 1-1. 83
Figure 3.20. Incoming wind turbulence; tests NT-2 and 1-2. 85
Figure 3.21. α_{LF}, z_{HF}, and θ_{HF}; tests NT-2 and 1-2. 85
Figure 3.22. $C_{L,LF}$, and $C_{M,LF}$; tests NT-2 and 1-2. 86

Figure 3.23. Incoming wind turbulence; tests NT-3 and 1-3. 87

Figure 3.24. α_{LF}, z_{HF}, and θ_{HF}; tests NT-3 and 1-3. 88

Figure 3.25. $C_{L,LF}$, and $C_{M,LF}$; tests NT-3 and 1-3. 88

Figure 3.26. Incoming wind turbulence; tests NT-4 and 2-1. 90

Figure 3.27. α_{LF}, z_{HF}, and θ_{HF}; tests NT-4 and 2-1. 90

Figure 3.28. $C_{L,LF}$, and $C_{M,LF}$; tests NT-4 and 2-1. 91

Figure 4.1. Rheological models: motion induced forces left side; turbulence induced forces right side 99

Introduction

The study of wind action on long-span bridges represents a difficult task due to various aspects both related to the complexity of the wind-structure interaction and to the random nature of the wind phenomena. The high slenderness that characterizes these structures makes them very sensitive to *wind buffeting* dynamic action that might induce large oscillations in the response of the bridge. These significant bridge motions can even be the cause of the fluid-structure interaction phenomena, referred to as *aeroelastic phenomena*. These effects occur when the motion – displacements and velocities - of the considered structure is such as to modify, in a significant way, the flow field and the pressure induced by the wind. Aeroelasticity might also introduce energy in the system, decreasing the overall stiffness and/or damping of the structure thus producing critical conditions of incipient instability.

Various methods for buffeting analysis of long-span bridges have been developed in the last decades both in frequency (A. Jain 1996), (N.N. Minh 1999) and time domain (X. Chen 2003), (S. B. G. Diana 11-15 July 2005), (D. R. G. Diana 2013). However, universities and companies interested in the study of these problems have written their own in-house codes without any information from reliable databases. In absence of a direct numerical comparison, the validation of numerical methods represents a crucial problem. Many difficulties are in fact encountered due to the lack of exhaustive full-scale measurements on existing bridges and to the complexity in the scaling of full aeroelastic models in wind tunnel tests. Moreover, it must be considered that these validation techniques present high financial costs. Under this context, a common interest in the definition of reliable numerical standards for bridge buffeting analysis has spread among the wind engineering community at the global level. Recently, in November 2016, the International Association of Bridge and Structural Engineering (IABSE) has launched an international benchmark project in this field. Many participants – including universities and engineering companies – joined in, demonstrating the great amount of interest in this topic. Models based on

different methodologies have been gathered by the work group members. The presented codes work either in the time or in the frequency domain. Politecnico di Milano (PoliMi; Milan, Italy) participates in the project as leader member nominating professor G. Diana as chairman of the work group. Historically, PoliMi has focused on the definition of time domain methods (F. R. G. Diana 2008), (D. R. G. Diana 2010) able to capture the non-linearities connected to wind-bridge interaction. Considering this scenario, this thesis studies the experimental evidence of such non-linearities, and proposes a new numerical model based on these results intended to be an alternative to the one currently present in the PoliMi database.

What is intended in this thesis is to study the significant effects of non-linearities through an experimental campaign of a modified sectional model of an actual bridge. An alternative model that is an extension of the current band superposition method (D. R. G. Diana 2013) is proposed. The analytical formulation of the new model is given in a linearized context. The rheological models (RM) able to describe the transfer functions of self-excited and buffeting forces in the time domain are explained. With this new model, the response of the deck is obtained by means of a "one-shot" integration able to describe the static deflection, the low frequency (LF) response, and the high frequency (HF) response. In brief, the following aspects are considered:

- Definition of a non-linear QST able to describe the LF deck response.
- Definition of the RM linearized contributions – for both flutter derivatives and admittance functions – able to describe the HF response. In this case, the RM is provided with a new formulation since the QST is already considered.
- The HF response is modulated by the LF one, avoiding the direct superposition of the two.

The main advantage of the new numerical method consists in that a band separation of the wind excitation into LF and HF components (and the response of the deck to each input frequency band) is avoided; and that the non-linearities are intended to be captured correctly.

Chapter 1 presents the general background and the theoretical framework which are at the base of the problem of wind actions on bridges. The aerodynamic forces are, in fact, complex to model as they show a dependency on the deck motion ($\underline{x}, \underline{\dot{x}}$), the wind angle of attack (α) and on the reduced velocity (V^*):

$$\underline{F_a} = \underline{F_a}(\underline{x}, \underline{\dot{x}}, \alpha, V^*)$$

The identification of the functions that define the aerodynamic forces requires a series of specific wind tunnel tests. Since the aerodynamic forces are defined at a sectional level, a bridge deck rigid sectional model is employed. A previous experimental campaign (A. Pellegri 2017) studied the aerodynamic behavior of the deck sectional model of the Yavuz Sultan Selim Bridge, also known as the Third Bosphorus Bridge (BB3). Since the non-linearities of the aerodynamic forces are studied in this thesis, an obstacle shaped as a scaled train was added to the BB3 sectional model in order to move away from a stream-lined body to a resemble a bluff body. As it will be studied in **Chapter 3**, the presence of the scaled train leads to an increased non-linear relationship between $\underline{F_a}$ and α, reason for which a new numerical model that accounts for these non-linearities is needed. **Chapter 3** shows the experimental setup, executed in the PoliMi wind tunnel facility (http://www.wintunnel.polimi.it/facility n.d.) and tests that allow for the aerodynamic characterization of the BB3 sectional model with a train.

Finally, some general considerations are also provided as possible guidelines for future analyses.

Chapter 1

Wind Actions on Bridges

1.1 Introduction

In this first chapter, an overview of the definition of the non-linear aerodynamic forces on a generic bridge section is presented. Likewise, the flutter derivatives and aerodynamic admittance functions notations are given. Reference is made to long-span bridges, which are the object of study of this this dissertation, and which are slender structures prone to receive a strong impact of wind action. Figure 1.1 displays the Yavuz Sultan Selim Bridge or Third Bosphorus Bridge, whose cross section is studied in the present thesis.

Figure 1.1. The Yavuz Sultan Selim Bridge, or Third Bosphorus Bridge (BB3).

1.1.1 Main Aspects of wind-bridge interaction

In order to understand the different problems related to the wind action on bridges, it is necessary to define the aerodynamic forces. When a 3D structure is exposed to an air flow, three force and three moment components can be generally considered. However, since bridges are extended only in one predominant direction, the primary concern regards its behavior when wind comes perpendicular to its longitudinal axis. In consequence, the 6 aerodynamic actions are reduced to 3 essential actions: lift force (F_L), drag force (F_D) and pitching moment (M) which are depicted in Figure 1.2.

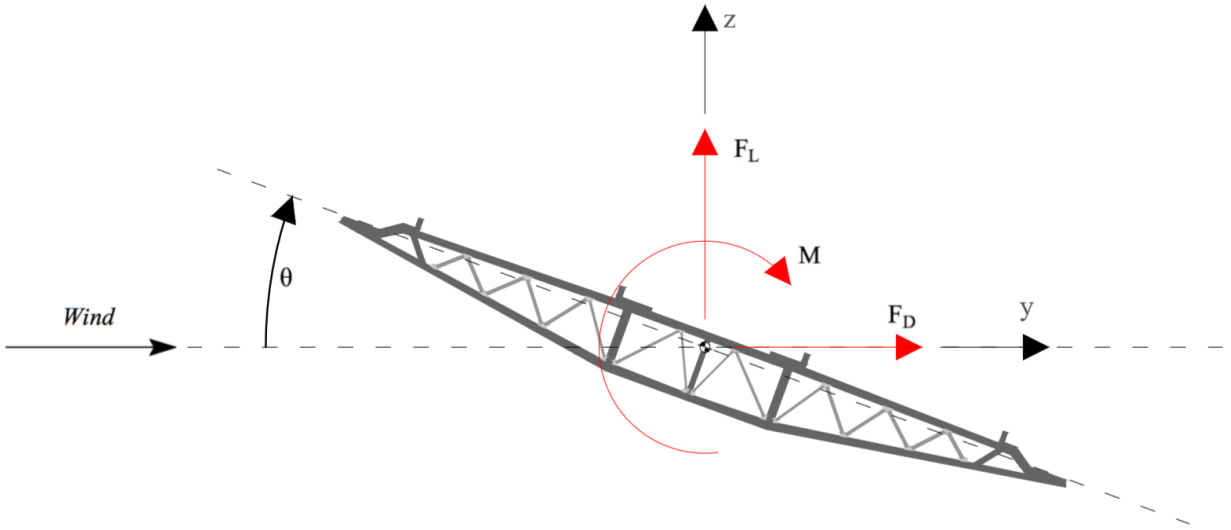

Figure 1.2. Aerodynamic forces in a generic deck section.

The most sensitive part of the bridge to the wind action is its deck. Both the static and dynamic behavior of the bridge actually depend upon the deck aerodynamics The aerodynamic forces to the generic bridge section, reported in Figure 1.2, are complex to model as they show a dependence on the deck motion ($\underline{x}, \underline{\dot{x}}$), the wind angle of attack (α) and on the reduced velocity (V^*): (F. C. G. Diana 1991)

$$\underline{F_{aero}} = \underline{F_{aero}}(\underline{x}, \underline{\dot{x}}, \alpha, V^*) \tag{1-1}$$

The reduced velocity V^* and the angle of attack α are the main keywords to understand the wind interaction, and are described in the following:

- The reduced velocity is defined as:

$$V^* = \frac{V}{fB} \tag{1-2}$$

It represents the ratio between the period $T = 1/f$ associated to the deck's oscillation and the time B/V needed by a fluid particle to move through the deck width B. A conjugate parameter can be defined as the inverse of the reduced velocity V^* called the reduced frequency f^*:

$$f^* = \frac{fB}{V} \tag{1-3}$$

The frequency f in the reduced frequency expression can also represent (in case that the turbulence effect is considered) the frequency of fluctuation of the wind turbulence spectrum.

- The angle of attack is defined with respect to a reference axis (Figure 1.4) as:

$$\alpha = \theta + \psi = \theta + \tan^{-1}\left(\frac{w - \dot{z} - B_1\dot{\theta}}{V + u - \dot{y}}\right) \tag{1-4}$$

It represents the angle between the incoming flow and the deck's position. If small displacements and velocities (of the deck) are considered, equation (1-4) is linearized as:

$$\alpha = \theta + \psi = \theta + \frac{w - \dot{z} - B_1\dot{\theta}}{V + u - \dot{y}} \tag{1-5}$$

B_1 is furtherly defined.

Problems related to the wind action on a bridge can be distinguished into static and dynamic:

- Static problems are related to the static loads exerted by the average wind speed. Such loads are function of the angle of attack α.
- Dynamic problems are related to the turbulence of the incoming wind and to the aerodynamic forces (equation (1-1)) and is also referred to as the aeroelastic problem.

Static Problem

The average wind speed produces a static load that acts on all the components of the bridge. For very long bridges, the load applied on the deck is the most important. In the case of suspended bridges, the loads on the deck are transferred through the hangers to the main cables and to the top of the towers, thus producing a very high bending moment that has a strong impact on the tower and on the overall bridge design. In consequence, drag on the deck is one of the parameters that must be minimized for long-span bridges.

For the sake of the analysis, the crucial aspect of the static problem stands in the definition of the configuration of static equilibrium, around which it is possible to linearize the aerodynamic forces. In practice, what really matters is the static rotation of the deck θ that determines the aerodynamic parameters that must be used to describe the aeroelastic phenomena and the forces due to the turbulence of the incoming wind.

Aeroelastic Problems

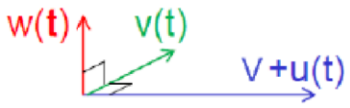

Figure 1.3. Wind turbulence components.

The incoming wind is characterized by turbulent components in three directions, *u(t)*, *v(t)* and *w(t)* (Figure 1.3), to be added to the average wind velocity . Equation (1-5) shows that turbulence components have an impact on the definition of the wind angle of attack and consequently on the aerodynamic forces, that, therefore, change randomly in time. This variation of the aerodynamic forces produces a bridge motion induced by turbulence, called *buffeting*. If the deck or any part of the bridge is moving with a given velocity in the wind flow, the forces applied to the body are functions of the relative velocity V_{rel} of the incoming wind with respect to the body and the same expressions can be applied introducing V_{rel} instead of V.

As observed in equation (1-4) and in Figure 1.4, the motion of the bridge and its position have an effect on the angle of attack α. More specifically, the rotation of the deck θ and the deck velocities $\dot{z}$ and $\dot{\theta}$ concur in the definition of α. The body motion has therefore an impact on the aerodynamic forces. Depending on the shape of the deck, if the motion-dependent - also called self-excited - aerodynamic forces act in favor of the motion, they introduce energy in the system and the oscillations magnitude is amplified. In other words, in such situation the bridge becomes unstable. Different kinds of instability can be identified: one degree of freedom instability in the vertical or torsional mode, or two degrees of freedom instability, which results from the coupling of vertical and torsional motions. The second type of instability is also known as *flutter instability*.

As it will be discussed in Section 1.2, self-excited forces can be seen as equivalent damping and stiffness terms that modify the structural properties of the bridge. Typically, long-span bridges behave in the following way:

- At zero wind speed the overall damping is due only to the structural part (usually structural damping assumes values of about 3-5‰).
- As the wind speed increases, the contribution of the aerodynamic forces becomes very important and the overall damping becomes slightly higher.
- A further increase in wind speed causes a reduction in the overall damping. The wind speed at which the overall damping becomes negative is defined as the flutter velocity.

Section 2.4.3 studies the above behavior for the cross section of the BB3 with a scaled train, which is the object of study of this thesis.

The prediction of the buffeting response to turbulent wind is generally secondary to the question of aerodynamic stability. However, when the bridge is proved to be stable, the bridge response to wind gusts is important for the design of the superstructure and the assessment of the user comfort by predicting the acceleration levels. Moreover, the large vibrations reached by the structure may give rise to fatigue problems. Vibration amplitudes associated with buffeting can be controlled by increasing the aerodynamic damping or equivalently, by increasing the stability of the bridge.

From this point of view, it is important to have a high critical flutter velocity not only to be conservative on stability conditions, but also to increase the aerodynamic damping so as to reduce the turbulence-induced motions.

1.2 Definition of Aerodynamic Forces

Different analytical approaches are available to model the aerodynamic behavior of bridges. In the following, reference is made to a single isolated deck section of length L with three degrees of freedom: the horizontal displacement y, the vertical displacement z, and the rotation θ. An illustration of the problem is depicted in Figure 1.4.

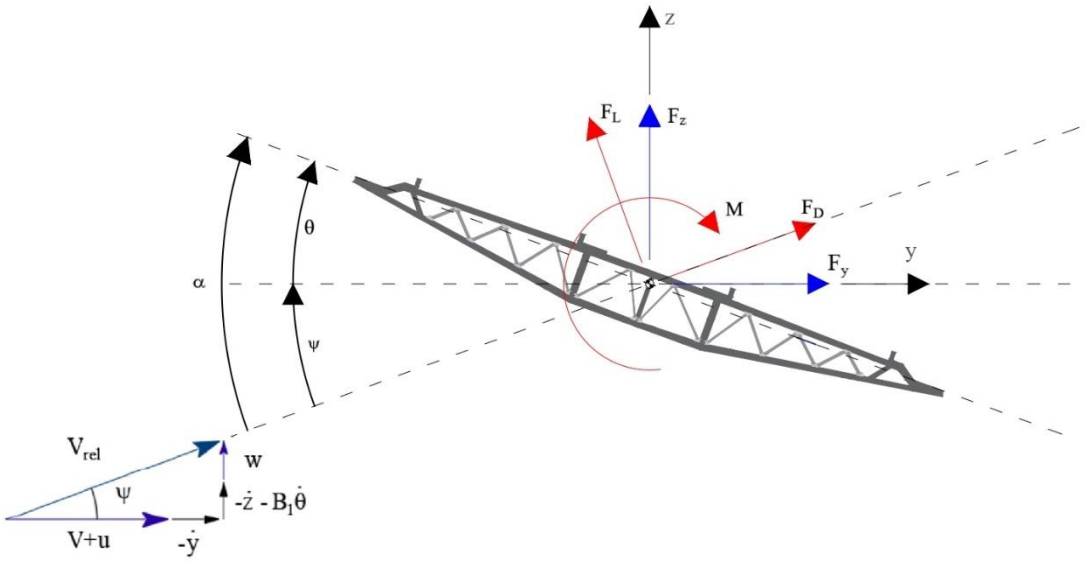

Figure 1.4. Aerodynamic forces on a generic deck section and its sign conventions.

1.2.1 Quasi-steady Theory

The quasi-steady theory (QST) is the most suitable approach to better understand the physics of the aeroelastic problem (M. F. G. Diana 1995), (F. C. G. Diana 1991). The QST well reproduces the aerodynamic forces on a deck for high values of the reduced velocity V^*>15. High reduced velocity means that the time needed by a particle to cross the body is very small compared to the

period of oscillation of the body. Hence, the QST assumes that the aerodynamic forces acting on the bridge deck are not influenced by the frequency of the deck's motion. Consequently, the QST allows to match the aerodynamic forces to the static forces measured on still sectional models via static tests in the wind tunnel (furtherly discussed in Section 2.4.1), and are expressed as:

$$F_D = \frac{1}{2}\rho B L V_{rel}^2 C_D(\alpha) \tag{1-6}$$

$$F_L = \frac{1}{2}\rho B L V_{rel}^2 C_D(\alpha) \tag{1-7}$$

$$M = \frac{1}{2}\rho B^2 L V_{rel}^2 C_M(\alpha) \tag{1-8}$$

Where ρ is the air density, V_{rel} is the relative wind velocity, B is the deck width, L is the length of the generic bridge deck, α is the angle of attack and $C_D(\alpha)$, $C_L(\alpha)$, $C_M(\alpha)$ are respectively the drag, lift and moment aerodynamic coefficients.

In accordance to Figure 1.4, the square of the relative velocity V_{rel}^2 can be expressed as follows:

$$V_{rel}^2 = (V + u - \dot{y})^2 + \left(w - \dot{z} - B_1\dot{\theta}\right)^2 \tag{1-9}$$

And the angle of attack α was previously defined by equation (1-5).

The equations of motion of the deck written in its degrees of freedom y, z and θ are:

$$m_y\ddot{y} + r_y\dot{y} + k_y y = F_y = F_D\cos(\psi) - F_L\sin(\psi) \tag{1-10}$$

$$m_z\ddot{z} + r_z\dot{z} + k_z z = F_z = F_D\sin(\psi) + F_L\cos(\psi) \tag{1-11}$$

$$I_\theta\ddot{\theta} + r_\theta\dot{\theta} + k_\theta\theta = F_\theta = M \tag{1-12}$$

Where $m_{y,z}$ and I_θ are the effective inertias of the deck for the horizontal, vertical and torsional degrees of freedom, $r_{y,z,\theta}$ are the effective viscous damping, and $k_{y,z,\theta}$ the effective stiffness.

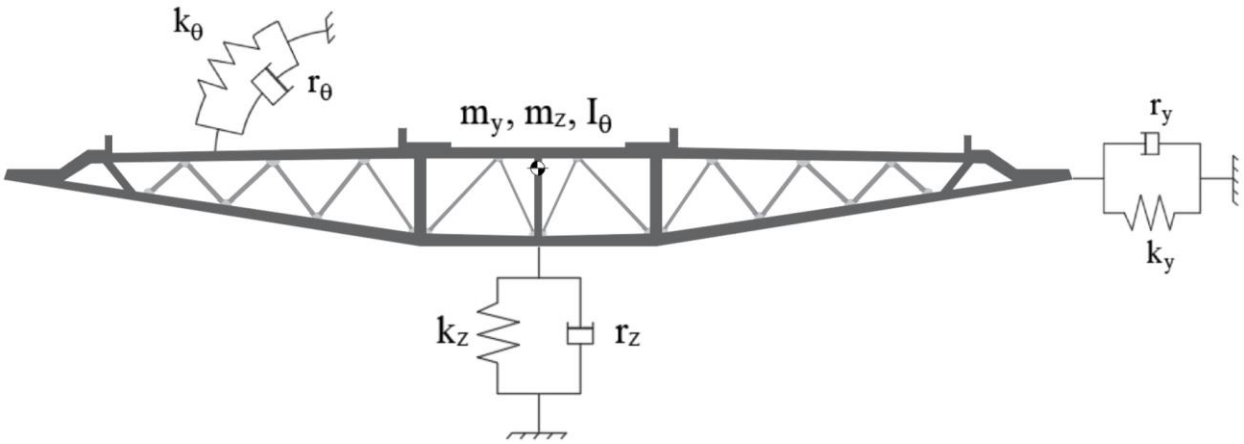

Figure 1.5. Elastically suspended deck section.

Substituting equation (1-9) into equations (1-6)-(1-7)-(1-8), the equations of motion are rewritten as:

$$m_y\ddot{y} + r_y\dot{y} + k_y y = \frac{1}{2}\rho BL\left((V+u-\dot{y})^2 + \left(w-\dot{z}-B_{1y}\dot{\theta}\right)^2\right)\left(C_D(\alpha)\cos(\psi) - C_L(\alpha)\sin(\psi)\right) \quad (1\text{-}13)$$

$$m_z\ddot{z} + r_z\dot{z} + k_z z = \frac{1}{2}\rho BL\left((V+u-\dot{y})^2 + \left(w-\dot{z}-B_{1z}\dot{\theta}\right)^2\right)\left(C_D(\alpha)\sin(\psi) + C_L(\alpha)\cos(\psi)\right) \quad (1\text{-}14)$$

$$I_\theta\ddot{\theta} + r_\theta\dot{\theta} + k_\theta\theta = \frac{1}{2}\rho B^2 L\left((V+u-\dot{y})^2 + \left(w-\dot{z}-B_{1z}\dot{\theta}\right)^2\right)C_M(\alpha) \quad (1\text{-}15)$$

The reference body dimensions $B_{1y,z,\theta}$ contain information of the *flutter derivatives* (Section 1.2.3) and are aimed at 'correcting' the quasi-steady approach by introducing a slight dependence of aerodynamic forces at on the reduced velocity V^*. Hence, the above formulation is referred to as Corrected Quasi-steady Theory (QSTC).

Introducing the displacement vector:

$$\underline{x} = \begin{bmatrix} y \\ z \\ \theta \end{bmatrix}$$

The equation of motion of the system may be written employing a matrix formulation:

$$[M_s]\underline{\ddot{x}} + [R_s]\underline{\dot{x}} + [K_s]\underline{x} = \underline{F_{aero}}(\underline{x}, \underline{\dot{x}}, V_m, \underline{b}) \quad (1\text{-}16)$$

Where $\underline{b} = \begin{bmatrix} u/V \\ w/V \end{bmatrix}$ contains the turbulence components of the wind speed.

This equation represents a non-linear formulation, given both the motion and turbulence dependency of aerodynamic forces, to reproduce the bridge response to the incoming turbulent wind excitation at high reduced velocity values (V^*>15).

1.2.2 Linearized theory

The aeroelastic problem can be simplified by considering the linear formulation of the aerodynamic forces, acting on a generic section of the bridge deck. It is to be recalled that the aerodynamic forces are a non-linear function of the bridge motion, of the mean wind speed and of the turbulent wind velocity components:

$$\underline{F_{aero}} = \underline{F_{aero}}(\underline{x}, \underline{\dot{x}}, V_m, \underline{b})$$

Where:

$$\underline{F_{aero}} = \begin{bmatrix} F_y \\ F_z \\ F_\theta \end{bmatrix}, \qquad \underline{x} = \begin{bmatrix} y \\ z \\ \theta \end{bmatrix}, \qquad \underline{\dot{x}} = \begin{bmatrix} \dot{y} \\ \dot{z} \\ \dot{\theta} \end{bmatrix}, \qquad \underline{b} = \begin{bmatrix} \frac{u}{V} \\ \frac{w}{V} \end{bmatrix}$$

By assuming the hypothesis of small variations of the parameters $\underline{x}, \underline{\dot{x}}$, and $\underline{b}$ a linearization formulation can be performed around the static equilibrium configuration $\underline{x}_0, \underline{\dot{x}}_0$, and $\underline{b}_0$:

$$\underline{x}_0 = \begin{bmatrix} y_0 \\ z_0 \\ \theta_0 \end{bmatrix}, \qquad \underline{\dot{x}}_0 = \begin{bmatrix} 0 \\ 0 \\ 0 \end{bmatrix}, \qquad \underline{b}_0 = \begin{bmatrix} 0 \\ 0 \end{bmatrix}$$

The static equilibrium position $\underline{x}_0$ is computed by solving the corresponding static non-linear problem:

$$[K_s]\underline{x}_0 = \underline{F_{aero}}(\underline{x}_0, \underline{\dot{x}}_0, V_m, \underline{b}_0) \tag{1-17}$$

$$k_y y_0 = \frac{1}{2}\rho B L V_m^2 C_D(\theta_0) \tag{1-18}$$

$$k_z z_0 = \frac{1}{2}\rho B L V_m^2 C_L(\theta_0) \tag{1-19}$$

$$k_\theta \theta_0 = \frac{1}{2}\rho B^2 L V_m^2 C_M(\theta_0) \tag{1-20}$$

Subsequently, the linear expression of the aerodynamic forces acting on the generic section of the bridge deck is:

$$\underline{F_{aero}} = \underline{F_{aero}}(\underline{x}_0, \dot{\underline{x}}_0, \underline{b}_0) + \left.\frac{\partial \underline{F_{aero}}}{\partial \underline{x}}\right|_0 (\underline{x} - \underline{x}_0) + \left.\frac{\partial \underline{F_{aero}}}{\partial \dot{\underline{x}}}\right|_0 \dot{\underline{x}} + \left.\frac{\partial \underline{F_{aero}}}{\partial \underline{b}}\right|_0 \underline{b} \tag{1-21}$$

Considering the QSTC formulation of the aerodynamic forces:

$$F_y = \frac{1}{2}\rho B L V_{rel}^2 (C_D(\alpha)\cos(\psi) - C_L(\alpha)\sin(\psi)) \tag{1-22}$$

$$F_z = \frac{1}{2}\rho B L V_{rel}^2 (C_D(\alpha)\sin(\psi) + C_L(\alpha)\cos(\psi)) \tag{1-23}$$

$$F_\theta = \frac{1}{2}\rho B^2 L V_{rel}^2 C_M(\alpha) \tag{1-24}$$

performing a change of coordinates in which only the dynamic part of the oscillations is considered:

$$\overline{\underline{x}} = \underline{x} - \underline{x}_0 = \begin{bmatrix} \overline{y} = y - y_0 \\ \overline{z} = z - z_0 \\ \overline{\theta} = \theta - \theta_0 \end{bmatrix}$$

linearizing the aerodynamic coefficients:

$$C_D(\alpha) = C_{D_0} + \left.\frac{\partial C_D}{\partial \alpha}\right|_0 \alpha = C_{D_0} + K_{D_0}\alpha \tag{1-25}$$

$$C_L(\alpha) = C_{L_0} + \left.\frac{\partial C_L}{\partial \alpha}\right|_0 \alpha = C_{L_0} + K_{L_0}\alpha \tag{1-26}$$

$$C_M(\alpha) = C_{M_0} + \left.\frac{\partial C_M}{\partial \alpha}\right|_0 \alpha = C_{M_0} + K_{M_0}\alpha \tag{1-27}$$

and linearizing the following terms as well:

$$\psi \approx \frac{w - \dot{\overline{z}} - B_1\dot{\overline{\theta}}}{V} \tag{1-28}$$

$$V_{rel}^2 \approx V^2 + 2Vu - 2V\dot{\overline{y}} \tag{1-29}$$

$$\sin(\psi) \approx \psi \tag{1-30}$$

$$\cos(\psi) \approx 0 \tag{1-31}$$

the linearized expressions of the aerodynamic forces are:

$$F_y = \frac{1}{2}\rho BL(V^2 + 2Vu - 2V\dot{\bar{y}})\left((C_{D_0} + K_{D_0}\alpha) - (C_{L_0} + K_{L_0}\alpha)\psi\right) \tag{1-32}$$

$$F_z = \frac{1}{2}\rho BL(V^2 + 2Vu - 2V\dot{\bar{y}})\left((C_{D_0} + K_{D_0}\alpha)\psi + (C_{L_0} + K_{L_0}\alpha)\right) \tag{1-33}$$

$$F_\theta = \frac{1}{2}\rho B^2 L(V^2 + 2Vu - 2V\dot{\bar{y}})(C_{M_0} + K_{M_0}\alpha) \tag{1-34}$$

Thus, developing the above expressions and neglecting the second order terms:

$$\begin{aligned} F_y = {} & \frac{1}{2}\rho BLV^2 C_{D_0} + \frac{1}{2}\rho BLV^2\left[K_D\left(\overline{\theta} + \frac{w - \dot{\bar{z}} - B_{1y}\dot{\overline{\theta}}}{V}\right) - C_{L_0}\left(\frac{w - \dot{\bar{z}} - B_{1y}\dot{\overline{\theta}}}{V}\right)\right] \\ & + \frac{1}{2}\rho BLV2C_{D_0}\left(u - \dot{\bar{y}}\right) \end{aligned} \tag{1-35}$$

$$\begin{aligned} F_z = {} & \frac{1}{2}\rho BLV^2 C_{L_0} + \frac{1}{2}\rho BLV^2\left[K_L\left(\overline{\theta} + \frac{w - \dot{\bar{z}} - B_{1z}\dot{\overline{\theta}}}{V}\right) - C_{D_0}\left(\frac{w - \dot{\bar{z}} - B_{1z}\dot{\overline{\theta}}}{V}\right)\right] \\ & + \frac{1}{2}\rho BLV2C_{L_0}\left(u - \dot{\bar{y}}\right) \end{aligned} \tag{1-36}$$

$$F_\theta = \frac{1}{2}\rho B^2 LV^2 C_{M_0} + \frac{1}{2}\rho B^2 LV^2\left[K_{M_0}\left(\overline{\theta} + \frac{w - \dot{\bar{z}} - B_{1\theta}\dot{\overline{\theta}}}{V}\right)\right] + \frac{1}{2}\rho B^2 LV2C_{M_0}(u - \dot{\bar{y}}) \tag{1-37}$$

The static and dynamic parts of the aerodynamic forces can be separated and rewritten in a matrix formulation:

$$\underline{F}_{aero,st} = \frac{1}{2}\rho BLV^2\begin{bmatrix} C_{D_0} \\ C_{L_0} \\ BC_{M_0} \end{bmatrix} \tag{1-38}$$

$$\begin{aligned} \underline{F}_{aero,dyn} = {} & \frac{1}{2}\rho BLV^2\begin{bmatrix} 0 & 0 & K_{D_0} \\ 0 & 0 & K_{L_0} \\ 0 & 0 & BK_{M_0} \end{bmatrix}\underline{\overline{x}} \\ & - \frac{1}{2}\rho BLV\begin{bmatrix} 2C_{D_0} & (K_{D_0} - C_{L_0}) & (K_{D_0} - C_{L_0})B_{1y} \\ 2C_{L_0} & (K_{L_0} + C_{D_0}) & (K_{L_0} + C_{D_0})B_{1z} \\ 2BC_{M_0} & BK_{M_0} & BK_{M_0}B_{1\theta} \end{bmatrix}\underline{\dot{\bar{x}}} \\ & + \frac{1}{2}\rho BLV^2\begin{bmatrix} 2C_{D_0} & K_{D_0} - C_{L_0} \\ 2C_{L_0} & K_{L_0} + C_{D_0} \\ 2C_{M_0} & BK_{M_0} \end{bmatrix}\underline{b} \end{aligned} \tag{1-39}$$

The dynamic component $\underline{F}_{aero,dyn}$ of the aerodynamic forces can be written in a compact notation:

$$\underline{F}_{aero,dyn} = \underline{F}_{se} + \underline{F}_{buff} \tag{1-40}$$

Where $\underline{F_{se}}$ are called the self-excited forces originated due to the deck motion and $\underline{F_{buff}}$ are called the buffeting forces related to the incoming wind turbulence:

$$\underline{F_{se}} = -([K_{aero}]\underline{x} + [R_{aero}]\dot{\underline{x}}) \tag{1-41}$$

$$\underline{F_{buff}} = [A_m]\underline{b} \tag{1-42}$$

In which $[R_{aero}]$ and $[K_{aero}]$ are the equivalent damping and stiffness matrices due to the linearized aerodynamic forces:

$$[R_{aero}] = \frac{1}{2}\rho BLV \begin{bmatrix} 2C_{D_0} & (K_{D_0} - C_{L_0}) & (K_{D_0} - C_{L_0})B_{1y} \\ 2C_{L_0} & (K_{L_0} + C_{D_0}) & (K_{L_0} + C_{D_0})B_{1z} \\ 2BC_{M_0} & BK_{M_0} & BK_{M_0}B_{1\theta} \end{bmatrix} \tag{1-43}$$

$$[K_{aero}] = -\frac{1}{2}\rho BLV^2 \begin{bmatrix} 0 & 0 & K_{D_0} \\ 0 & 0 & K_{L_0} \\ 0 & 0 & BK_{M_0} \end{bmatrix} \tag{1-44}$$

And $[A_m]$ is the aerodynamic admittance matrix that multiplied by $\underline{b}$ gives the buffeting forces:

$$[A_m] = \frac{1}{2}\rho BLV^2 \begin{bmatrix} 2C_{D_0} & K_{D_0} - C_{L_0} \\ 2C_{L_0} & K_{L_0} + C_{D_0} \\ 2C_{M_0} & BK_{M_0} \end{bmatrix} \tag{1-45}$$

Finally, the linear aerodynamic forces are substituted into the equations of motion of the system (equation (1-16)):

$$[M_s]\ddot{\underline{x}} + [R_s + R_{aero}]\dot{\underline{x}} + [K_s + K_{aero}]\underline{x} = [A_m]\underline{b} \tag{1-46}$$

In which the contribution of the static forces $\underline{F_{aero,st}}$ is cancelled out with the static deflection $[K_s]\underline{x}_0$ as computed in equation (1-17), and where $[M_s]$, $[R_s]$, and $[K_s]$ are the structural diagonal matrices of the generic section:

$$[M_S] = \begin{bmatrix} m_y & 0 & 0 \\ 0 & m_z & 0 \\ 0 & 0 & I_\theta \end{bmatrix}, \qquad [R_S] = \begin{bmatrix} r_y & 0 & 0 \\ 0 & r_z & 0 \\ 0 & 0 & r_\theta \end{bmatrix}, \qquad [K_S] = \begin{bmatrix} k_y & 0 & 0 \\ 0 & k_z & 0 \\ 0 & 0 & k_\theta \end{bmatrix}$$

It should be noted that $[K_{aero}]$ and $[A_m]$ matrices provided by the linearized QSTC do not depend on the reduced velocity but depend on the mean wind speed instead. Hence, the dependence of $[K_{aero}]$ on the mean wind speed implies that the natural frequencies of the bridge will change with respect to those computed from $[K_S]$ and $[M_S]$ in absence of incoming wind. Likewise, the

dependence of $[R_{aero}]$ on the mean wind speed means that the overall damping is modified. Extra-diagonal terms in $[R_{aero}]$ and $[K_{aero}]$ represent coupling terms. The coupling introduced between the different degrees of freedom depend on the values of the aerodynamic coefficients of the deck section and on the mean wind speed. At certain mean wind speed values, the $[R_{aero}]$ and $[K_{aero}]$ matrices can be modified in such a way that 1 d.o.f. or 2 d.o.f. instability may take place.

1.2.3 Flutter derivatives and aerodynamic admittance functions

The hypothesis in which the quasi-steady theory is based, i.e. that the aeroelastic forces acting on the bridge deck are not influenced by the frequency of the deck motion, is its major limitation. It implies that the QST is valid only for high reduced velocities V^*, or commonly low frequency fluctuations. As a result, the formulation exposed does not depend on the reduced velocity V^*. This is evident in the fact that the aerodynamic coefficients $C_{D,L,M}$ depend on the angle of attack α only. To extend the formulation to the low values of reduced velocities, or, equivalently, high frequency oscillations, V^* dependent parameters called *flutter derivatives* and *aerodynamic admittance functions* are introduced in the formulation of the self-excited and buffeting forces, respectively. These are transfer functions measured over sectional models in the wind tunnel for different angles of attack (F. R. G. Diana 2004). The identification of the flutter derivatives and the aerodynamic admittance functions for the BB3 sectional model with a train is exposed in section 2.4.

Flutter Derivatives

Different conventions from different authors for the flutter derivatives are used. The *"PoliMi notation"* (Zasso 1996) is employed in this thesis and expresses the self-excited forces as follows:

$$F_y^{se} = \frac{1}{2}\rho B L V^2 \left(-p_1^* \frac{\dot{z}}{V} - p_2^* \frac{B\dot{\theta}}{V} + p_3^* \theta + p_4^* \frac{\pi}{2V_\omega^{*2}} \frac{z}{B} - p_5^* \frac{\dot{y}}{V} + p_6^* \frac{\pi}{2V_\omega^{*2}} \frac{y}{B} \right) \tag{1-47}$$

$$F_z^{se} = \frac{1}{2}\rho B L V^2 \left(-h_1^* \frac{\dot{z}}{V} - h_2^* \frac{B\dot{\theta}}{V} + h_3^* \theta + h_4^* \frac{\pi}{2V_\omega^{*2}} \frac{z}{B} - h_5^* \frac{\dot{y}}{V} + h_6^* \frac{\pi}{2V_\omega^{*2}} \frac{y}{B} \right) \tag{1-48}$$

$$F_\theta^{se} = \frac{1}{2}\rho B^2 L V^2 \left(-a_1^* \frac{\dot{z}}{V} - a_2^* \frac{B\dot{\theta}}{V} + a_3^* \theta + a_4^* \frac{\pi}{2V_\omega^{*2}} \frac{z}{B} - a_5^* \frac{\dot{y}}{V} + a_6^* \frac{\pi}{2V_\omega^{*2}} \frac{y}{B}\right) \tag{1-49}$$

where:

- $V_\omega^* = \frac{V^*}{2\pi}$
- p_i^* are the flutter derivatives for the drag force (i=1,…,6).
- h_i^* are the flutter derivatives for the lift force (i=1,…,6).
- a_i^* are the flutter derivatives for the pitching moment (i=1,…,6).

Flutter derivatives have the same meaning of the equivalent aerodynamic stiffness and damping matrices presented in the linearized QST in section 1.2.2. Recalling equation (1-41), the $[K_a]$ and $[R_a]$ can be written with the flutter derivatives as follows:

$$[K_a] = -\frac{1}{2}\rho B L V^2 \begin{bmatrix} p_6^* \frac{\pi}{2V_\omega^{*2}} \frac{1}{B} & p_4^* \frac{\pi}{2V_\omega^{*2}} \frac{1}{B} & p_3^* \\ h_6^* \frac{\pi}{2V_\omega^{*2}} \frac{1}{B} & h_4^* \frac{\pi}{2V_\omega^{*2}} \frac{1}{B} & h_3^* \\ a_6^* \frac{\pi}{2V_\omega^{*2}} & a_4^* \frac{\pi}{2V_\omega^{*2}} & a_3^* \end{bmatrix} \tag{1-50}$$

$$[R_a] = \frac{1}{2}\rho B L V \begin{bmatrix} p_5^* & p_1^* & p_2^* B \\ h_5^* & h_1^* & h_2^* B \\ a_5^* B & a_1^* B & a_2^* B^2 \end{bmatrix} \tag{1-51}$$

The $[K_a]$ and $[R_a]$ matrix coefficients expressed with the flutter derivatives can be compared to those written with the QSTC. At high values of V^*, the experimental stiffness and damping matrices should converge to those obtained through the QSTC. Thanks to this relationship, it is possible to obtain an expression for the length parameters $B_{1y,z,\theta}$ of the QSTC, by dividing the third column of the QSTC aeroelastic damping matrix over the third column of the experimental aeroelastic damping matrix. More precisely:

$$B_{1y} = \frac{p_2^*}{p_1^*} B, \qquad B_{1z} = \frac{h_2^*}{h_1^*} B, \qquad B_{1\theta} = \frac{a_2^*}{a_1^*} B \tag{1-52}$$

At high values of V^*, the following relationships should hold:

- Flutter derivatives p_{1-6}^*:

$$p_1^* = K_{D_0} - C_{L_0}, \qquad p_2^* = \left(K_{D_0} - C_{L_0}\right)\frac{B_{1y}}{B}, \qquad p_3^* = K_{D_0}, \qquad p_4^* = 0,$$
$$p_5^* = 2C_{D_0}, \qquad p_6^* = 0, \tag{1-53}$$

– Flutter derivatives h_{1-6}^*:

$$h_1^* = K_{L_0} - C_{D_0}, \qquad h_2^* = \left(K_{L_0} - C_{D_0}\right)\frac{B_{1z}}{B}, \qquad h_3^* = K_{L_0}, \qquad h_4^* = 0,$$
$$h_5^* = 2C_{L_0}, \qquad h_6^* = 0, \tag{1-54}$$

– Flutter derivatives a_{1-6}^*:

$$a_1^* = K_{M_0}, \qquad a_2^* = K_{M_0}\frac{B_{1\theta}}{B}, \qquad a_3^* = K_{M_0}, \qquad a_4^* = 0, \qquad a_5^* = 2C_{M_0},$$
$$a_6^* = 0, \tag{1-55}$$

Aerodynamic Admittance Functions

Experimental expressions functions can also be identified in the wind tunnel for the formulation of buffeting forces. The turbulence wind components vector $\underline{b}$ is multiplied by these experimental functions, called aerodynamic admittance functions, to obtain the buffeting forces on the generic deck section. Hence, buffeting forces are expressed as:

$$\underline{F}_{buff} = \begin{bmatrix} F_y^{buff} \\ F_z^{buff} \\ F_\theta^{buff} \end{bmatrix} = \frac{1}{2}\rho B L V^2 \begin{bmatrix} \chi_{yu}^* & \chi_{yw}^* \\ \chi_{zu}^* & \chi_{zw}^* \\ B\chi_{\theta u}^* & B\chi_{\theta w}^* \end{bmatrix} \begin{bmatrix} \frac{u}{V} \\ \frac{w}{V} \end{bmatrix} \tag{1-56}$$

Where $\chi^*(V^*)$ are the complex admittance functions and are represented by amplitude and phase, thus: $\chi^* = |\chi|e^{i\phi}$. As an example, the buffeting forces considering only the vertical wind turbulence component w are expressed as:

$$F_y^{buff} = \frac{1}{2}\rho B L V^2 \left(Re\left(\chi_{yw}^*\right)\frac{w}{V} + iIm\left(\chi_{yw}^*\right)\frac{w}{V}\right) \tag{1-57}$$

$$F_z^{buff} = \frac{1}{2}\rho B L V^2 \left(Re\left(\chi_{zw}^*\right)\frac{w}{V} + iIm\left(\chi_{zw}^*\right)\frac{w}{V}\right) \tag{1-58}$$

$$F_\theta^{buff} = \frac{1}{2}\rho B^2 L V^2 \left(Re\left(\chi_{\theta w}^*\right)\frac{w}{V} + iIm\left(\chi_{\theta w}^*\right)\frac{w}{V}\right) \tag{1-59}$$

Aerodynamic admittance functions have the same meaning as the aerodynamic admittance matrix $[A_m]$ presented in section1.2.2.

1.3 Band superposition approach

A short overview on the main aspects of the *Band Superposition* (BS) approach developed at Polimi (D. R. G. Diana 2013) is presented here in order to understand the starting point of the new non-linear method presented in this thesis. It will be seen that non-linear aerodynamic forces can be seen as a low frequency contribution modeled by a non-linear QST and as a high frequency contribution modelled by several rheological models.

The Band Superposition approach was developed following the consideration that even if the bridge deck aerodynamics is dependent on the amplitude of the fluctuations of the angle of attack α and on the reduced velocity V^*, it is possible to separate the low frequency (LF) response of the bridge to turbulent wind from the high frequency (HF) response.

The separation of the LF response from the HF response is reasonable since these two regions show different characteristics. The features of the LF response are as follows:

- The aerodynamic forces show a small dependence on the reduced velocity V^* at high $V*$ values (equivalent to LF), while they depend in greater measure on the angle of attack. As an example to support this statement, Figure 1.6 reports the trend of the unsteady aerodynamic moment coefficients (flutter derivatives for torsional motion) as a function of the reduced velocity, for different angles of attack.
- Large variations of the instantaneous angle of attack are mainly related to the fluctuation of the wind velocity components w and u, since small oscillations of the bridge are expected for stable aerodynamic solutions. These variations are caused by the large turbulent scales present in the atmospheric turbulent wind. The large turbulent structures that are able to generate fluctuations of the angle of attack that could be effective on the bridge deck are, in fact, those having large length scale (usually several times larger than the deck chord) and long time scale (low frequency).

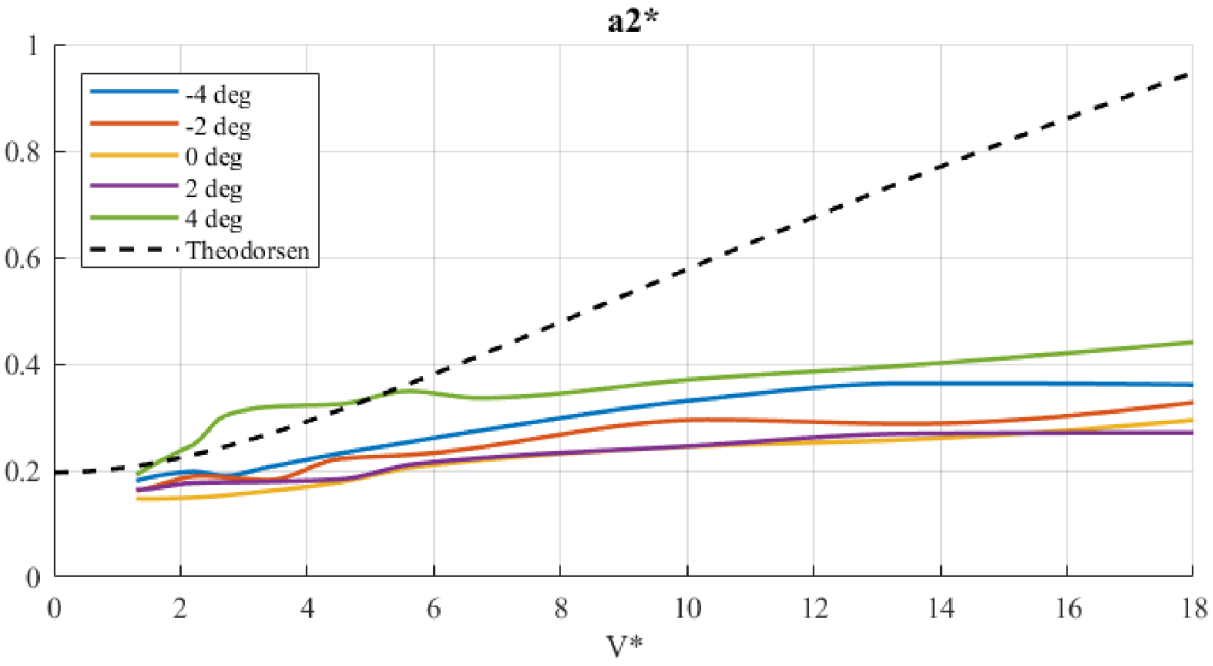

(a)

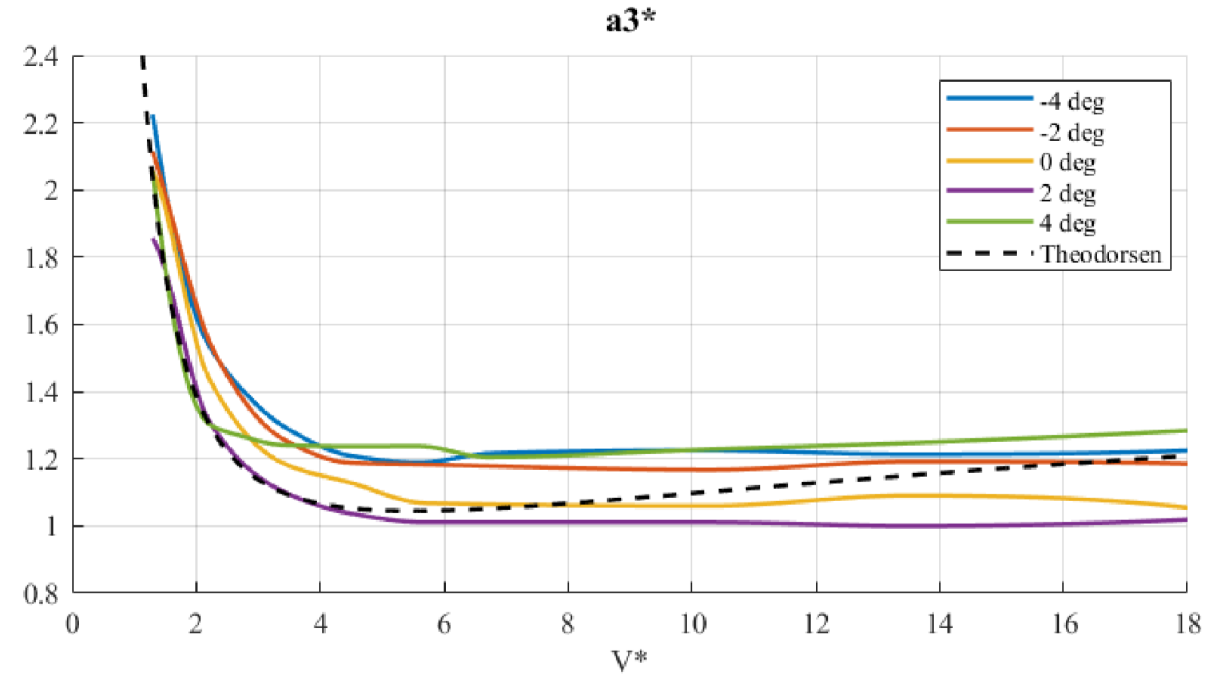

(b)

Figure 1.6. Flutter derivatives a_2^* (a) and a_3^* (b) of the BB3 section without a train and of a flat plate (Theodorsen's theory) vs. V^* for 5 angles of attack (A. Pellegri 2017).

The features of the HF response are the following:

- The aerodynamic forces show large dependence both on the reduced velocity (at low V^* values) and on the mean angle of attack.
- The fluctuations of the HF wind velocity components w and u are characterized by small turbulence length scales with respect to the deck chord length. This produces a flow field variation around the deck section that does not contribute to the global angle of attack.

The previous considerations imply that, when large fluctuations of the angle of attack α occur, in the LF range, a linear modelling of the aerodynamic forces is not appropriate in presence of strong non-linear dependence of the forces on this parameter. In this case, a time domain approach, such as the QST, able to consider the force dependence on large fluctuations of the angle of attack α but not on the reduced velocity V^*, is appropriate.

In the BS approach, a *corrected* quasi-steady theory is applied in order to take anyways into account that even at very low frequencies (or equivalently, at very high V^*) the aerodynamic terms are slightly different from what is obtained using the aerodynamic coefficients because of the rate of change of the angle of attack. This is the so-called QSTC approach and was presented earlier in Section 1.2.3. On the other hand, in the HF range, when small fluctuations of the angle of attack are produced by the wind velocity fluctuations, the aerodynamic forces should be subjected only to the reduced velocity dependency, if they were dependent just on the constant mean angle of attack.

The basic hypothesis of the BS approach is that the mean angle of attack, perceived by the deck in the definition of the aerodynamic force components acting in the HF range, is not only the static mean value but is also related to the fluctuation that takes place at LF with high amplitudes (perceived as static region for the HF terms). Hence, the method suggests that the HF aerodynamic forces are related to the instantaneous angle of attack computed considering the LF deck response and wind spectrum and not to the static mean angle of attack. Consequently, the unsteady HF aerodynamic forces can be expressed as follows:

If it is now considered that the fluctuations of the instantaneous angle of attack in the HF range are small, this means that the problem may be modelled using a linearization of the aerodynamic forces evaluated around the LF instantaneous angle of attack α. Under this assumption, it is possible to model the aerodynamic forces in the HF range by means of the aerodynamic transfer functions that are commonly expressed in bridge aerodynamics through the flutter derivatives coefficients (section 1.2.3), measured by means of wind tunnel tests at different reduced velocities and different mean angles of attack. In this case, being the linear problem considered around a slowly varying solution, represented by the low frequency fluctuation of the angle of attack, the response of the bridge deck is modelled applying, at each time step, the aerodynamic transfer function correspondent to the instantaneous value of the LF angle of attack.

In conclusion, if the BS hypothesis holds, the bridge deck response to turbulent wind might be computed by dividing the problem into two parts: a nonlinear problem at LF modelled using a QSTC approach, and a non-linear problem at HF modelled using a modulation of the aerodynamic transfer functions performed on the basis of the LF fluctuation of the angle of attack.

Moreover, the BS approach exploits rheological models (RM) to contemporary reproduce the reduced velocity V^* and the angle of attack α dependence in time domain on the whole HF band without asking for a HF band decomposition. The developed RM, adopted for the HF band response, is a mechanical model that is made by a group of mechanical elements (masses, springs and dashpots) whose response to a deformation, proportional to the fluctuation of the angle of attack, produces a force that represents the aerodynamic load acting on the deck. The identification of the parameters of the single mechanical element in this case is based on the information contained in the flutter derivatives and aerodynamic admittance function coefficients measured at different mean angles of attack and different reduced velocity.

The basic algorithm of the BS approach proposed by PoliMi (D. R. G. Diana 2013) is reported in Figure 1.7 in which three main steps are highlighted:

1 LF – HF range threshold definition: Identification of a threshold for separating the wind bands, solution of the LF deck response by means of a non-linear corrected QST and solution of the HF deck response by introducing the rheological models. The threshold separating the LF range from the HF range must be defined in terms of reduced velocity V^* or reduced frequency f^*. The threshold delimits the region, at high reduced velocity, where the flutter derivatives coefficients and the aerodynamic admittance function coefficients show a small dependence on the reduced velocity. Once the V^* threshold is defined, it can be used to separate the wind spectrum into two bands.

2 LF response computation: The LF response computation is performed by a QSTC approach. LF Aerodynamic forces depend uniquely on the instantaneous LF angle of attack, on the LF wind velocity turbulent components, and on the LF response of the bridge deck.

$$\underline{F}_{LF}(t) = \underline{F}_{se}\left(\alpha_{LF}(t), \underline{x}_{LF}, \dot{\underline{x}}_{LF}\right) + \underline{F}_{buff}(\alpha_{LF}(t), w_{LF}, u_{LF}) \tag{1-60}$$

3 HF response computation: Unsteady HF aerodynamic forces are modelled in the time domain with a rheological model whose parameters depend on the LF instantaneous angle of attack. Self-excited and buffeting forces are modelled independently, and their effects are summed up exploiting the superposition hypothesis. It is highlighted that HF unsteady forces depend explicitly on the LF angle of attack, on the HF deck motion and on HF incoming turbulence.

$$\underline{F}_{HF}(t) = \underline{F}_{se}\left(\alpha_{LF}(t), \underline{x}_{HF}, \dot{\underline{x}}_{HF}\right) + \underline{F}_{buff}(\alpha_{LF}(t), w_{HF}, u_{HF}) \tag{1-61}$$

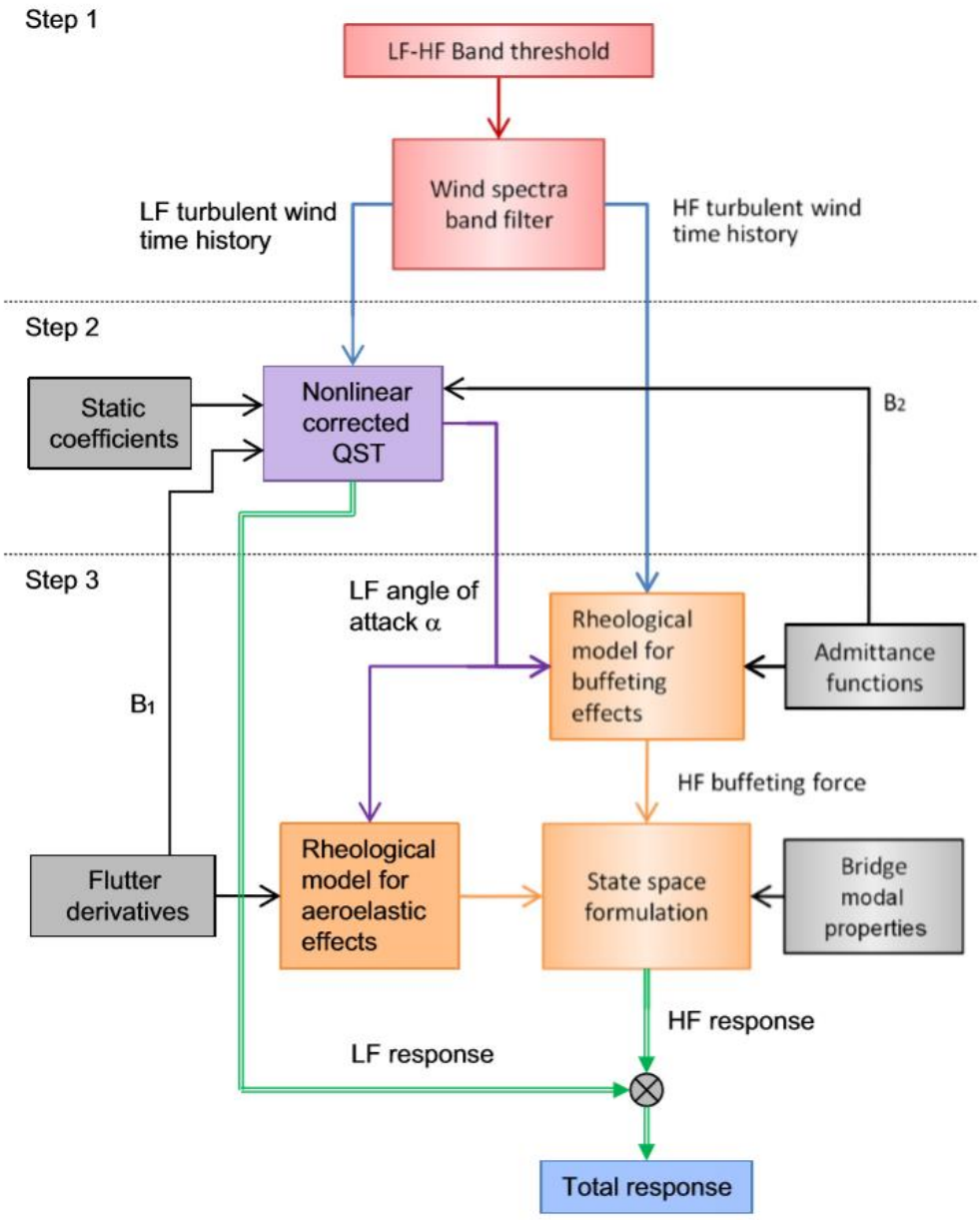

Figure 1.7. Band superposition approach: Simulation flow chart.

Chapter 2

Wind Tunnel Testing

2.1 Introduction

A wind tunnel is a powerful tool used to measure wind loads over structures. It is ideally desired to perform measurements on the full-scale structure. However, within the benchmark procedure established by the workgroup of IABSE Task Group 3.1, the step 2 (for which this research is part of) requires a modification on the natural frequencies of the bridge and a controlled periodical wind velocity profile for buffeting analysis, 2 tasks that are feasible only on a wind tunnel.

Tests at the wind tunnel laboratory at Politecnico di Milano (GVPM) are performed in order to define the parameters which allow us to compute the response of the deck section ($[K_a], [R_a],$ and $[A_m]$) with the numerical procedure, as well as to measure its response to a controlled wind flow scenario. The present chapter displays in section 2.2 an insight of the characteristics of the GVPM; in section 2.3 the experimental setup for the BB3 deck section is described; and finally, section 2.4 describes the parameters of the deck section obtained on the wind tunnel tests and the direct measurements of the response.

2.2 Wind Tunnel Laboratory (GVPM)

GVPM is a closed-circuit type wind tunnel composed of two test rooms arranged in a vertical layout (Figure 2.1). The lower chamber of the loop is intended for low turbulence tests. The upper chamber, where the BB3 deck sectional model was tested, is called the Boundary Layer Test Section and is able to reproduce the atmospheric boundary layer.

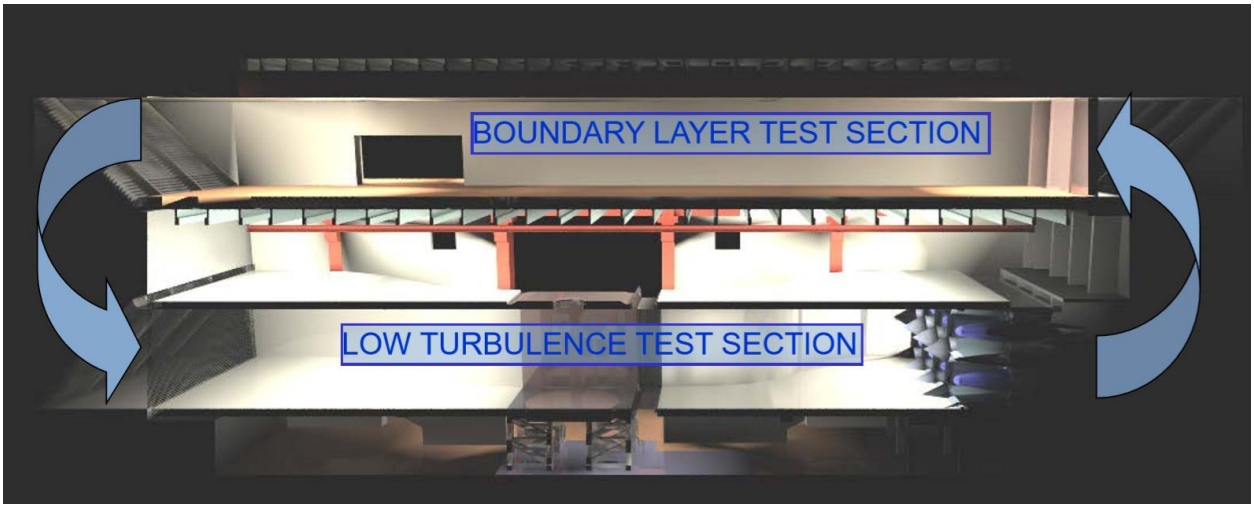

Figure 2.1. Overview of the flow circuit (http://www.wintunnel.polimi.it/facility n.d.).

The wind flow is generated by an array of 14 1.8 m diameter, 100 kW fans with a total power of 1.4 MW. They are arranged into two rows of seven 2x2 m independent cells. The fans are driven independently allowing for a continuous control of its rotation speed in order to obtain the desired wind speed in the test section.

The Boundary Layer Test Section is aimed at testing civil structure scaled models. The atmospheric boundary layer of different terrain conditions can be used by employing different configurations of spires and surface roughness elements. The latter, however, was not used during the sectional tests on the deck section of the BB3. Among the technical specifications we can find the following (http://www.wintunnel.polimi.it/facility n.d.):

- Dimensions: 13.84 m wide x 3.84 m high x 35 m long
- Maximum wind speed: 16 m/s
- Mean velocity variations in the test section: 5%
- Turbulence intensity: 2% for smooth flow conditions, Up to 35% for atmospheric boundary layer simulations
- Turntable: 13 m diameter.

The model is set over the turntable which is a floating floor that allows for a clean model set-up avoiding the interference of the instrumentation cable connections out of the flow. The room also enables for the setup of upstream active or passive turbulence generators to simulate and control a desired wind speed scenario.

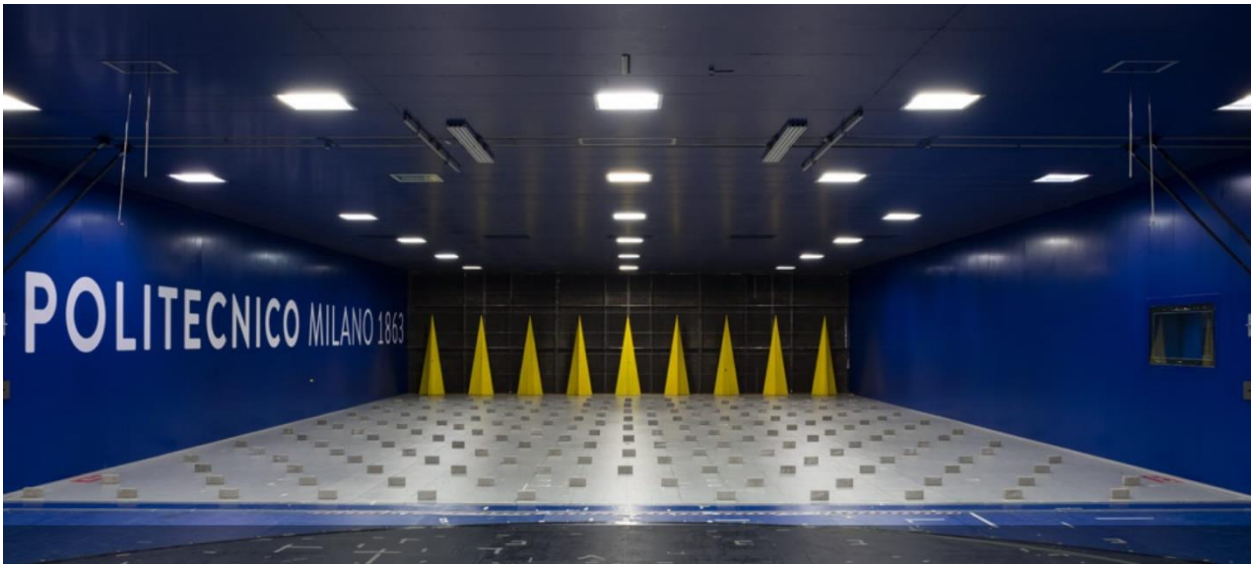

Figure 2.2. Spires and roughness elements for the simulation of the atmospheric boundary layer (http://www.wintunnel.polimi.it/facility n.d.).

2.3 Experimental Setup

The sectional model was arranged in two different fundamental configurations for the different tests, they were:

- The model supported on oil dynamic actuators
- The model suspended by means of steel cables

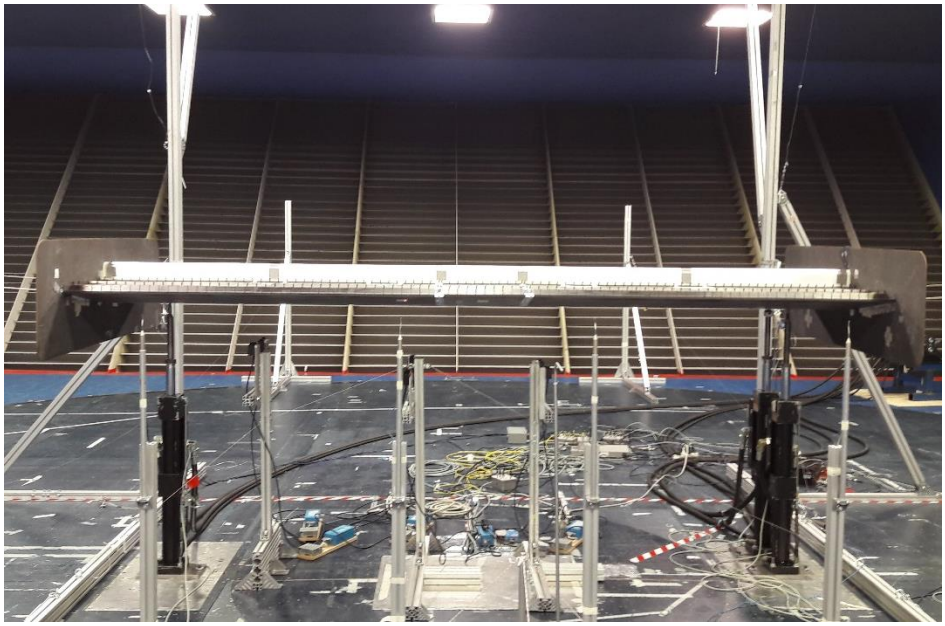

Figure 2.3. The sectional model supported on oil dynamic actuators in the Boundary Layer Test Section.

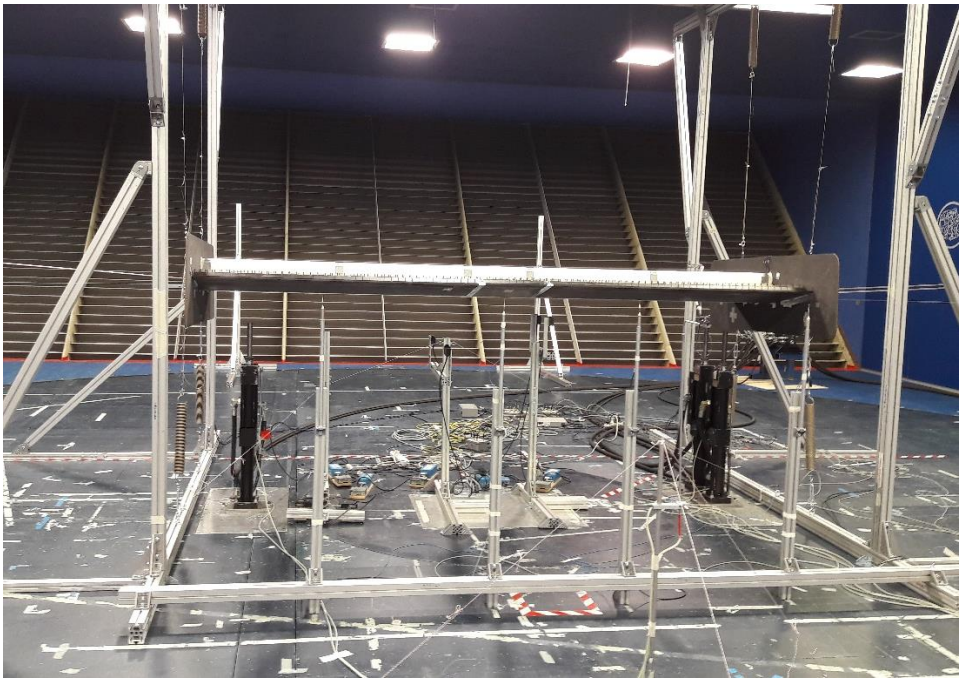

Figure 2.4. The sectional model suspended by means of steel cables on the Boundary Layer Test Section.

2.3.1 Instrumentation for Wind Flow Measurements

– Pitot Tube:

Is the most common device used to determine the flow velocity inside the test section (see Figure 2.5). The orifice A is the stagnation point and measures the total head i.e. $p + \frac{1}{2}\rho V^2$, while orifice B reads the static pressure p only. The dynamic pressure $q = A - B = \frac{1}{2}\rho V^2$ can be directly measured by if the two ports A and B are connected to a differential manometer. The velocity can then be computed as $V = \sqrt{\frac{2q}{\rho}}$. It is used to obtain the mean wind speed inside the tunnel and give no information about wind speed direction.

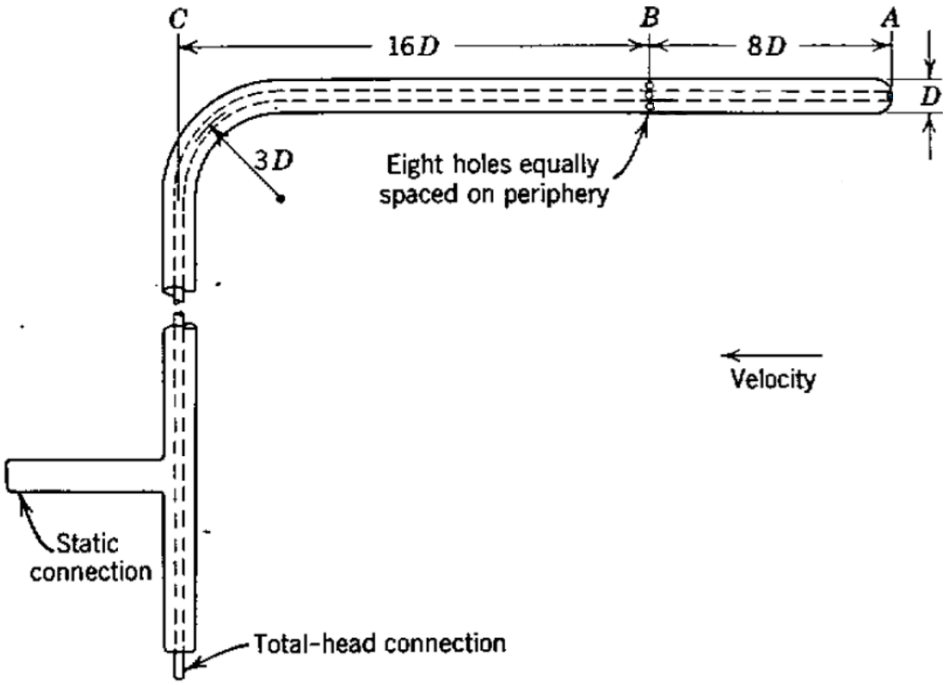

Figure 2.5. Pitot-static tube.

A single pitot tube was installed upstream of the sectional model as it appears in Figure 2.6.

Figure 2.6. Installed Pitot tube.

– Cobra Probe

The wind velocity direction is measured by means of the cobra probe. It is a multi-hole pressure probe that provides dynamic 3-component velocity and local static pressure measurements and can measure flow fields within a range of ± 45°.

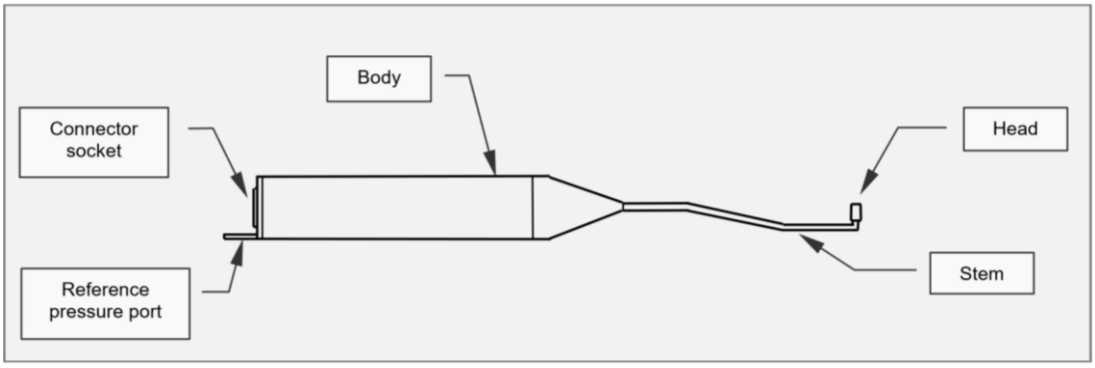

Figure 2.7. Schematic diagram of a Cobra Probe.

In the experimental setup, 4 cobra probes with a sampling frequency of 1500 Hz were placed one chord (1.17 m) upwind to the leading edge of the sectional model and at a 1.43 m height from the floor (see Figure 2.8).

Figure 2.8. Installed cobra probes, displayed inside the 4 green circles.

2.3.2 Instrumentation for Model Motion Measurements

Three sets of two laser transducers measuring vertical displacements were placed below different sections of the model in correspondence of the pressure rings (discussed in 2.3.4) as follows (see Figure 2.9):

- Laser transducers below pressure ring #2 with $d = 190$ mm
- Laser transducers below pressure ring #3 with $d = 745$ mm
- Laser transducers below pressure ring #4 with $d = 200$ mm

Figure 2.9. Lasers transducers below the deck sectional model.

Where d is the distance between the upwind and the downwind laser transducer. The vertical (z_j) and torsional (θ_j) displacements of the jth section for the forced motion tests are computed based on the laser transducer records as follows:

$$z_j = \frac{z_{j,upwind} + z_{j,downwind}}{2} \tag{2-1}$$

$$\theta_j = \tan^{-1}\left(\frac{z_{j,upwind} - z_{j,downwind}}{d_j}\right) \tag{2-2}$$

In which $z_{j,\,upwind}$ and $z_{j,\,downwind}$ are the vertical oscillations recorded by the upwind and downwind laser transducers of the jth laser set, respectively, and d_j is the distance between the two lasers.

However, the lasers' measurements output are recorded in Volts (V) and a calibration is required in order to obtain the vertical oscillations in millimeters (mm). For this scope, calibration tests are performed in which the angle θ is known *a priori*, and then the straight-line formula is used to match the angle recorded by the lasers:

$$\theta_{known} = m \cdot \theta_{recorded} + b \tag{2-3}$$

In the above equation, $\theta_{recorded}$ is computed similar to equation (2-2) with the difference that instead of using z_i, the direct measurements of the lasers in Volts (V) are used. As a result, the dimensions of $\theta_{recorded}$ are [V/mm], the dimensions of m are [mm/V], and those of b are [rad] in order to match the dimensions of θ_{known} in [rad]. As an example, a calibration of the laser transducers below pressure ring #3 is displayed in Figure 2.10. In this case, it was set θ_{known}=0°, 3°, 6° and 10°.

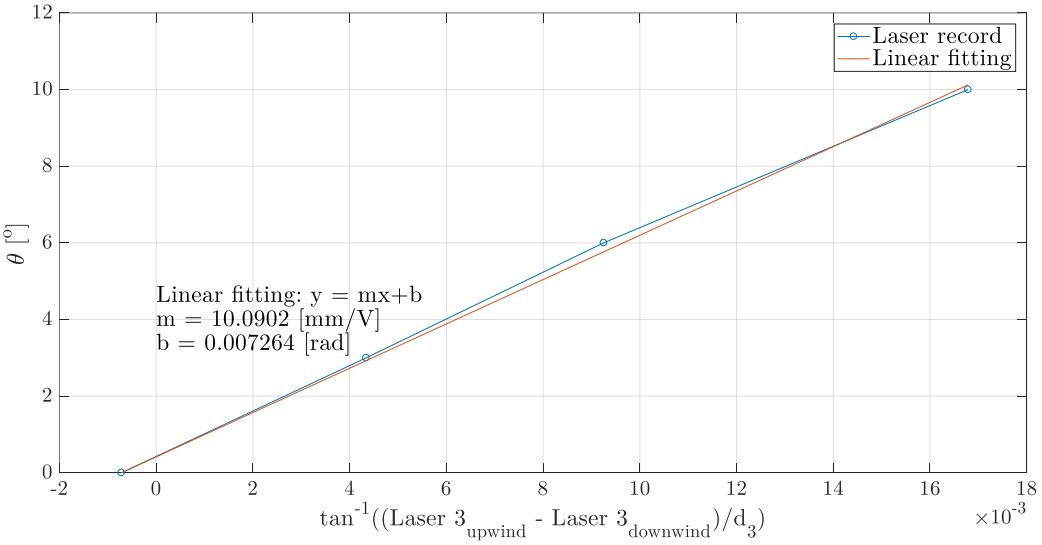

Figure 2.10. Calibration of the laser transducers below pressure ring #3.

2.3.3 Forcing System

Forced motion tests and harmonic wind input excitation tests (explained in detail in section 2.4) were practiced over the sectional model implementing the devices listed below.

- Hydraulic actuators

Three computer-controlled hydraulic actuators drive the forced motion tests, generating a harmonic motion around a user-defined average angle of attack. Figure 2.3 shows that, as seen from the upwind side, the sectional model has 1 actuator (L_1) placed on its left end and 2 actuators (L_2 and L_3) are placed on the right end of the sectional model. This configuration allows to the application of torsional and vertical motions on the sectional model separately in order to measure the flutter derivatives.

– Active turbulence generator

An array of airfoils is used and set to rotate around a fixed axis with a given harmonic motion with up to 3 different frequencies. This device generates a given fluctuation of the incoming flow in the vertical plane with an improved (almost deterministic) knowledge of the low-frequency content of the wind spectrum. The active turbulence generator was implemented on the identification of the Aerodynamic Admittance Matrix $[A_m]$ and on the forced motion tests which will then be compared to the results obtained with the Rheological Model.

(a) (b)

Figure 2.11. Implemented active turbulence generator: (a) array of 10 NACA0012 profile airfoils; (b) low frequency turbulence is generated in the incoming flow.

2.3.4 Instrumentation for force measurements

It is possible to define the aerodynamic forces by the integration of the pressure and shear stresses over the whole body surface (see Figure 2.12). Considering the sign convention reported in Figure 2.13 and summing up the pressure and shear stress contribution projected along the flow direction and perpendicular to the flow, the drag and lift forces can be computed as follows:

$$F_D = \int p \cdot \cos\theta \, dA + \int \tau_w \sin\theta \, dA$$

$$F_L = \int -p \cdot \sin\theta \, dA + \int \tau_w \cos\theta \, dA$$

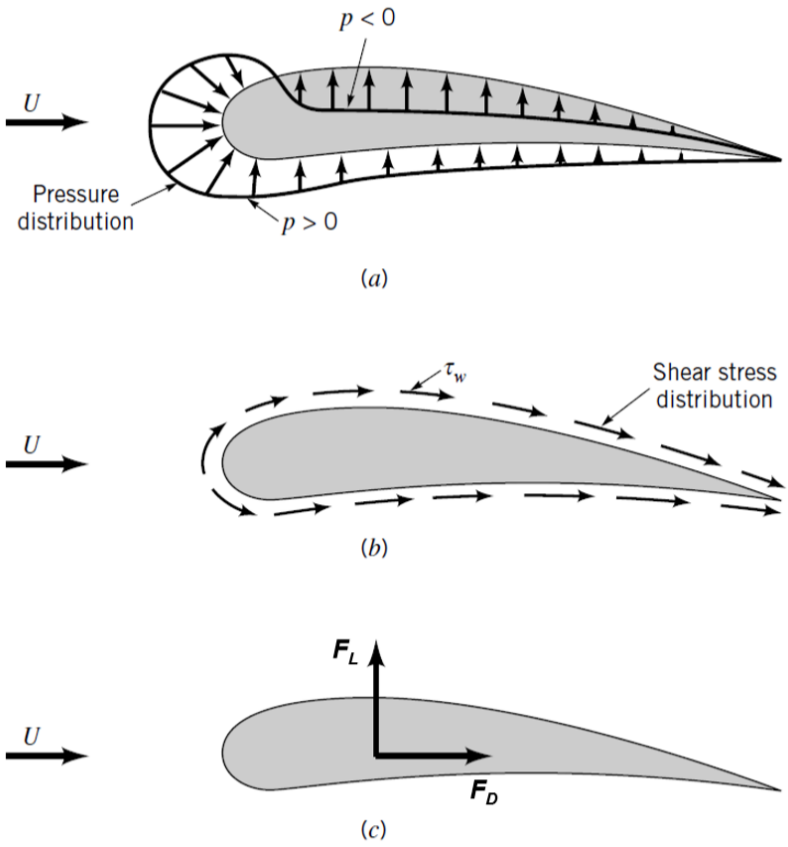

Figure 2.12. (a) Surface pressure distribution ; (b) Shear stress distribution ; (c) Lift Force F_L and drag force F_D over an airfoil profile

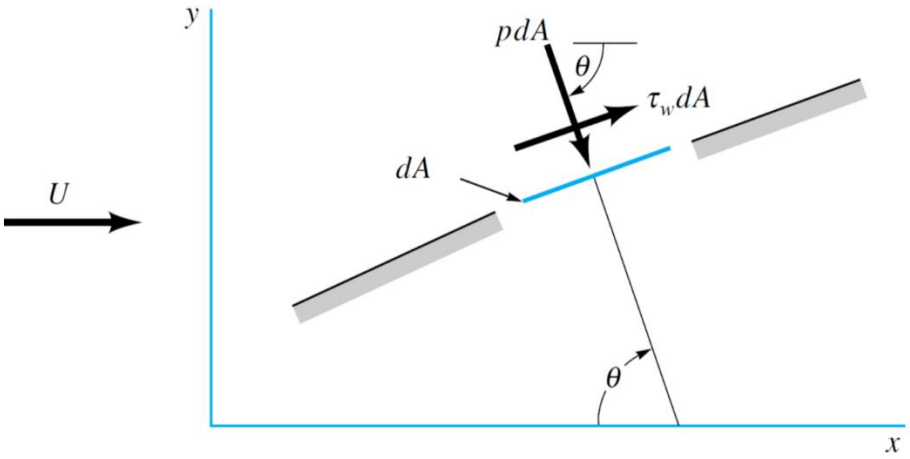

Figure 2.13. Sign convention of pressure and shear stress on a point of a body surface.

Given the presence of the train in the sectional model, shear stresses provide a small contribution to the aerodynamic forces. Instead, the pressure distribution along the body is predominant. Given the above, the aerodynamic forces were measured by considering only the surface pressure by using *pressure taps*.

- Pressure taps

The surface pressure was measured at a sampling frequency of 300 Hz on four rings, each one composed of 62 pressure taps. For each ring, half of the pressure taps were distributed on the upper part of the model and half on the lower part, as displayed in.

Each tap was realized through a hole located on the external surface of the model. Plastic tubes were used to connect each tap to pressure transducers placed inside the model to realize a clean set-up. Eight transducers were placed along the overall model, two for each ring of pressure taps.

The frequency response of the tubing connection may introduce distortions; therefore, the best response can be obtained using a tube as short as possible. The transfer function of the tubing is then used to correct the measured pressures taking into account the amplification due to the pneumatic connection.

2.4 Wind Tunnel Tests

The following wind tunnel tests were conducted, each one of them with a specific purpose:

1. Static tests (2.4.1), which measure the static lift, drag and moment coefficients (C_L, C_D and C_M, respectively) as a function of the angle of attack α.
2. Dynamic tests (2.4.2), which allow for the identification of both the flutter derivatives contained in the aerodynamic stiffness [K_a] and damping [R_a] matrix, and the aerodynamic admittance functions [A_m].
3. Suspended tests (2.4.3), which identify the mechanical parameters of 2 different configurations of the deck suspended by means of steel cables attached to a set of springs.
4. Forced motion tests (2.4.4), with direct measurement of the response of the sectional model suspended elastically, excited with a well-defined mono-, bi-, and tri-harmonic input wind turbulence in order to compare and validate numerical results.

2.4.1 Static tests

Static tests are implemented in order to identify the drag, lift and moment coefficients C_D, C_L and C_M. It is to be recalled that if the oscillations of the bridge deck were to occur with high values of V^*, these coefficients would be enough to compute its response via the definition of the QST aeroelastic and admittance matrices (chapter 1). As a result, static coefficients are relevant in the computation of both the static and dynamic behavior of the bridge deck.

The static tests were conducted in a *quasi-static* manner in order to spend less time. It implies that the sectional model was set to rotate around its longitudinal axis (making use of the hydraulic actuators) at a very low motion frequency (f = 0.01 Hz) from an inclination of -10º to 10º. This way, the rotation velocity is so small that no dynamic effects arise allowing for the implementation of this procedure. As a result, a smooth curve of the static coefficients as a function of α is obtained for the entire range of angles, instead of a discrete set of observation points. Different tests were conducted at different wind speeds in order to identify Reynolds effects.

It was considered that, due to the presence of the train in the sectional model, the aerodynamic forces over the deck will arise due to pressure forces primarily, and the shear forces contribution of the flow over the deck will be negligible. Due to the above, only the pressure tap system was used as a force measurement instrument and the force balance was not used in the wind tunnel tests. The pressure measurements of ring n° 3 were used to compute the static coefficients as this ring is in a central part of the sectional model, remaining to some extent undisturbed of its boundary conditions.

It is noted that pressure taps measure the aerodynamic forces in a local reference system which follows the rotation of the deck. However, the aerodynamic forces are measured with reference to a global reference system based in the wind velocity, and a projection must be done as follows (Figure 2.14):

$$F_y = F_D^* \cos\theta + F_L^* \sin\theta \tag{2-4}$$

$$F_z = -F_D^* \sin\theta + F_L^* \cos\theta \tag{2-5}$$

$$F_\theta = M^* \tag{2-6}$$

The rotation $\theta$is directly obtained from the hydraulic actuators which control the motion of the sectional model.

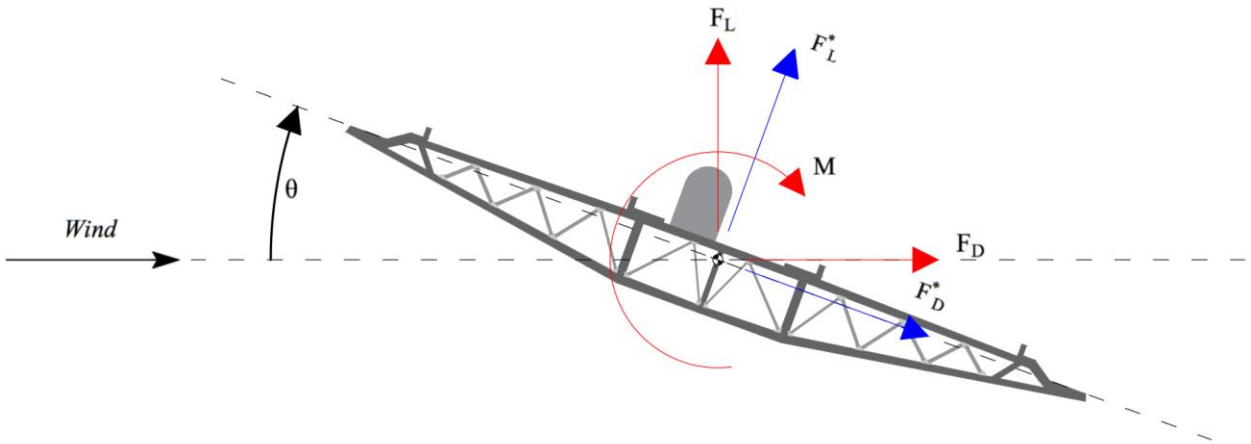

Figure 2.14. Aerodynamic forces, local and global reference systems.

The drag coefficient obtained for the different tests at different mean wind speeds is reported in Figure 2.15. It is observed that at a mean wind speed of 14.63 m/s the drag coefficient is slightly higher than at lower velocities, especially at $+10^{o}$. This occurs because the Reynolds number at this speed is high, and the pressure taps are not able to correctly capture the pressure forces at this speed. Considering this phenomenon, and in order to not include these disturbances, the values of the drag coefficient at V_m=14.63 m/s were left out when computing the average value among the different mean wind speeds.

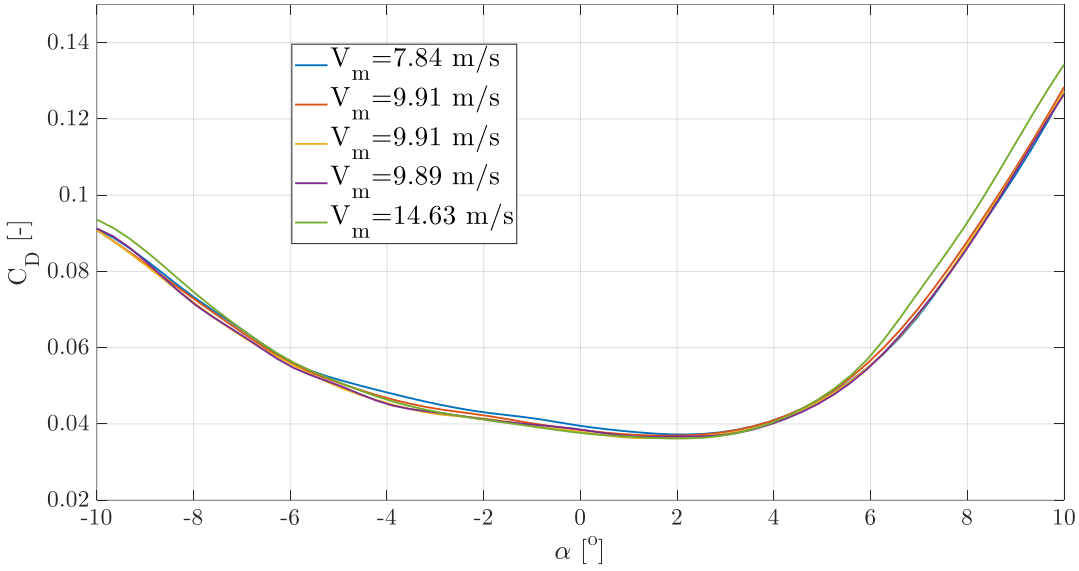

Figure 2.15. Drag coefficient measurements at different mean wind speeds.

The lift and moment coefficients are displayed in Figure 2.16 and Figure 2.17. No relevant discrepancies of the coefficients at different mean wind speeds are observed

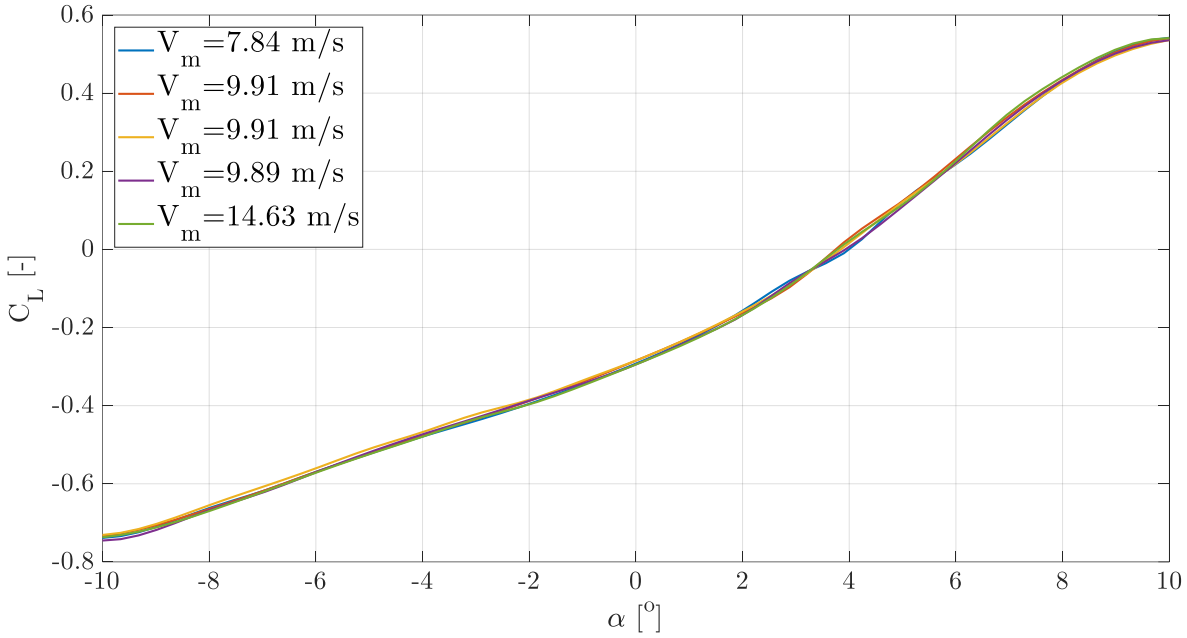

Figure 2.16. Lift coefficient measurements at different mean wind speeds.

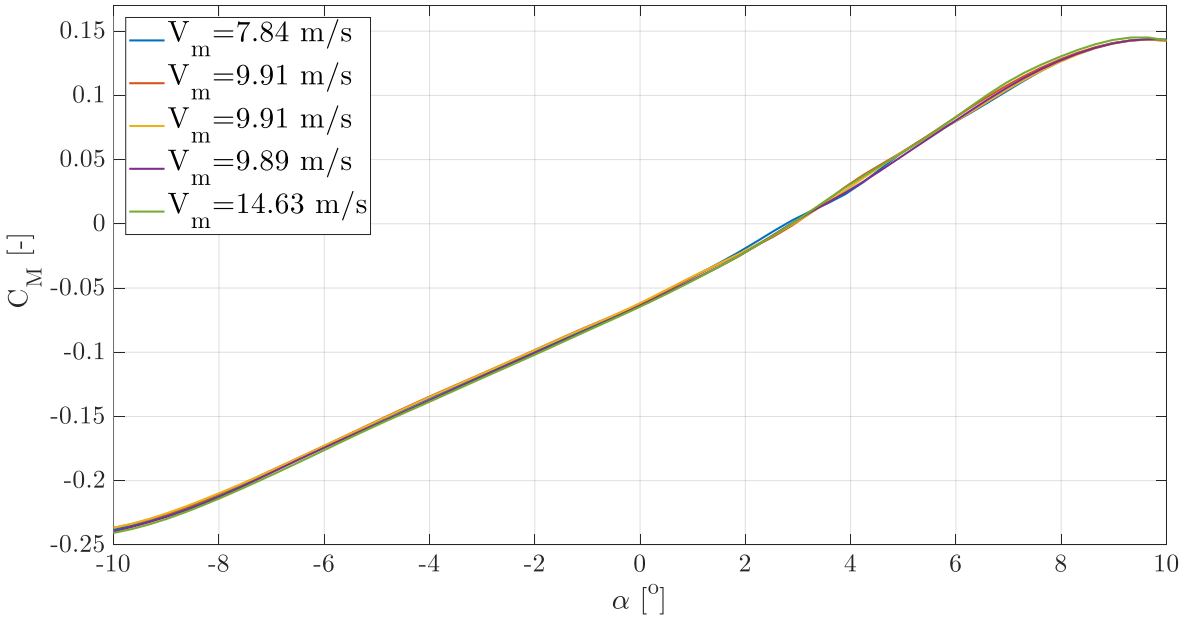

Figure 2.17. Moment coefficient measurements at different mean wind speeds.

The mean value of the static aerodynamic coefficients (with exception of the drag coefficient, whose values at V_m=14.63 m/s were left out) and their derivatives are reported in Figure 2.18 and Figure 2.19.

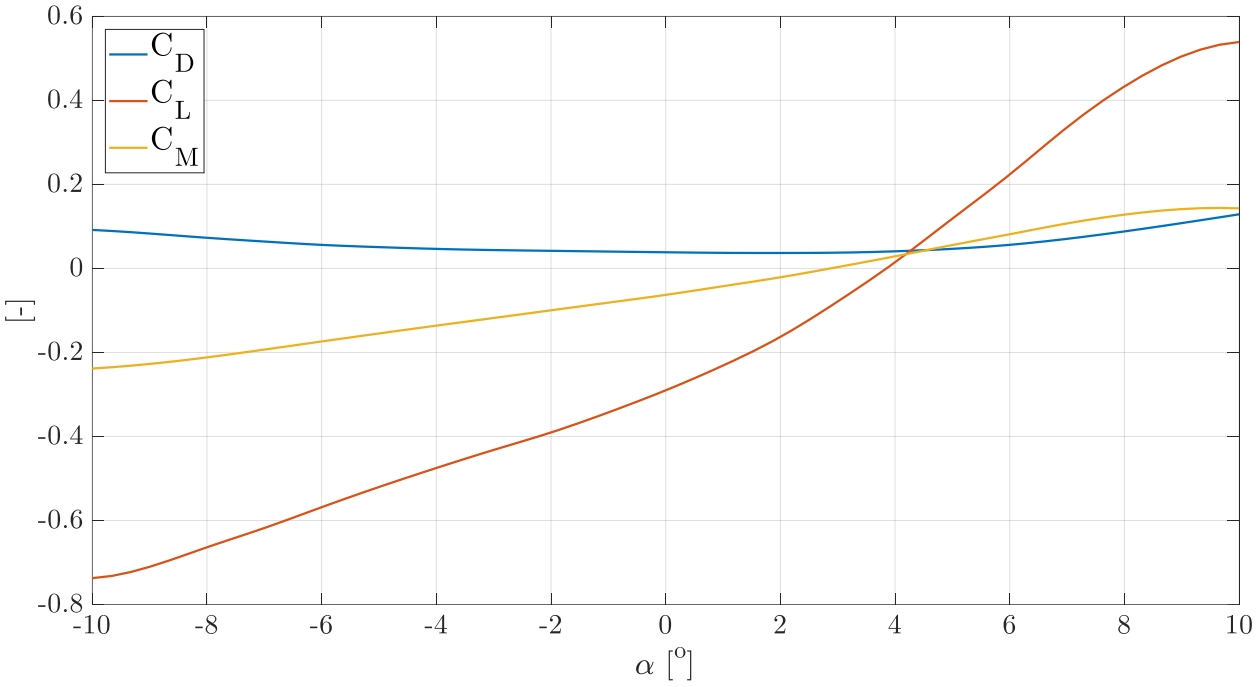

Figure 2.18. C_D, C_L and C_M at the Third Bosphorus Bridge deck sectional model with a train.

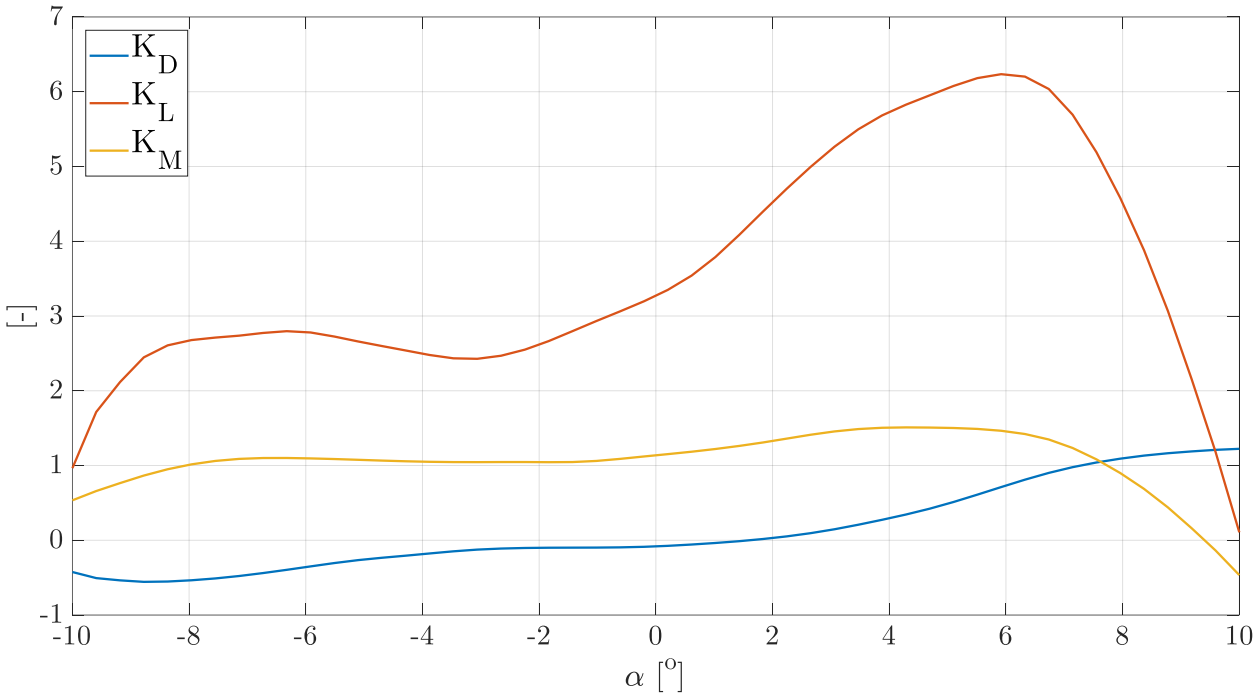

Figure 2.19. K_D, K_L and K_M at the Third Bosphorus Bridge deck sectional model with a train.

2.4.2 Dynamic Tests

The dynamic tests were conducted in order to obtain flutter derivatives on one side, which allow for the assembly of the aeroelastic matrices [K_a] and [R_a], and the aerodynamic admittance functions [A_m], which allow us to write the buffeting forces vector. The fundamental difference with respect to the static tests is that in the dynamic tests the sectional model is set to oscillate at a high frequency such that the QST is no longer able to describe analytically the response of the bridge deck.

Flutter Derivatives

The aeroelastic stiffness and damping matrices allow us to identify the so-called self-excited aerodynamic forces (chapter 1) as a function of the bridge deck motion, represented with its y, z and θ coordinates. These forces are computed as follows (equation (1-41)):

$$\underline{F_{se}} = -([K_a] \cdot \underline{x} + [R_a] \cdot \underline{\dot{x}}) \tag{2-7}$$

However, the experimental setup of the sectional model restrained the model's oscillation in its horizontal degree of freedom. Hence, the flutter derivatives related to the deck's oscillation in its horizontal motion were not identified. It is important to recall whatsoever, that the stability of the deck is governed by its vertical and torsional degrees of freedom. For instance, to ensure 1 d.o.f. dynamic stability it must be satisfied that the diagonal terms of the aeroelastic damping matrix [R_a] are positive, fulfilled if the flutter derivatives h_1^* and a_2^* are both greater than zero for the vertical and torsional degrees of freedom, respectively. At last, neglecting the horizontal forces F_y in the self-excited forces vector $\underline{F_{se}}$ and the oscillations in the horizontal direction y, equation (2-7) is rewritten according to the Polimi formulation (Zasso, 1996) as follows:

$$F_{se,z} = \frac{1}{2}\rho V_m^2 B L\left(-h_1^*\frac{\dot{z}}{V} - h_2^*\frac{B\dot{\theta}}{V} + h_3^*\theta + h_4^*\frac{\pi}{2V_\omega^{*2}}\frac{z}{B}\right) \tag{2-8}$$

$$F_{se,\theta} = \frac{1}{2}\rho V_m^2 B^2 L\left(-a_1^*\frac{\dot{z}}{V} - a_2^*\frac{B\dot{\theta}}{V} + a_3^*\theta + a_4^*\frac{\pi}{2V_\omega^{*2}}\frac{z}{B}\right) \tag{2-9}$$

And the matrices result as follows:

$$[K_a] = -\frac{1}{2}\rho V_m^2 BL \begin{bmatrix} h_4^* \frac{\pi}{2V_\omega^{*2}B} & h_3^* \\ a_4^* \frac{\pi}{2V_\omega^{*2}} & a_3^* B \end{bmatrix} \tag{2-10}$$

$$[R_a] = \frac{1}{2}\rho V_m BL \begin{bmatrix} h_1^* & h_2^* B \\ a_1^* B & a_2^* B^2 \end{bmatrix} \tag{2-11}$$

The tests were conducted in order to encompass the widest range of $V^* = \frac{V}{fB}$ values given that the flutter derivatives are a function of the reduced velocity V^* and on the mean angle of attack θ_0. The wind flow was set with mean speeds ranging from 4 m/s to 15 m/s and the forced motion frequency ranged from 0.5 Hz to 2.5 Hz. In consequence, it was able to describe the flutter derivatives over a range of V^*=1.33 ~ 25. On the other hand, the mean angles of attack studied were all greater or equal than zero. For the flutter derivatives related to the vertical motion, the mean angles of attack around which the deck motion was set to oscillate were: 0°, 3° and 6°. Meanwhile, the flutter derivatives related to the torsional motion were studied on an additional mean angle of attack of 5° in addition to the mean angles of attack of 0°, 3° and 6°. The reason for which the flutter derivatives were not identified under negative values of the mean angle of attack is because the static rotation θ_0 is 3° (Figure 2.18), and the forced motion tests are conducted by making the deck sectional model rotate around θ_0, thus only in positive angles.

In order to identify the flutter derivatives a harmonic motion is imposed in the sectional model employing the hydraulic actuators described in section 2.3.3. . Afterwards, the forces F_y and F_θ are measured using the pressure taps and a transfer function is defined. The real part of the transfer function identifies the stiffness-related flutter derivatives while the imaginary part of the transfer function identifies the damping-related flutter derivatives. The procedure is explained in further detail in the successive paragraph.

$-\ a_1^*, a_4^*, h_1^*, h_4^*$

A vertical harmonic motion is imposed on the deck such that $z(t) = Ze^{i\Omega t}$, and consequently $\dot{z}(t) = i\Omega Ze^{i\Omega t}$. The motion amplitude must be small in order that the problem can be linearized. Two complex transfer functions can be written by substituting the above in equations (2-8) and (2-9):

$$\frac{F_{se,z}}{\frac{1}{2}V_m^2 BL} = C_L = \left(\frac{\pi}{2V_\omega^{*2}}h_4^* - \frac{i\Omega}{V}h_1^*\right)Ze^{i\Omega t} \tag{2-12}$$

$$\frac{F_{se,\theta}}{\frac{1}{2}V_m^2 B^2 L} = C_M = \left(\frac{\pi}{2V_\omega^{*2}}a_4^* - \frac{i\Omega}{V}a_1^*\right)Ze^{i\Omega t} \tag{2-13}$$

In order to obtain the data needed in the above equations, the pressure taps were employed in recording the aerodynamic forces, the pitot tube measured the incoming velocity, and the lasers measured the oscillations (in this case vertical) of the sectional model. Figure 2.20 schematically displays the procedure followed:

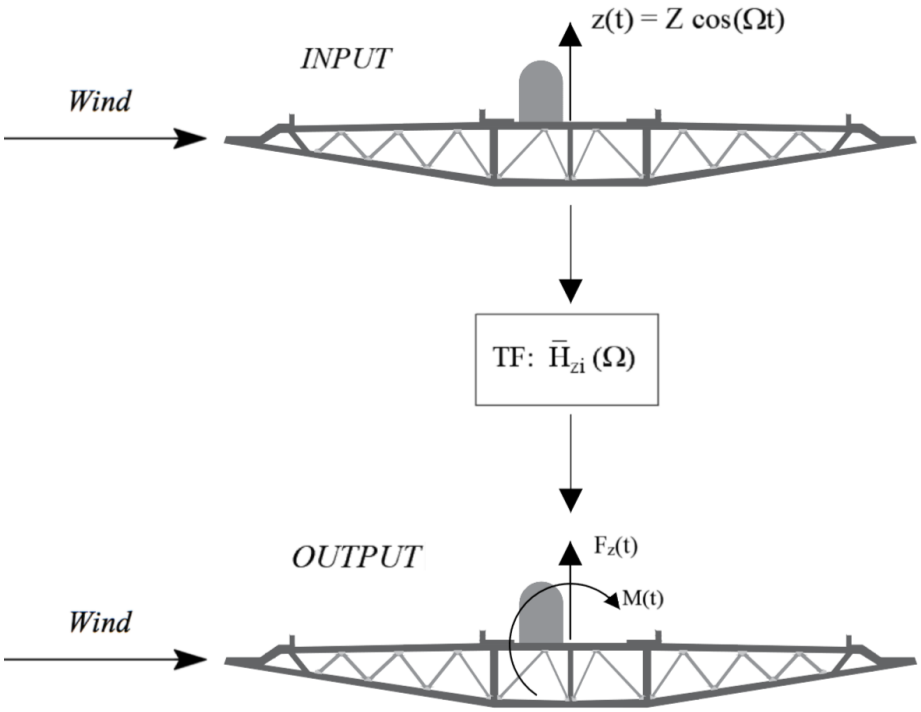

Figure 2.20. Procedure to define the aerodynamic transfer functions for the z d.o.f.

Therefore, the flutter derivatives are given by:

$$h_1^* = -\frac{V}{\Omega} \cdot Im\left\{\frac{C_L}{z}\right\} \tag{2-14}$$

$$h_4^* = \frac{2V_\omega^{*2}B}{\pi} \cdot Re\left\{\frac{C_L}{z}\right\} \tag{2-15}$$

$$a_1^* = -\frac{V}{\Omega} \cdot Im\left\{\frac{C_M}{z}\right\} \tag{2-16}$$

$$a_4^* = \frac{2V_\omega^{*2}B}{\pi} \cdot Re\left\{\frac{C_M}{z}\right\} \tag{2-17}$$

$- a_2^*, a_3^*, h_2^*, h_3^*$

A analogic procedure as the one described above is employed to define the flutter derivatives of the torsional d.o.f. (see Figure 2.21). A vertical harmonic motion is imposed on the deck such that $\theta(t) = \Theta e^{i\Omega t}$, and consequently $\dot{\theta}(t) = i\Omega\Theta e^{i\Omega t}$. The motion amplitude must be small in order that the problem can be linearized. Two complex transfer functions can be written by substituting the above in equations (2-8) and (2-9):

$$\frac{F_{se,z}}{\frac{1}{2}V_m^2 BL} = C_L = \left(h_3^* - \frac{i\Omega \mathrm{B}}{V} h_2^*\right)\Theta e^{i\Omega t} \tag{2-18}$$

$$\frac{F_{se,\theta}}{\frac{1}{2}V_m^2 B^2 L} = C_M = \left(a_3^* - \frac{i\Omega \mathrm{B}}{V} a_2^*\right)\Theta e^{i\Omega t} \tag{2-19}$$

In order to obtain the data needed in the above equations, the pressure taps were employed in recording the aerodynamic forces, the pitot tube measured the incoming velocity, and the lasers measured the oscillations (in this case torsional) of the sectional model.

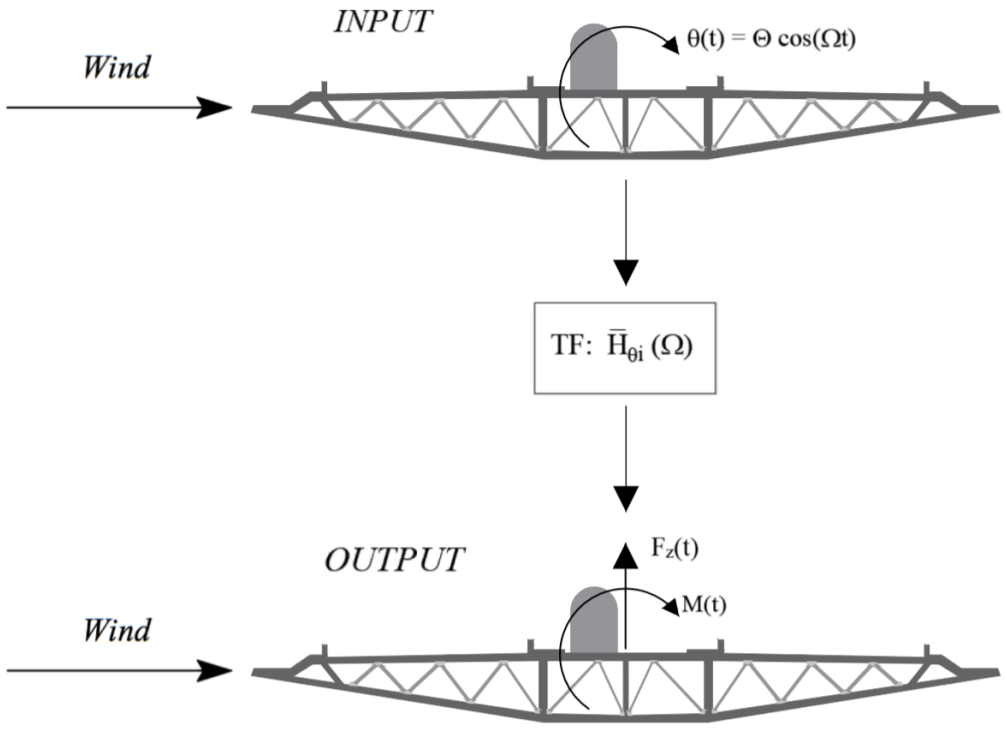

Figure 2.21. Procedure to define the aerodynamic transfer functions for the θ d.o.f.

Consequently, the flutter derivatives are given by:

$$h_2^* = -\frac{V}{\mathrm{B}\Omega} \cdot Im\left\{\frac{C_L}{\theta}\right\} \tag{2-20}$$

$$h_3^* = Re\left\{\frac{C_L}{\theta}\right\} \tag{2-21}$$

$$a_2^* = -\frac{V}{\mathrm{B}\Omega} \cdot Im\left\{\frac{C_M}{\theta}\right\} \tag{2-22}$$

$$a_3^* = Re\left\{\frac{C_M}{\theta}\right\} \tag{2-23}$$

The flutter derivatives at different mean angles of attack needed for the computation of the deck sectional model along the z and θ degrees of freedom are reported on Figure 2.22 through Figure 2.29.

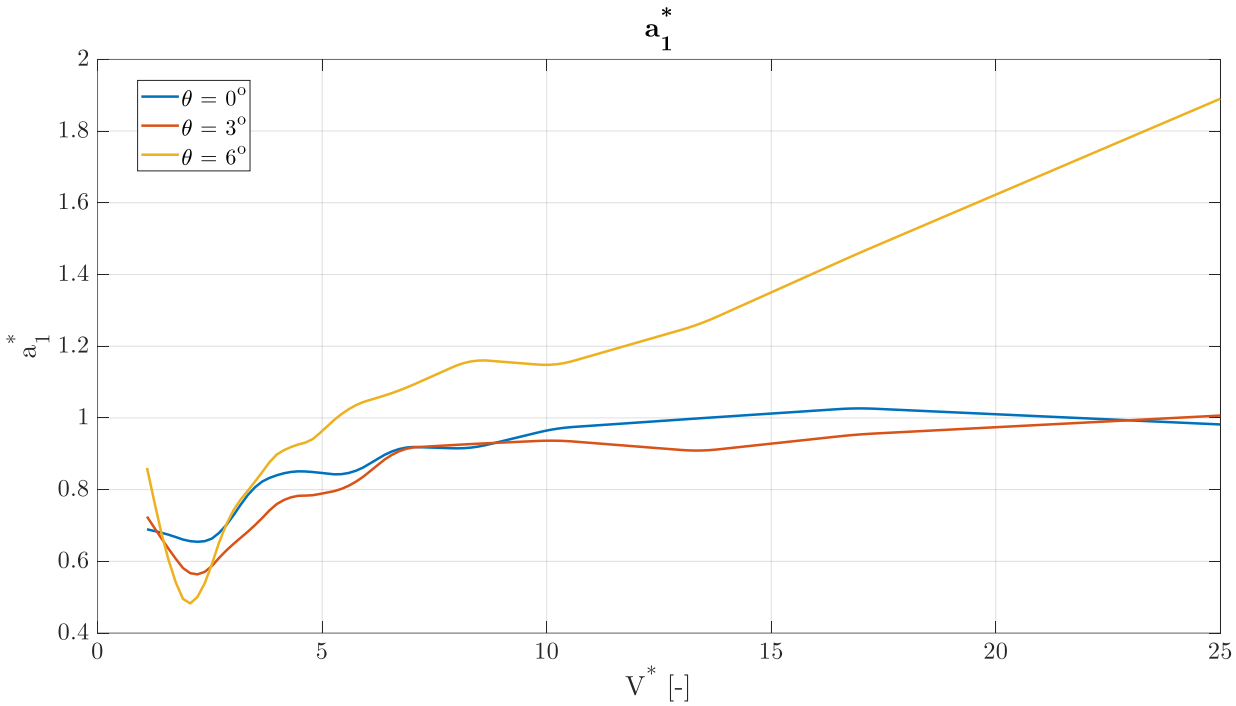

Figure 2.22. Polimi moment flutter derivative a_1^*.

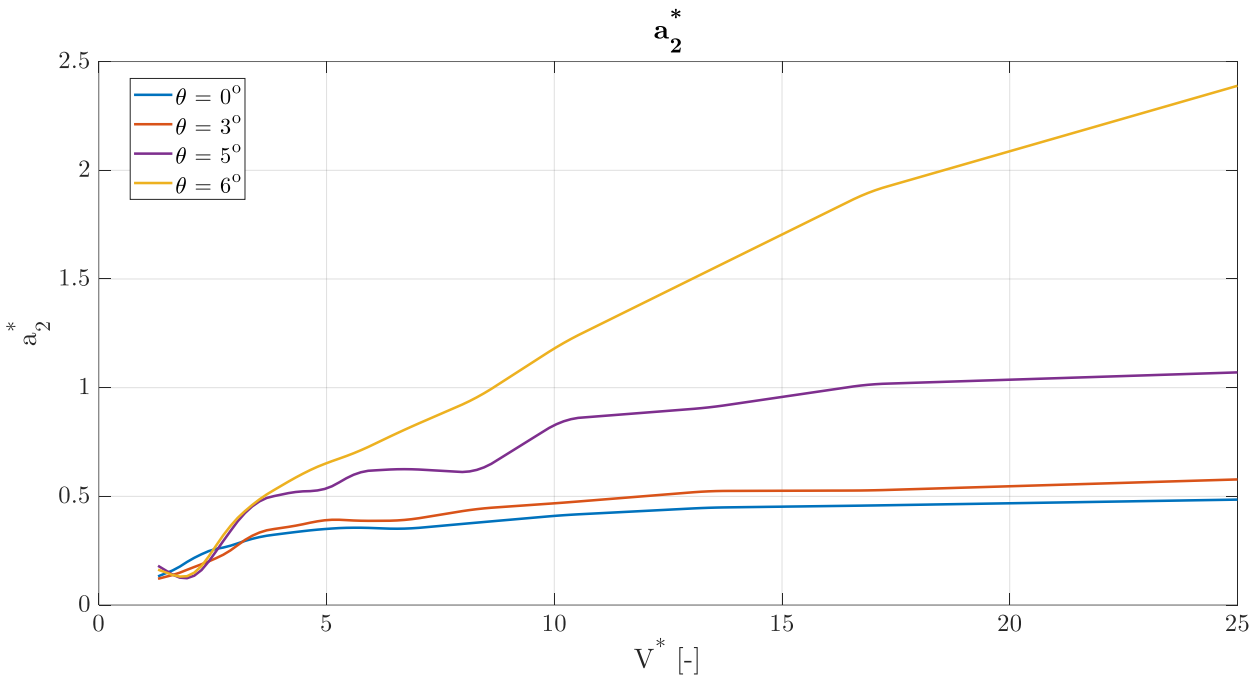

Figure 2.23. Polimi moment flutter derivative a_2^*.

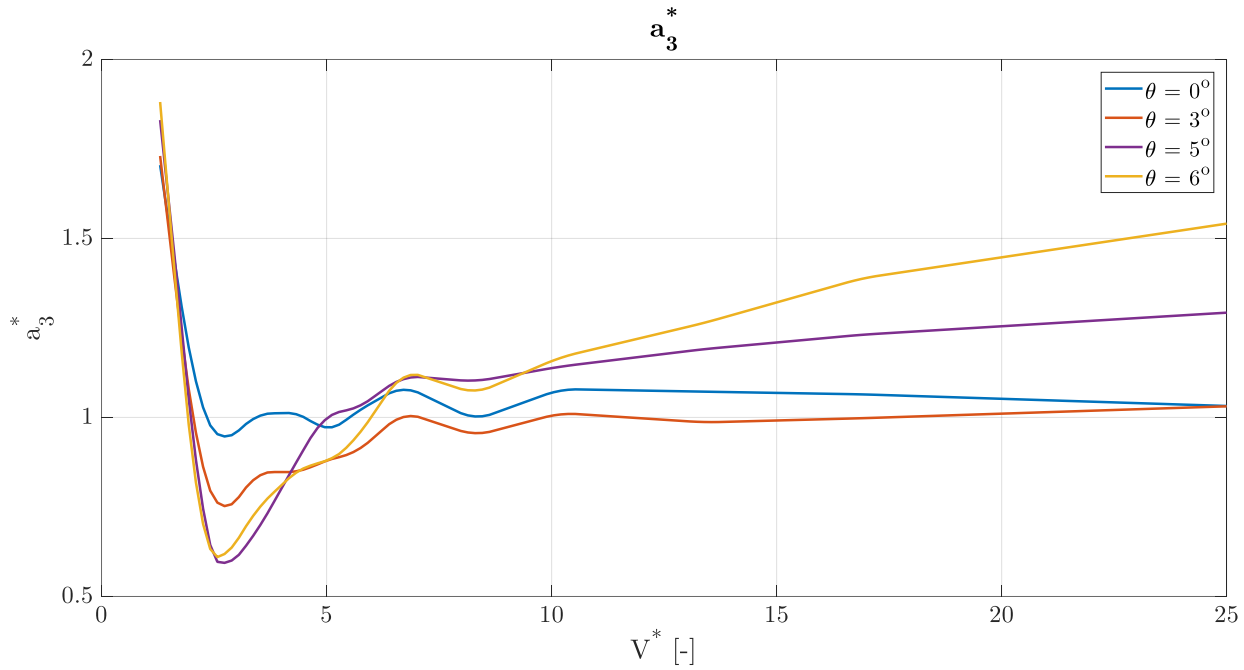

Figure 2.24. Polimi moment flutter derivative a_3^*.

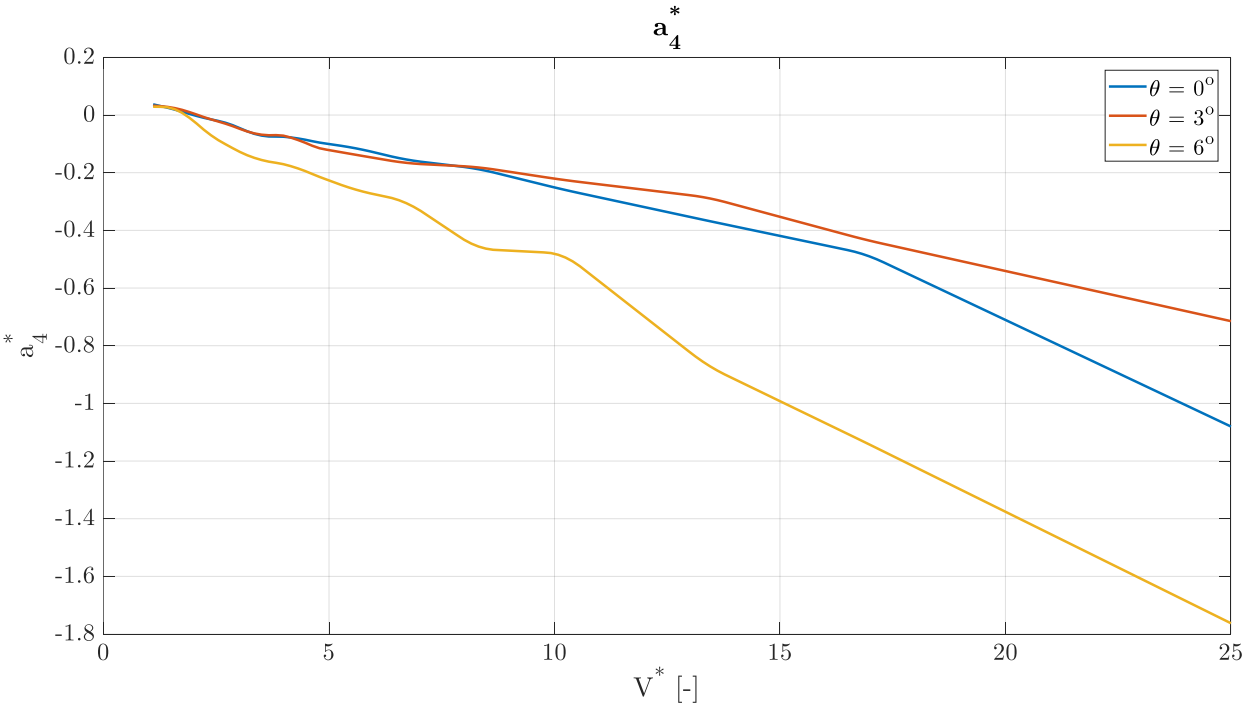

Figure 2.25. Polimi moment flutter derivative a_4^*.

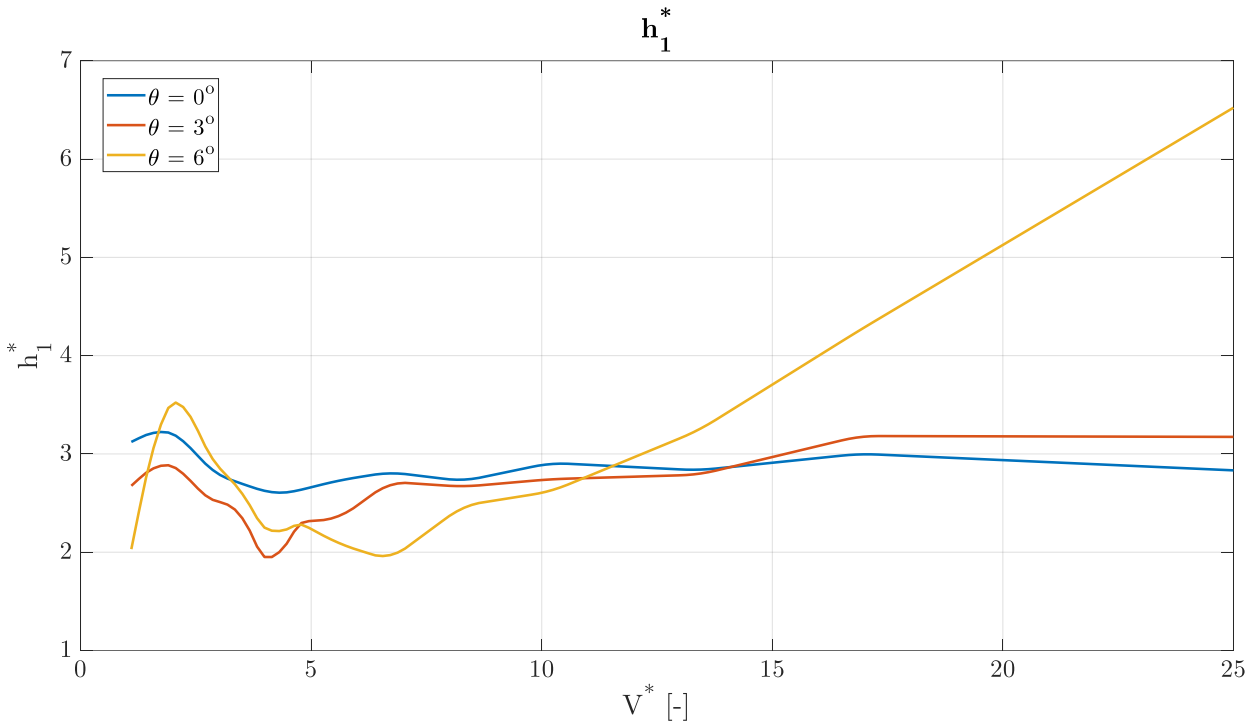

Figure 2.26. Polimi lift flutter derivative h_1^*.

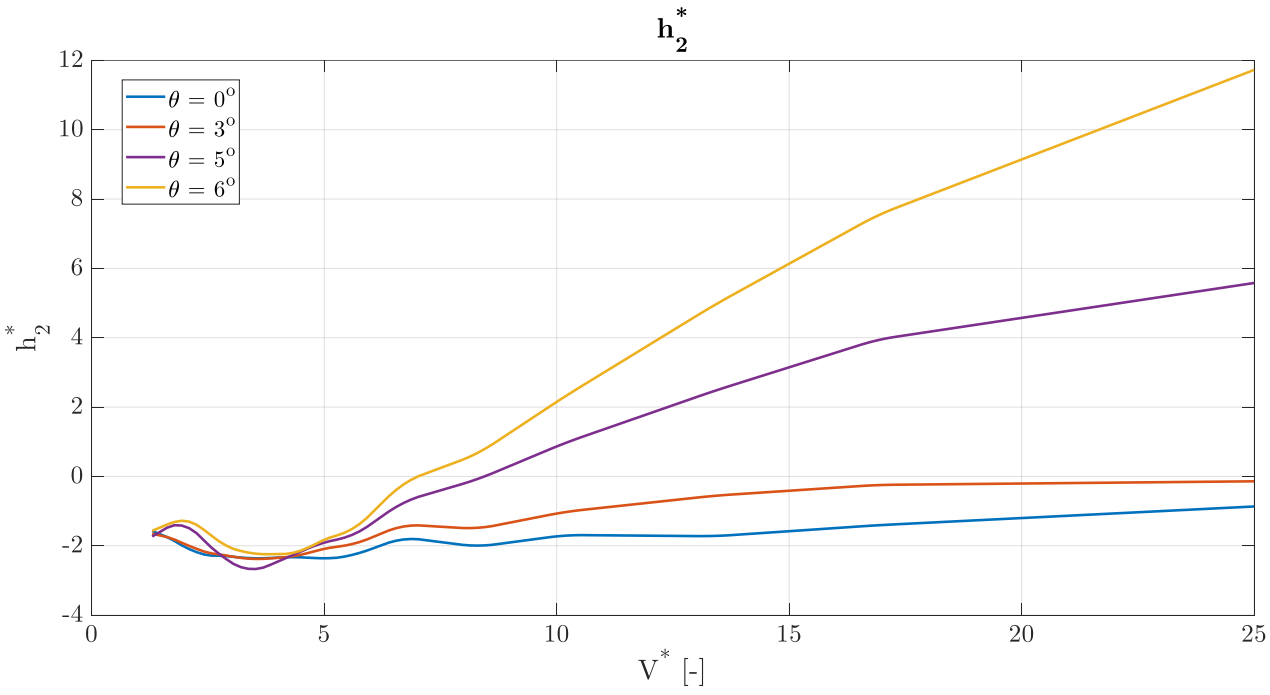

Figure 2.27. Polimi lift flutter derivative h_2^*.

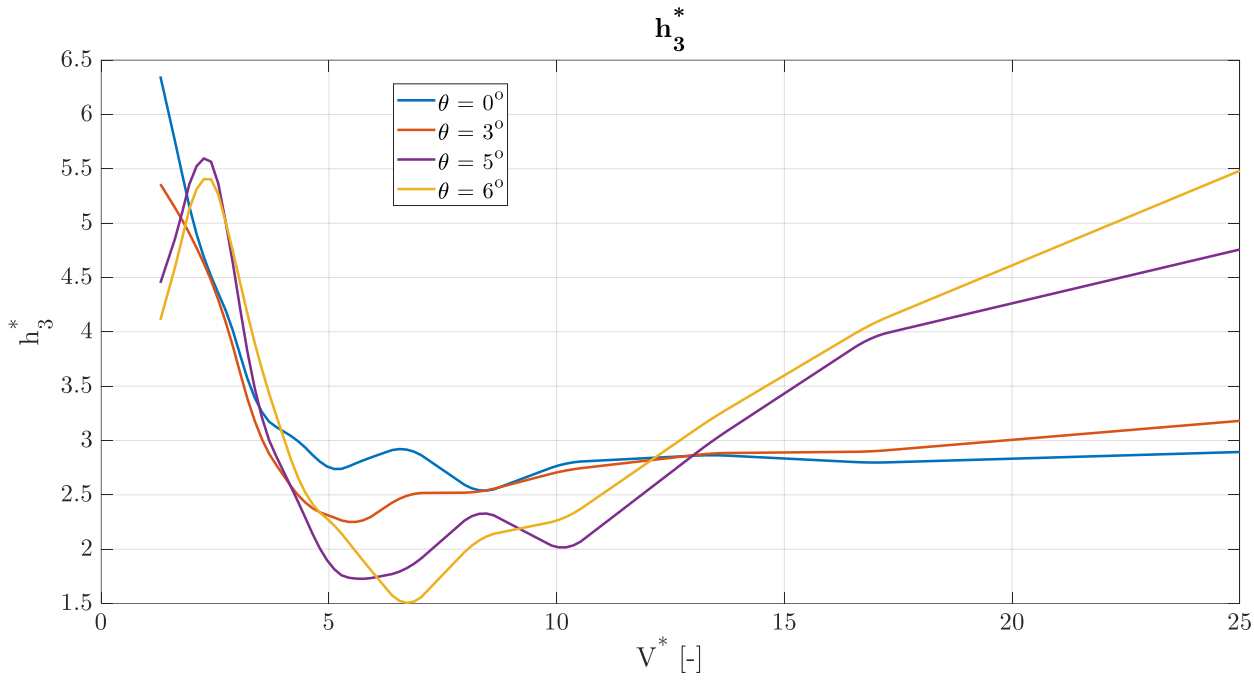

Figure 2.28. Polimi lift flutter derivative h_3^*.

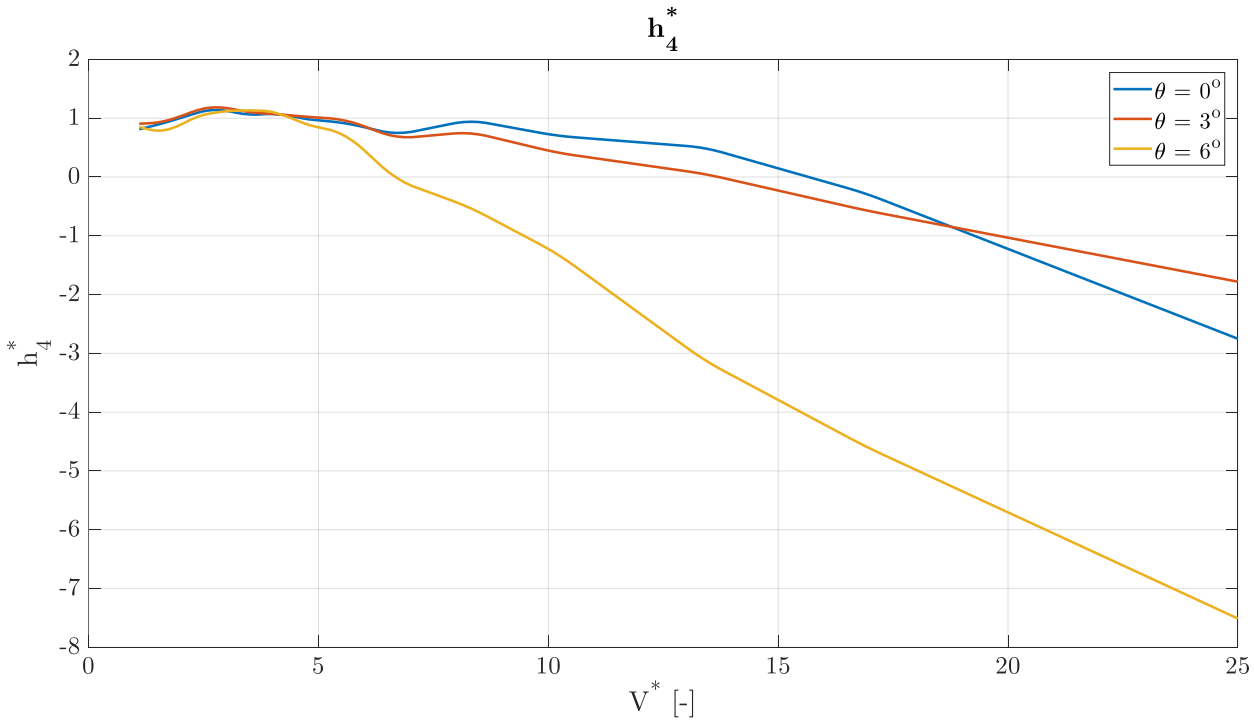

Figure 2.29. Polimi lift flutter derivative h_4^*.

Once the flutter derivatives are identified, it is possible to define the values of B_{1z} and $B_{1\theta}$ employed in the QSTC aeroelastic damping matrix (section 1.2) by the ratios:

$$B_{1z} = \frac{h_2^*}{h_1^*} B \tag{2-24}$$

$$B_{1\theta} = \frac{a_2^*}{a_1^*} B \tag{2-25}$$

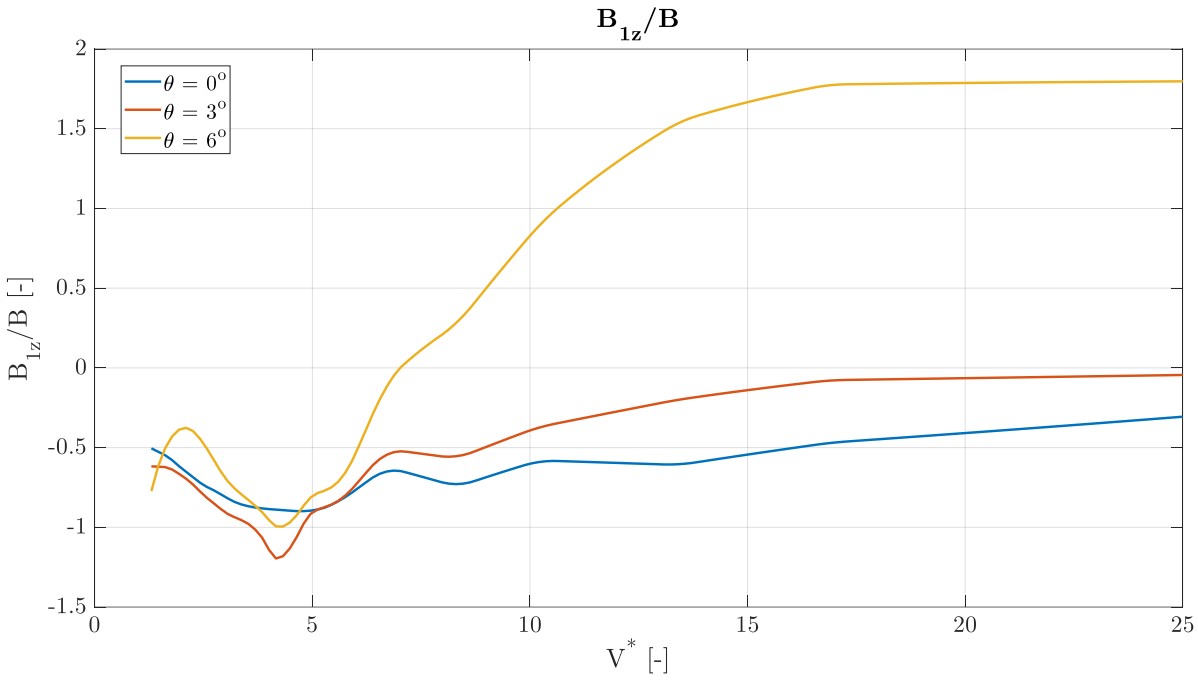

Figure 2.30. B_{1z}/B as a function of V^*.

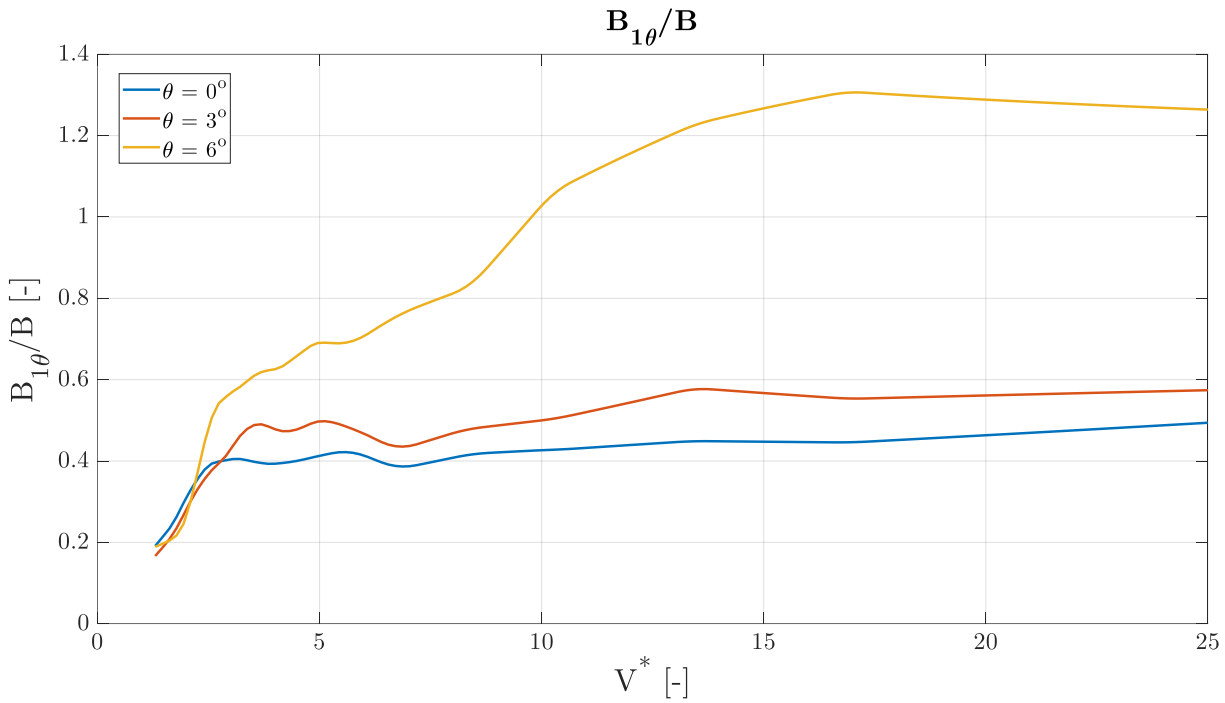

Figure 2.31. $B_{1\theta}/B$ as a function of V^*.

It is to be highlighted that these experimentally identified parameters of B_{1z} and $B_{1\theta}$ are aimed at "correcting" the QST formulation at high values of V^* where it fails by itself to describe the deck's response. Hence, it is called the Correct Quasi Steady Theory QSTC.

At high values of the reduced velocity V^*, the aeroelastic stiffness and damping matrices written with the flutter derivatives should converge to those written with the QSTC. Table 2.1 shows these theoritcal values:

PoliMi Notation	**QSTC**
h_1^*	$K_L + C_D$
h_2^*	$(K_L + C_D)\frac{B_{1z}}{B}$
h_3^*	K_L
$h_4^* \frac{\pi}{2V_\omega^{*2} B}$	0
a_1^*	K_M
a_2^*	$K_M \frac{B_{1\theta}}{B}$
a_3^*	K_M
$a_4^* \frac{\pi}{2V_\omega^{*2}}$	0

Table 2.1. QSTC coefficients to which the flutter derivatives converge at high V^*.

In the following tables the above values for the flutter derivatives and for the QSTC matrices are reported. The values of the B_{1z} and $B_{1\theta}$ coefficients are

Ang [°]	$\boldsymbol{K_L + C_D}$	$\boldsymbol{(K_L + C_D)\frac{B_{1z}}{B}}$	$\boldsymbol{K_L}$	$\boldsymbol{K_M}$	$\boldsymbol{K_M \frac{B_{1\theta}}{B}}$
0	3.288	-1.007	3.25	1.095	0.541
3	5.239	-0.232	5.201	1.448	0.8313
5	5.993	(-)	5.946	1.481	(-)
6	6.524	11.724	6.467	1.499	1.895

Table 2.2. QSTC values to which the flutter derivatives converge at high V^*.

Ang [°]	$\boldsymbol{h_1^*}$	$\boldsymbol{h_2^*}$	$\boldsymbol{h_3^*}$	$\boldsymbol{h_4^* \frac{\pi}{2V_\omega^{*2} B}}$
0	2.833	-0.8672	2.894	-0.2334
3	3.173	-0.141	3.181	-0.1510
5	(-)	5.579	4.758	(-)
6	6.523	11.72	5.483	-0.6370

Table 2.3. Lift flutter derivatives at V^*=25.

Ang [º]	a_1^*	a_2^*	a_3^*	$a_4^* \frac{\pi}{2V_\omega^{*2}}$
0	0.982	0.485	1.032	-0.1072
3	1.007	0.5778	1.031	-0.0709
5	(-)	1.07	1.293	(-)
6	1.890	2.389	1.541	-0.1749

Table 2.4. Moment flutter derivatives at V^*=25.

Aerodynamic admittance functions

The buffeting forces are written employing the aerodynamic admittance functions contained in its homonymous matrix $[A_M]$ as follows:

$$\underline{F_{buff}} = [A_M] \cdot \underline{b} \tag{2-26}$$

Where $\underline{b}$ is a vector that contains the incoming turbulence. Due to the instrumentation available in the GVPM, it was not feasible to generate a well defined harmonic turbulence in the longitudinal direction of the wind flow v/V. Instead, a well defined harmonic turbulence could be succesfully generated in the vertical component of the wind flow w/V. Due to the above, the turbulence vector results $\underline{b} = w/V$. In consequence, the buffeting force vector is computed as follows:

$$\underline{F_{buff}} = \begin{bmatrix} F_z \\ F_\theta \end{bmatrix} = \begin{bmatrix} \chi_{zw} \\ \chi_{\theta w} \end{bmatrix} \cdot \frac{w}{v} \tag{2-27}$$

Where χ_{zw} and $\chi_{\theta w}$ are the aerodynamic admittance functions for F_z and F_θ due to the incoming vertical turbulence of the wind flow, respectively.

A method used in the GVPM aimed at identifying the aerodynamic admittance functions as a complex transfer function in which the input is a well defined harmonic wind turbulence generated by an active device as displayed in Figure 2.11. and the output are the aerodynamic forces F_z and F_θ, recorded by the pressure taps, is employed. Such a procedure is schematically displayed in Figure 2.32.

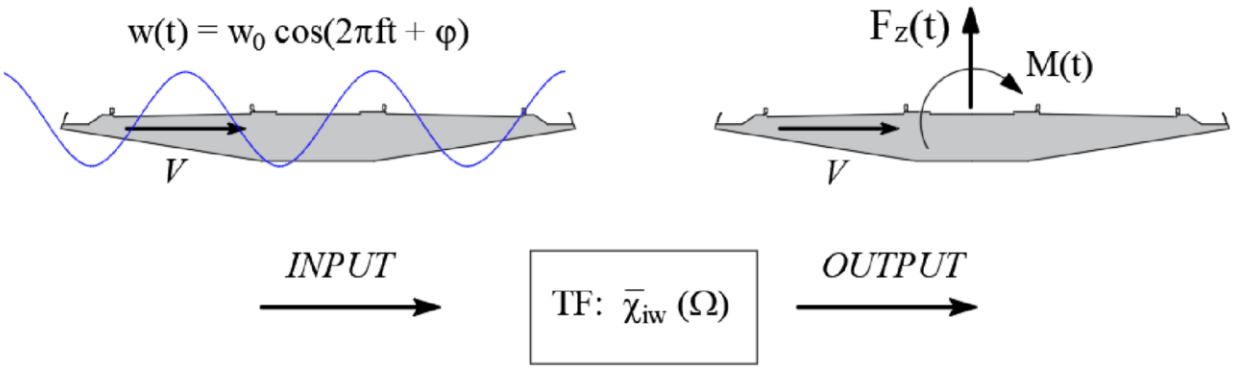

Figure 2.32. Procedure to define the aerodynamic admittance functions

The active turbulence generator is able to produce a harmonic fluctuation of the vertical component of the wind speed at different frequencies, ranging from 0.5 Hz to 3 Hz. This component changes the wind angle of attack α, due to the incoming turbulence w/V. The admittances are functions of the mean angle of attack θ_0 and of the the reduced velocity on which the tests are conducted. The wind flow inside the wind tunnel was set to flow at velocities ranging from 6 m/s to 15 m/s, hence allawoing a wide range of reduced velocity values of V^*=1.7 ~ 25. The complex aerodynamic admittance functions are displayed in the Figure 2.33 and Figure 2.34 reported as its amplitude and phase.

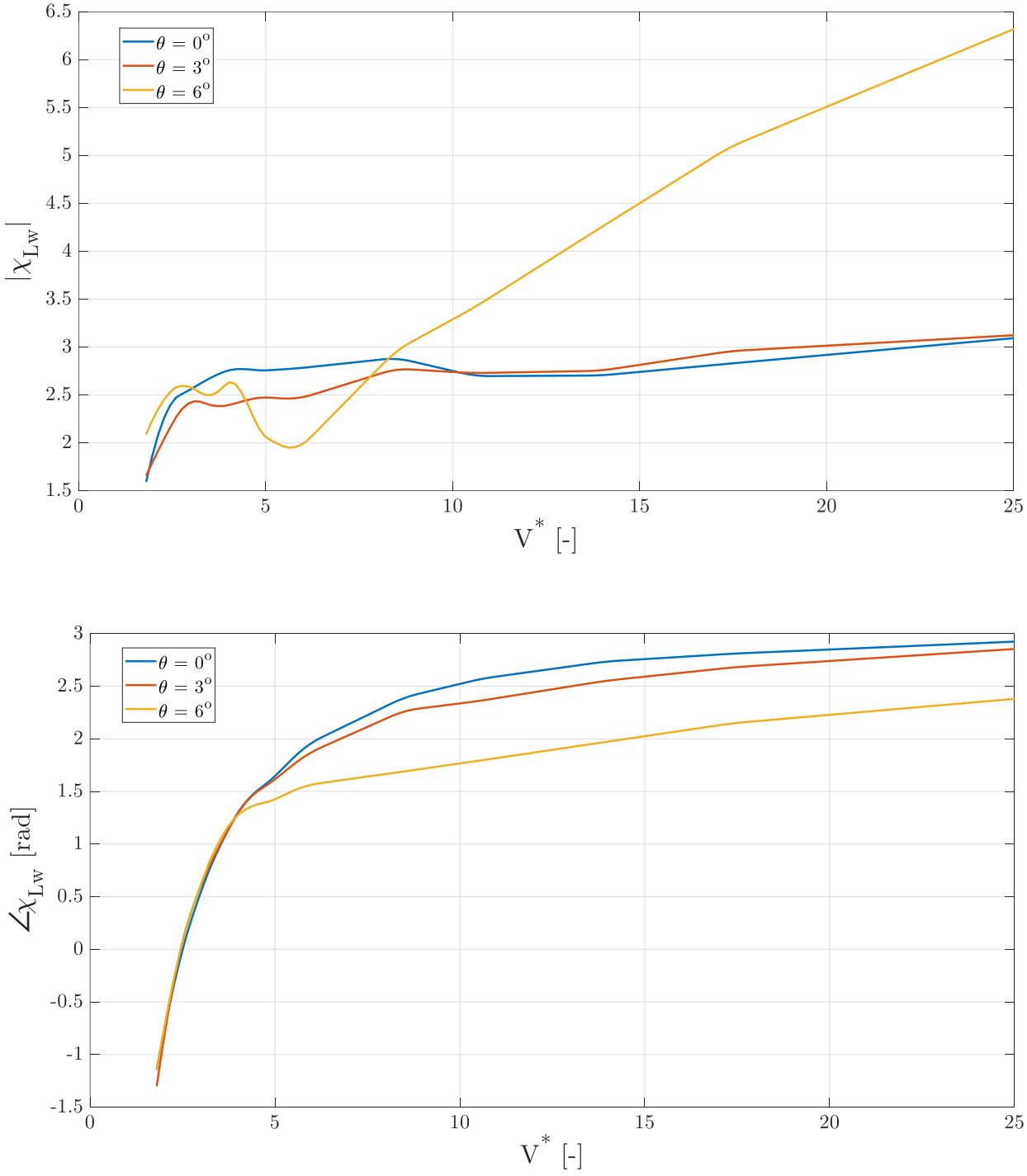

Figure 2.33. Vertical aerodynamic admittance function χ_{zw}; amplitude and phase.

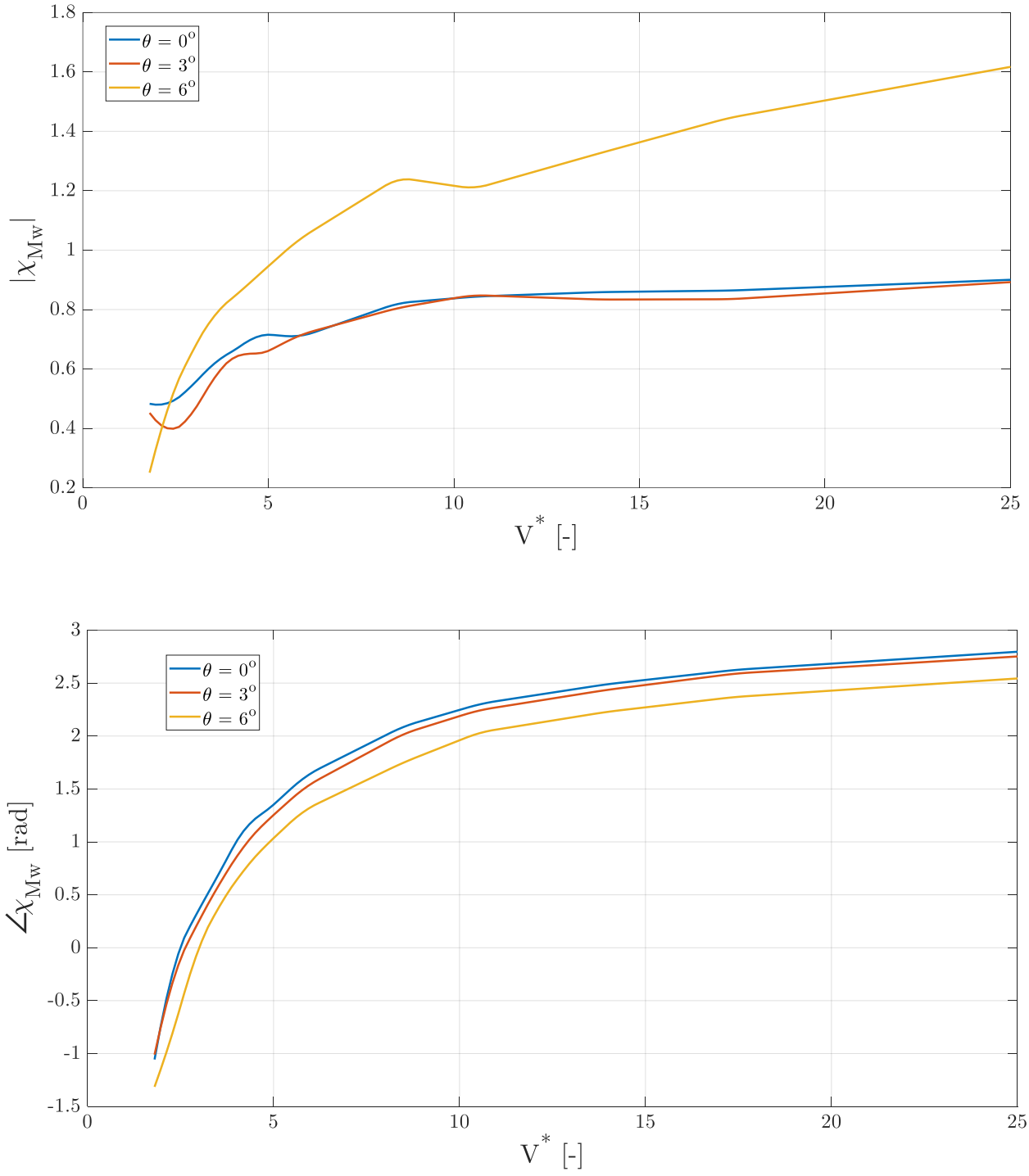

Figure 2.34. Torsional aerodynamic admittance function $\chi_{\theta w}$; amplitude and phase.

2.4.3 Suspended model tests

Up to this point, aerodynamic parameters that characterize the sectional model's aerodynamic behavior have been identified. On the following, structural parameters will be obtained in order to write the structural mass, damping, and stiffness matrices; $[M_s], [R_s], [K_s]$, respectively. To this aim, the hydraulic actuators were removed from the sectional model, and the model was suspended by a set of springs which were attached to steel cables. Eight vertical cables were attached at the extremities of the sectional model and connected it to a steel frame in such a way that four of them were placed on each end as depicted in Figure 2.35.

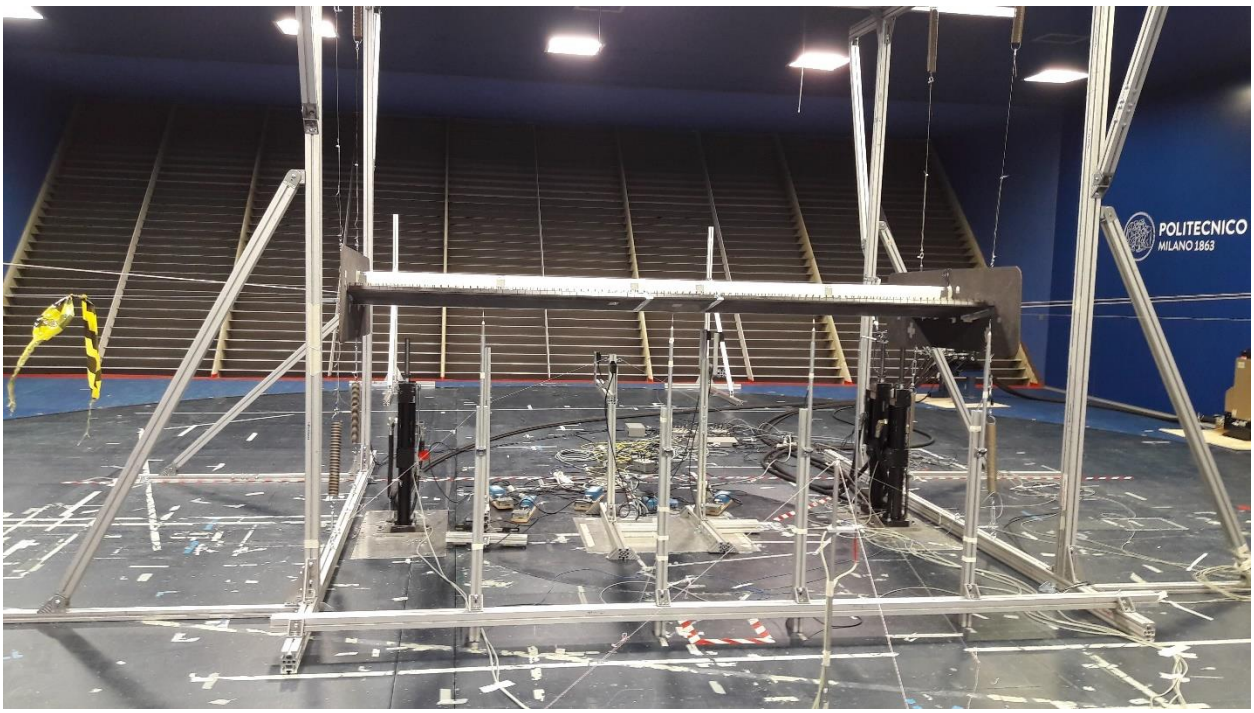

Figure 2.35. Suspended sectional model; the springs are observed attached to the steel cables.

In order to investigate the stability of the deck, 2 different configurations were adopted. *Configuration 1* had a spacing between the vertical steel cables connected at each end of the deck sectional model of 0.88 m, while *configuration 2* had a spacing between the cables of 1.18 m and no steel cables below the sectional model. On both configurations, the horizontal oscillations (y d.o.f.) were restrained. The aim of establishing a second configuration of the sectional model is to

decrease the stiffness (thus, four of the eight vertical cables were removed) to be able to obtain a deck response close to the flutter instability. This phenomenon could not take place in *configuration 1* as the flutter velocity is higher than the maximum mean wind speed capacity of the wind tunnel (≈15 m/s).

The procedure employed to identify the damping ratios and natural frequencies for the z and θ degrees of freedom; ξ_z, ξ_θ, f_z and f_θ, respectively, consisted in setting the incoming wind's velocity at the desired value and then applying an initial displacement either in z or in θ to the sectional model. In order to avoid a superposition of the dynamic oscillations on a static response of the deck to V_m, the deck sectional model's static position is on purposely set at a rotation of θ_0=3°, position in which the moment coefficient C_M assumes a value of 0 as reported in Figure 2.18. The deck then oscillates in free vibration around its static equilibrium position, and applying the equations of the logarithmic decrement (under the assumption that viscous damping takes place), the damping ratio and the natural frequencies are determined as a function of the incoming wind speed. In the following equations, t_0 is the time instant of a selected initial peak $x(t_0)$ within the free vibration time history of the generic coordinate x (which in this case are the degrees of freedom z and θ), T is the identified period of oscillation, and n is the number of the counted subsequent peaks until the following chosen second peak $x(t_0+nT)$.

$$\delta = \frac{1}{n} \ln \frac{x(t_0)}{x(t_0 + nT)} \tag{2-28}$$

$$\xi = \frac{\delta}{\sqrt{\delta^2 + 4\pi^2}} \tag{2-29}$$

$$f_n = \frac{1}{2\pi} \sqrt{\frac{4\pi^2 + \delta^2}{T}} \tag{2-30}$$

For the elastically suspended sectional model with no incoming wind, the following parameters were identified:

Modal Parameters

	Configuration 1	*Configuration 2*
$m_{y,z}$ (kg/m)	17.42	17.42
I_θ (kg m)	2.59	2.59
f_z (Hz)	1.92	1.37
f_θ (Hz)	2.38	2.08
ξ_z (%)	0.37	0.58
ξ_θ (%)	0.38	0.39

Table 2.5. Modal parameters of the two configurations of the elastically suspended sectional model.

Once the wind turbine is activated, the variation of the damping ratio and the natural frequency of the deck with an increasing wind flow can be captured. Figures Figure 2.36 through Figure 2.39 report the damping ratios and the natural frequencies as a function of the incoming wind velocity for *configuration 1* and *configuration 2*, respectively.

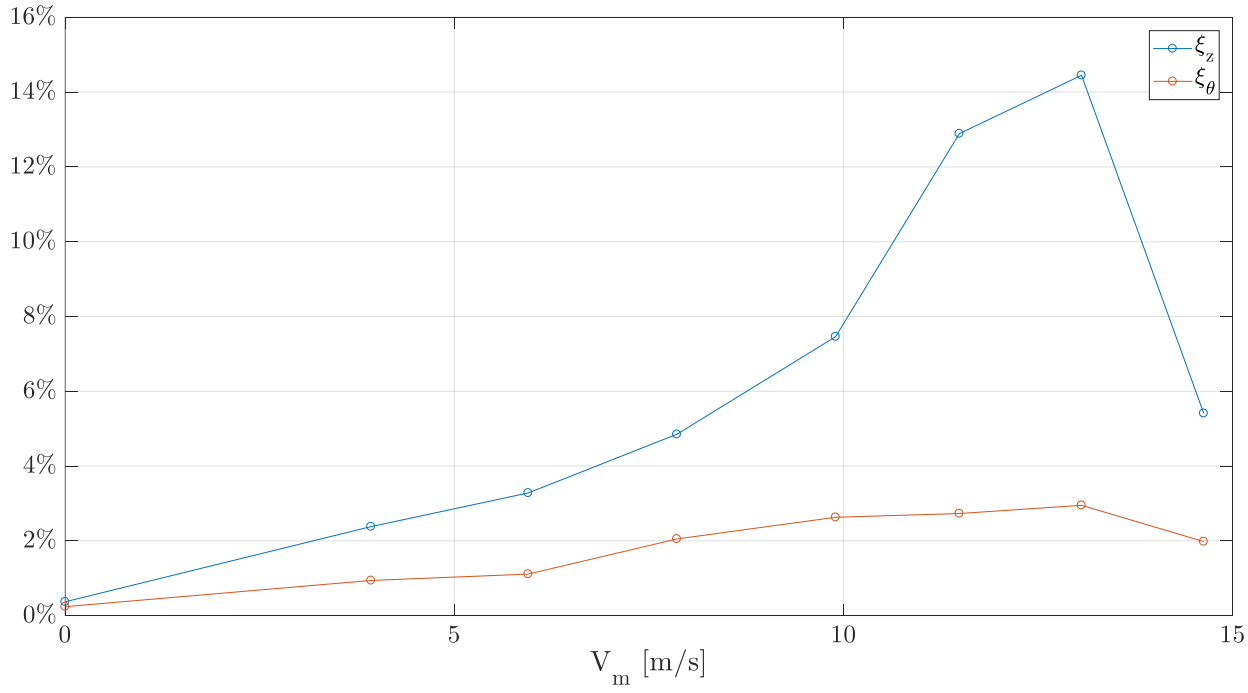

Figure 2.36. *Configuration 1:* damping ratios as a function of the incoming wind speed.

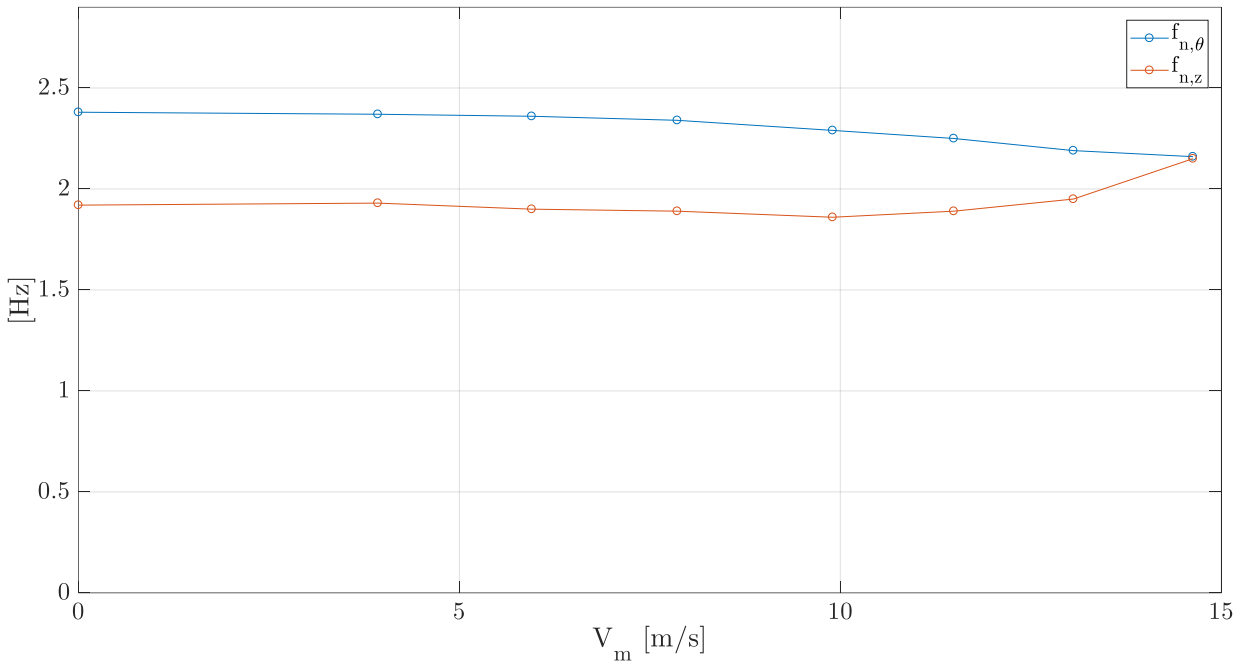

Figure 2.37. *Configuration 1*: natural frequencies as a function of the incoming wind speed.

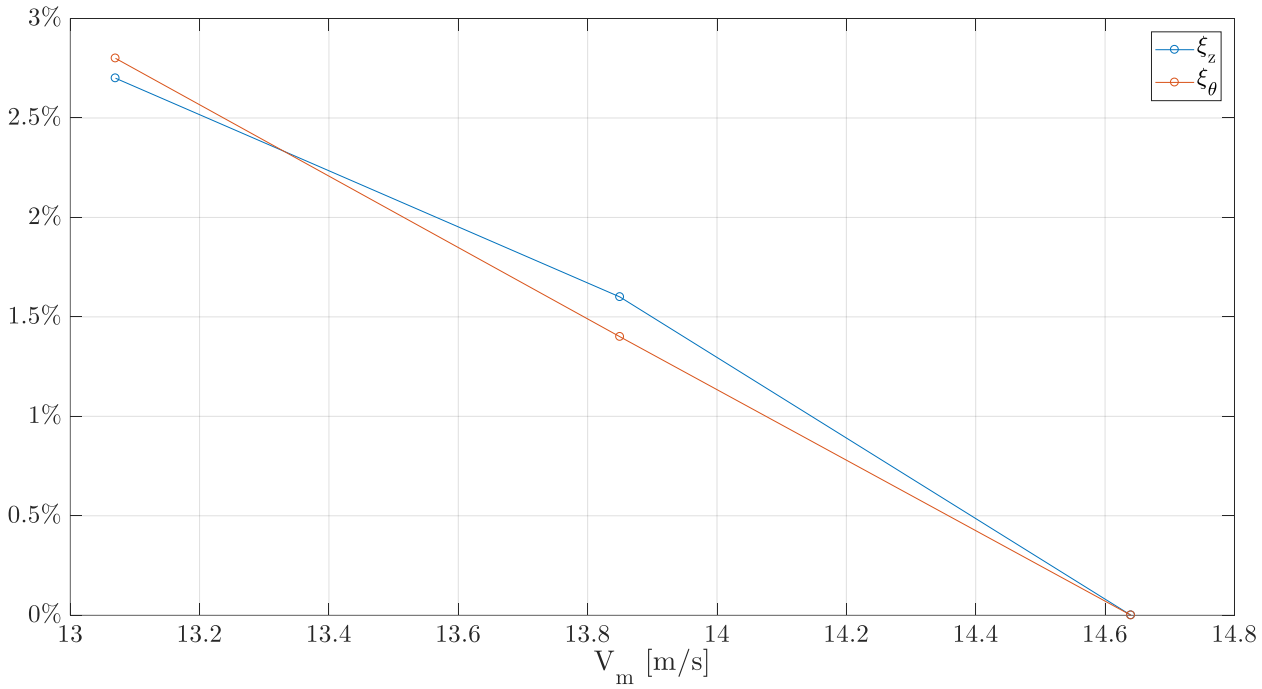

Figure 2.38. *Configuration 2*: Damping ratios as a function of the incoming wind speed.

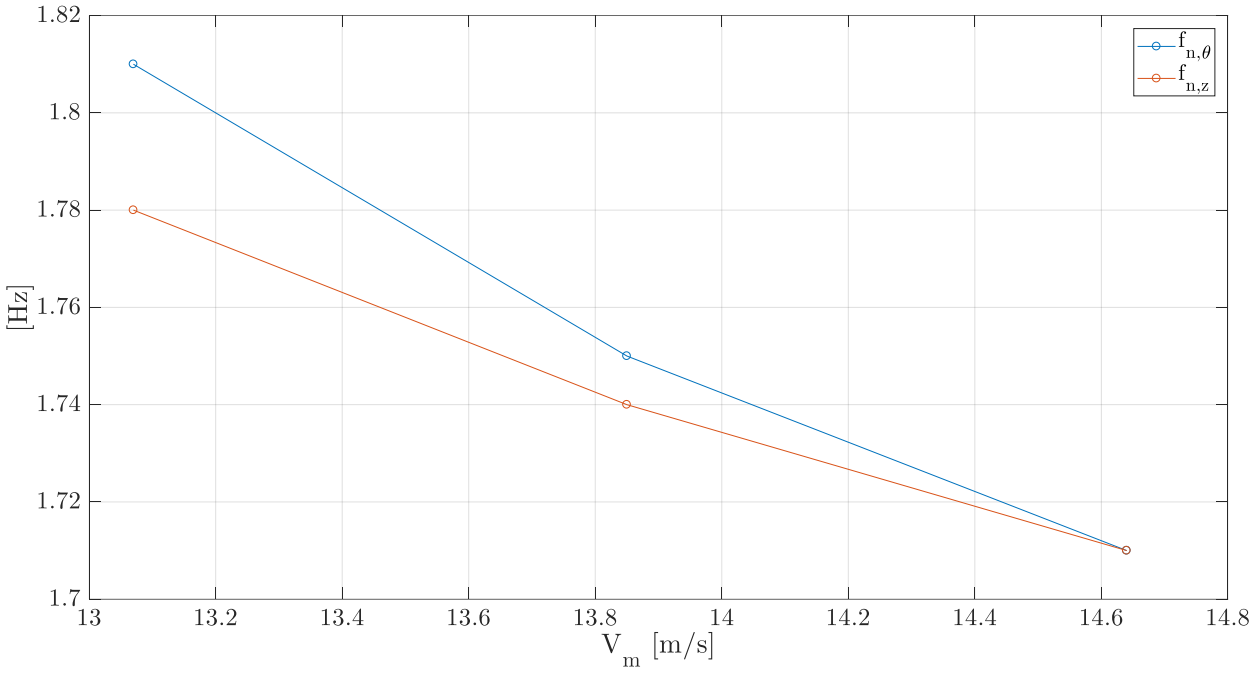

Figure 2.39. *Configuration 2*: Natural frequencies as a function of the incoming wind speed.

It is observed in figures Figure 2.36 and Figure 2.37 that at high mean wind speeds, the damping ratios ξ_z and ξ_z start to decrease, and the natural frequencies f_{nz} and $f_{n\theta}$ converge. As a matter of fact, at high values of the mean wind speed (V_m>14 m/s) a vibration mode appears in which the oscillation components of the deck in z and θ are coupled. This was made evident when in the wind tunnel the vertical oscillations (z) were excited at high mean wind speed by imposing an initial vertical displacement and the deck started to oscillate in free vibration with displacements on both components z and θ.

Only the damping ratios and natural frequencies at high values of the incoming wind speed were investigated for *configuration 2*. It is noted that flutter instability is successfully found at V_m=14.64 m/s. This is evident given that at this speed the torsional and vertical natural frequencies coincide, and the damping ratios are zero, hence, allowing for an uncontrolled coupling of the vertical and torsional oscillations of the deck.

2.4.4 Forced motion tests

The active turbulence generator, made up of a series of wings linked together, produces a wind tunnel flow with an almost constant horizontal velocity component and a well-defined harmonic oscillating vertical velocity component (see Figure 2.40). Employing this generator, it was possible to excite the sectional model with buffeting forces, while it was left free of moving under the turbulent flow, with the steel cable arrangements of *configuration 1* and *configuration 2*.

Several tests were conducted at different wind velocities and frequencies of the incoming wind speed. As a matter of fact, mono-, bi- and tri-harmonic turbulence excitations were generated by the active turbulence generator. In order to obtain high values of reduced velocities V^*, low values of frequencies were generated along with high wind speeds. Reduced velocities as high as V^*=482.05 were attainable by employing an oscillation frequency of 0.025 Hz and a mean wind speed of 14.10 m/s. It is expected that at high reduced velocities (or low frequencies), the RM model will have a negligible contribution to the deck's response, and that the QSTC will be able to describe the deck's response. The time histories and spectra of the degrees of freedom z and θ, and of the force coefficients C_L and C_M. will be reported in further detail in Chapter 3 where the experimental evidence of the non-linearities will be discussed.

Figure 2.40. Harmonic oscillating wind velocity generated by an active turbulence generator.

Configuration 1

Test	V [m/s]	f [Hz]	**A** [cm]	**phase** [º]	V^* [-]
1-1	13.30	0.05	3	-	227.35
		2.20	1	-	5.17
1-2	13.30	0.10	2.5	-	113.68
		2.20	1	0	5.17
1-3	13.30	0.025	2.5	-	454.70
		2.20	1	0	5.17
1-4	13.30	0.025	3	-	454.70
		2.20	1	0	5.17
1-5	13.30	0.05	2	-	227.35
		0.10	1	0	113.68

Table 2.6. Forced motion tests conducted over *configuration 1.*

1-6	13.30	0.05	2	-	227.35
		0.10	1	0	113.68
		2.20	1	0	5.17
1-7	13.30	0.05	2	-	227.35
		0.1	1	90	113.68
		2.2	1	0	5.17
1-8	13.30	0.05	2	-	227.35
		0.1	1	90	113.68
1-9	13.30	0.05	2.5	-	227.35
		1.8	2	0	6.32
1-10	6.00	0.05	2.5	-	102,56
		2.35	1	0	2.18
1-11	6.00	0.05	3	-	102.56
		1.90	2	0	2.70

Table 2.6. (Continuation) Forced motion tests conducted over *configuration 1.*

Configuration 2

Test	V **[m/s]**	f **[Hz]**	**A [cm]**	**phase [º]**	V^* **[-]**
2-1	14.10	0.05	3.5	-	241.03
		1.75	0.3	0	6.89
2-2	14.10	0.025	3.5	-	482.05
		1.75	0.3	0	6.89

Table 2.7. Forced motion tests conducted over *configuration 2.*

Chapter 3

Experimental Evidence of Non-Linearities

3.1 Introduction

The non-linearities present in the bridge aerodynamic problem are expressed through a non-linear relationship between the bridge's motion and the incoming wind angle of attack. Thus, the experimental campaign here presented has as a scope to deepen the knowledge of the behavior of a deck with a highly non-linear relationship of its response with the incoming wind-flow. In order to achieve this, the response of a bluff-like deck to a turbulent wind excitation must be explored. In consequence, it was decided to add to the deck sectional model of the BB3 a scaled train that would change the behavior of the BB3 sectional model alone, which resembles a streamlined body, to a sectional model whose behavior would be that of a bluff-like body.

In the present chapter, the experimental evidence of non-linearities are presented. The results of specific wind tunnel tests performed over the BB3 sectional model without a train (A. Pellegri 2017) are displayed in order to contrast them with the behavior of the BB3 sectional model with the train (Chapter 2). A deep look is performed over the values of the static force coefficients and the flutter derivatives of both sections, and how they explain the unequal motions of both models.

3.2 Aerodynamic coefficients

Static Aerodynamic Coefficients

The static aerodynamic coefficients of the BB3 sectional model vary with the presence of a train. It is noted a shift in the angle of attack for which the moment coefficient is zero. For the BB3 section without a train (BB3NT) C_M=0 at $\alpha \cong 0^o$, meanwhile for the BB3 section with a train (BB3T) C_M=0 at $\alpha \cong 3^o$. This implies that the static equilibrium position for the section with a train will take place at θ_0=3°.

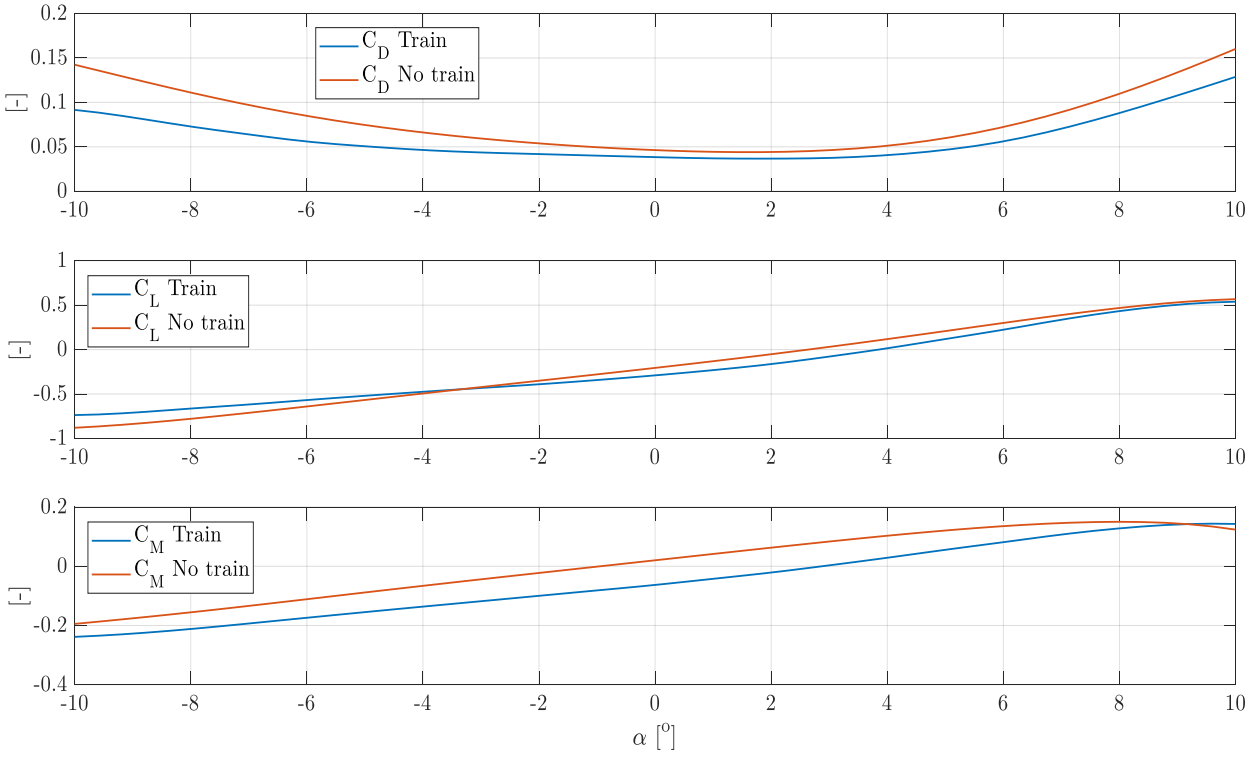

Figure 3.1. Static aerodynamic coefficients of the BB3 sectional models with a train and without a train.

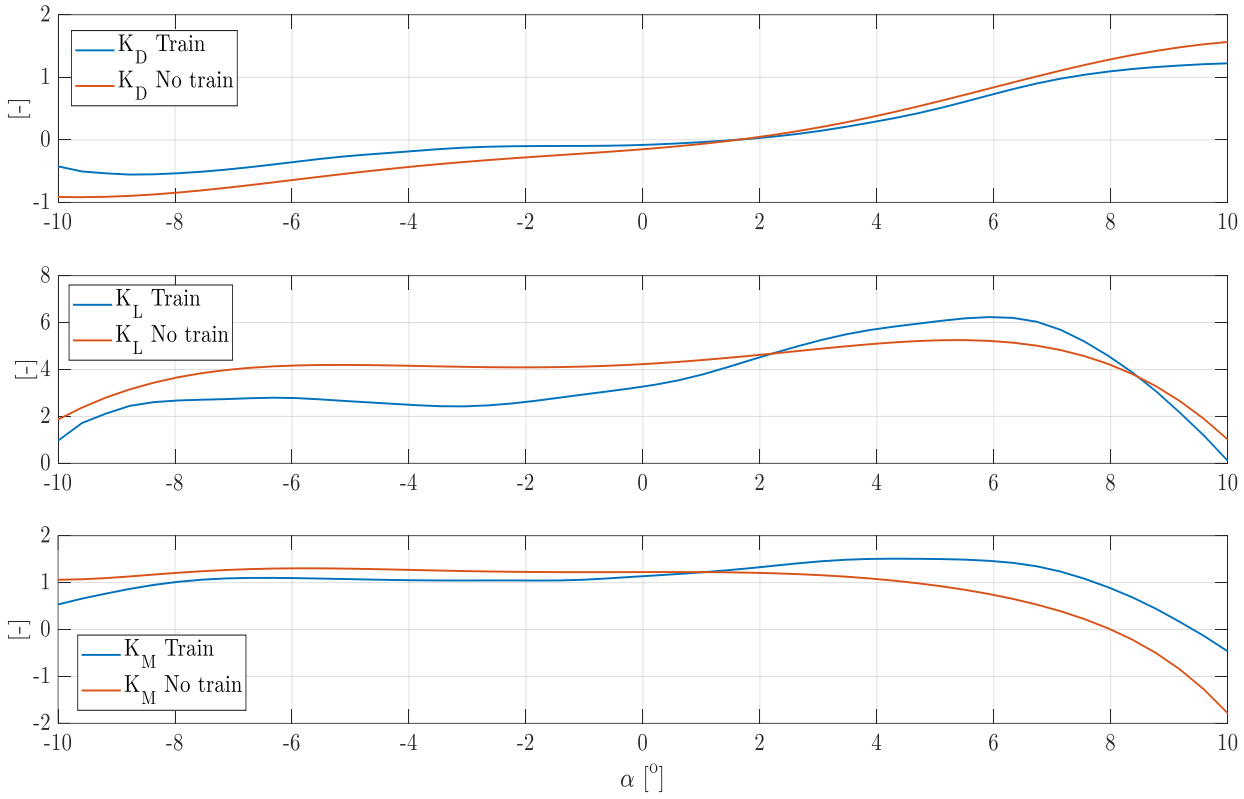

Figure 3.2. Static aerodynamic coefficients derivatives of the BB3 sectional models with a train and without a train.

On the other hand, the static aerodynamic coefficients derivatives are useful in indicating the expected flutter derivatives values at high V^*, where the QST is valid. Hence, $[K_a]$ and $[R_a]$ aeroelastic matrices written using the flutter derivatives should converge to the QSTC $[K_{aQ}]$ and $[R_{aQ}]$ aeroelastic matrices. The theoretical values the flutter derivatives must assume at high V^* are shown in Table 2.1, displayed in the following for convenience.

PoliMi Notation	**QSTC**
h_1^*	$K_L + C_D$
h_2^*	$(K_L + C_D)\frac{B_{1z}}{B}$
h_3^*	K_L
$h_4^*\frac{\pi}{2V_\omega^{*2}B}$	0
a_1^*	K_M
a_2^*	$K_M\frac{B_{1\theta}}{B}$
a_3^*	K_M
$a_4^*\frac{\pi}{2V_\omega^{*2}}$	0

Table 3.1. QSTC coefficients to which the flutter derivatives converge at high V^*.

It is particularly noted in Figure 3.2 that the lift coefficient derivative K_L for the BB3 section without a train exhibits a smooth behavior (almost constant) between α=-7° to α=6°, which is in contrast to the trend of K_L in for the BB3 section with a train that displays a higher variability. Specifically, K_L at α=6° is the double that K_L at α=0°. It is thus expected that the flutter derivatives $h_{1,2,3}^*$ at α=6° double their values at α=0° for high V^* for the section with a train

Flutter Derivatives

A comparison of the flutter derivatives is presented on the following figures, in which the flutter derivatives $a_{1,2,3,4}^*$ and $h_{1,2,3,4}^*$ are presented for the BB3 section with a train (repeated here for convenience) and without it one besides the other.

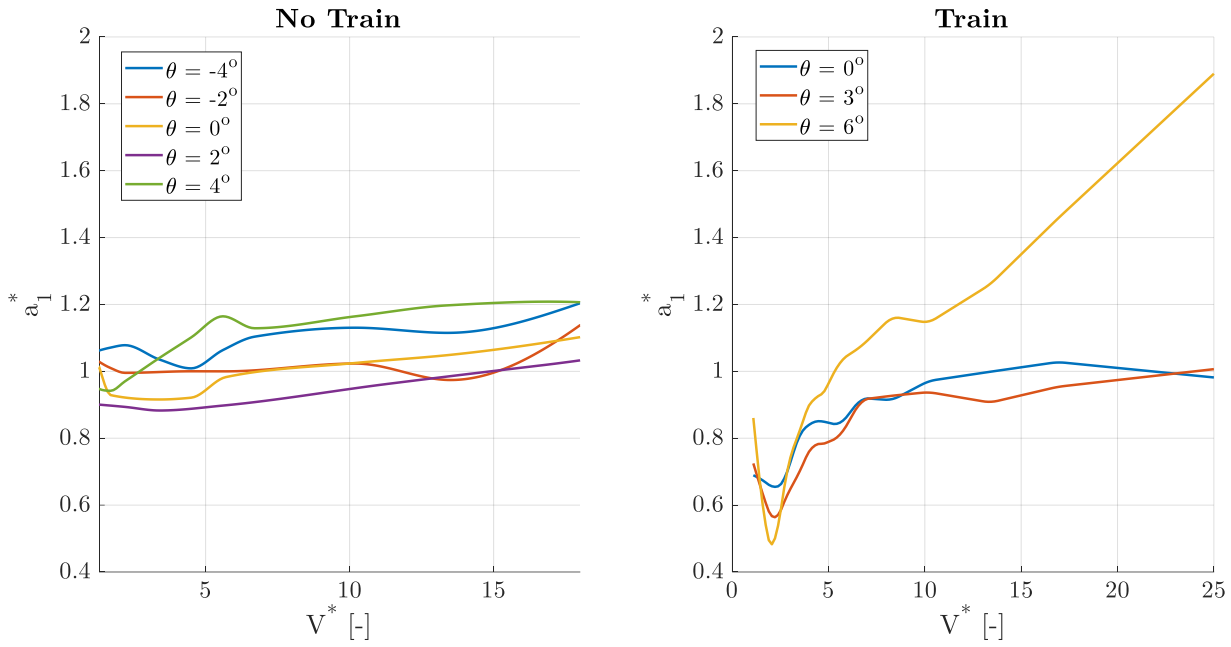

Figure 3.3 a_1^* of the BB3 with a train and without it.

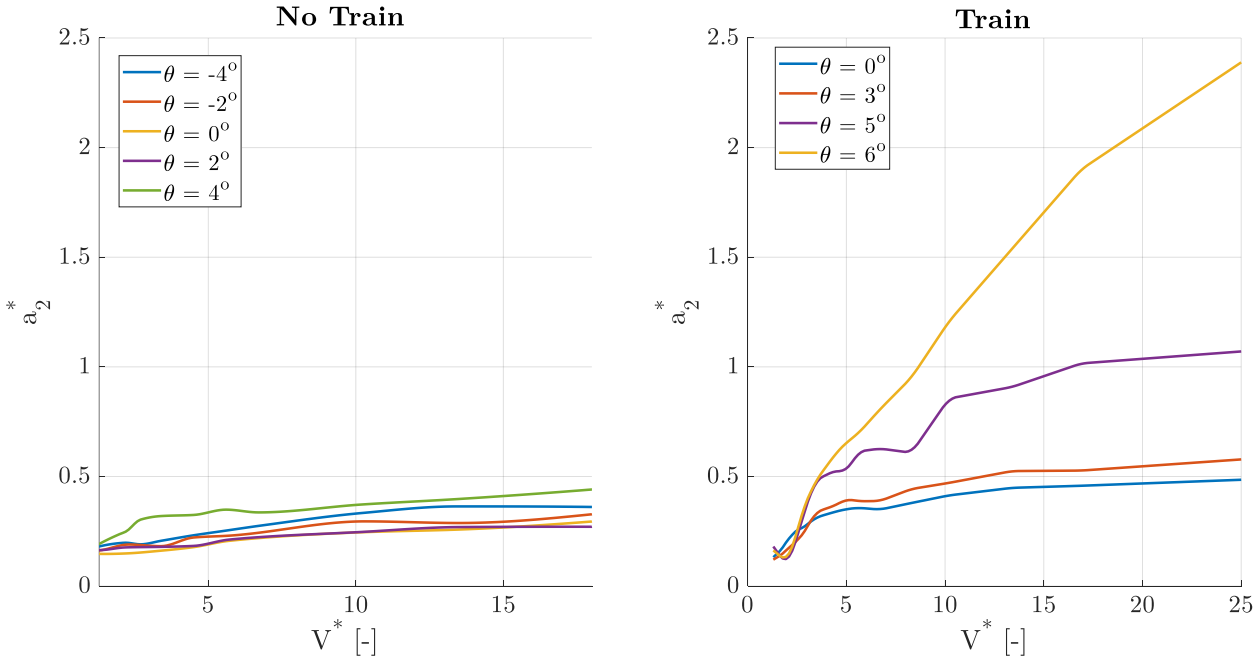

Figure 3.4 a_2^* of the BB3 with a train and without it.

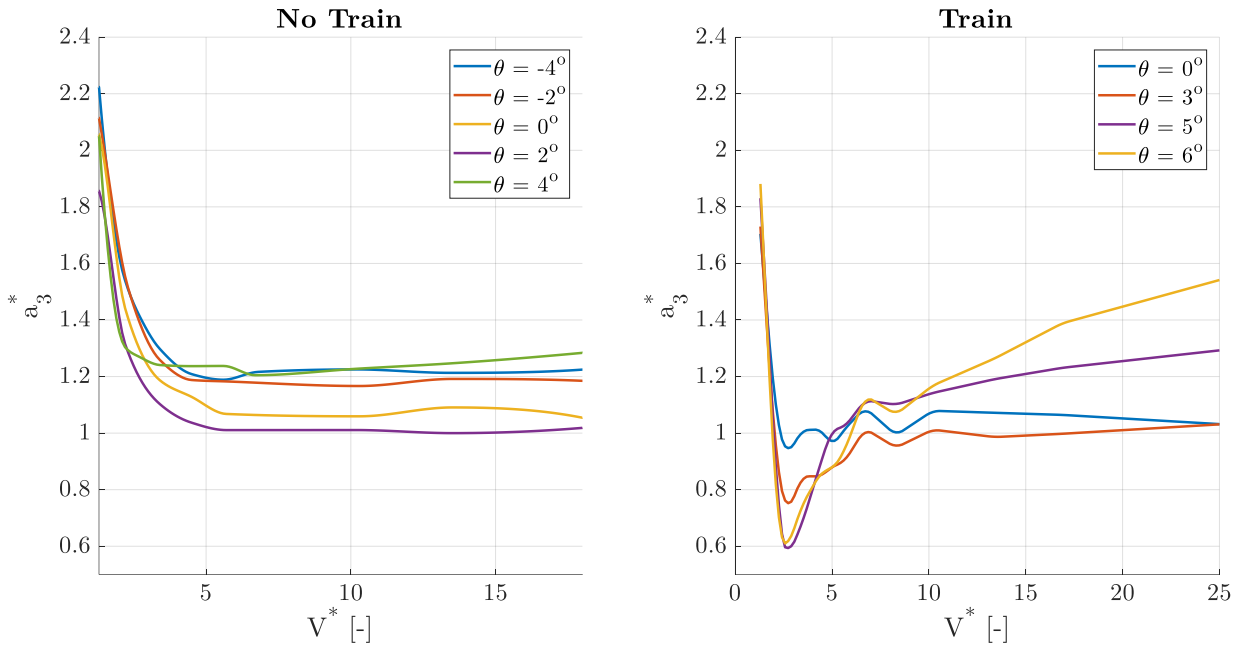

Figure 3.5 a_3^* of the BB3 with a train and without it.

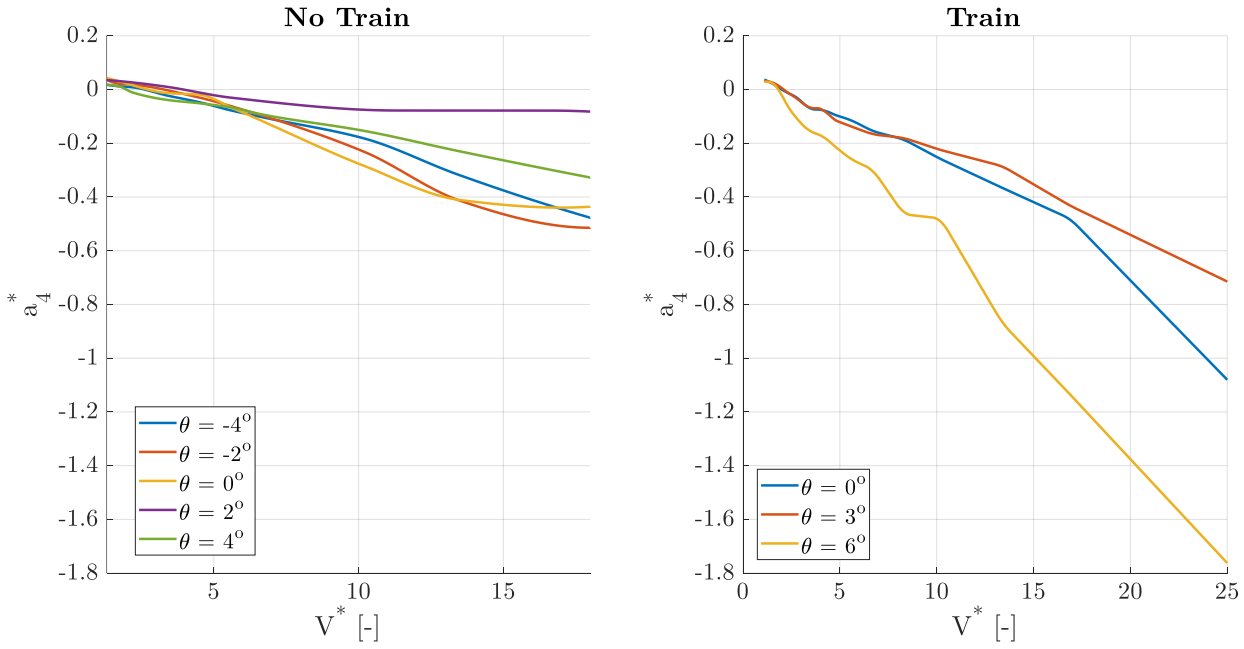

Figure 3.6 a_4^* of the BB3 with a train and without it.

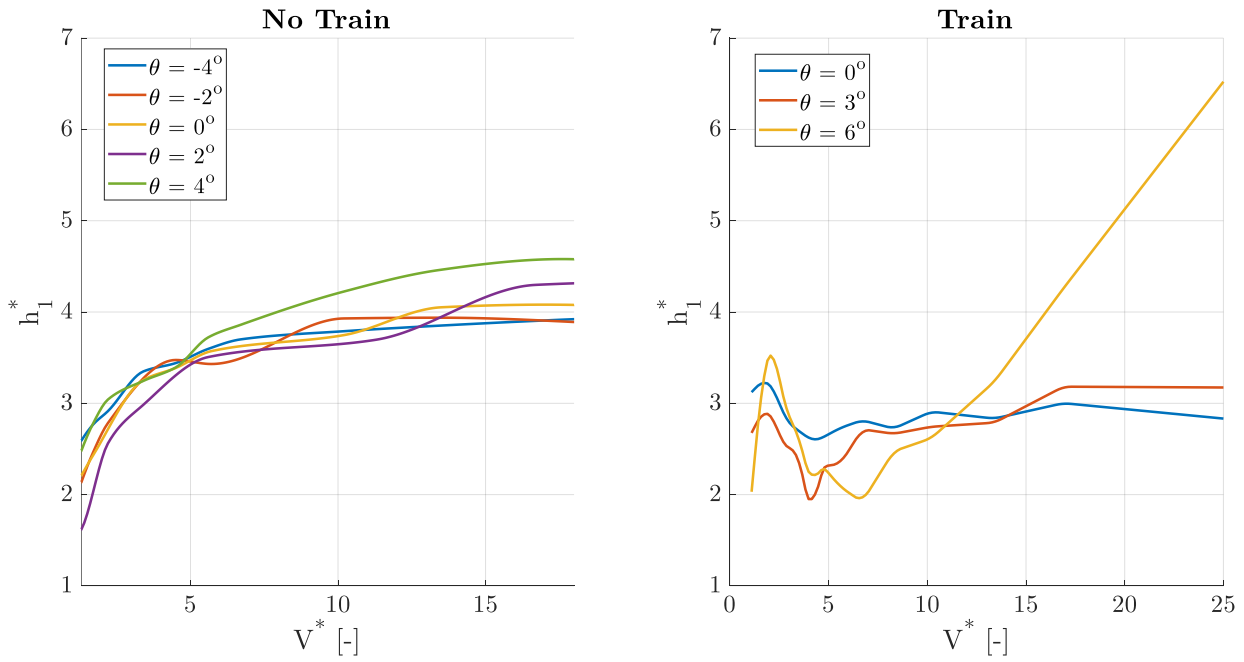

Figure 3.7 h_1^* of the BB3 with a train and without it.

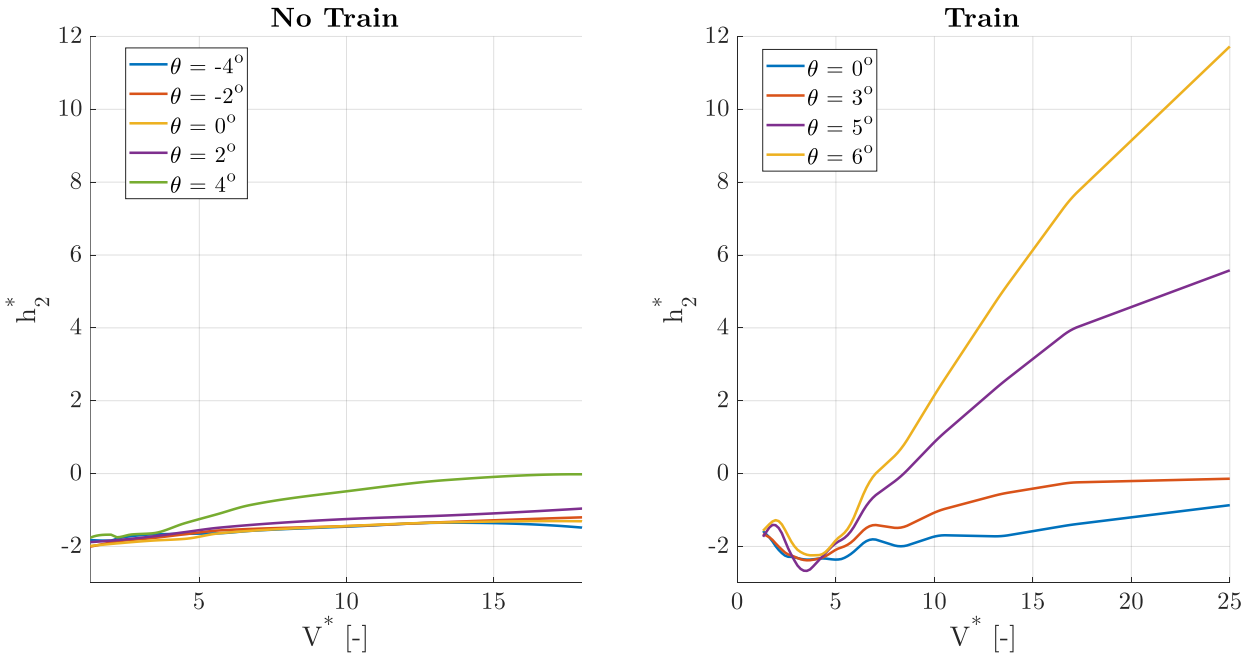

Figure 3.8 h_2^* of the BB3 with a train and without it.

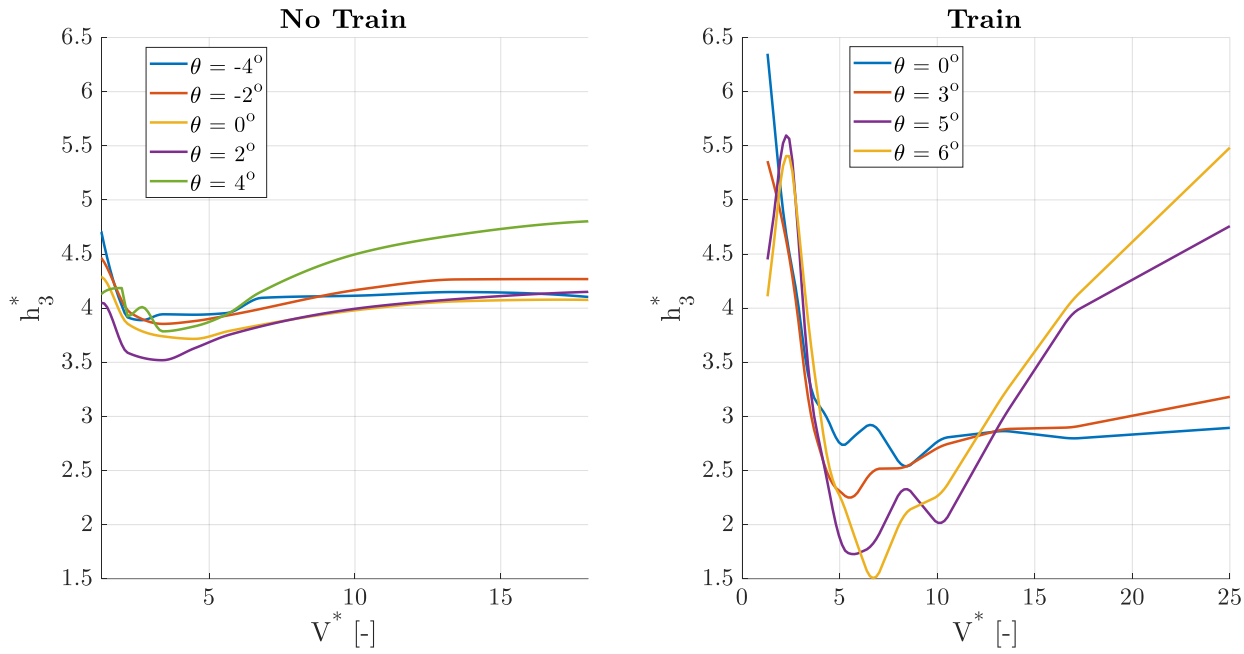

Figure 3.9 h_3^* of the BB3 with a train and without it.

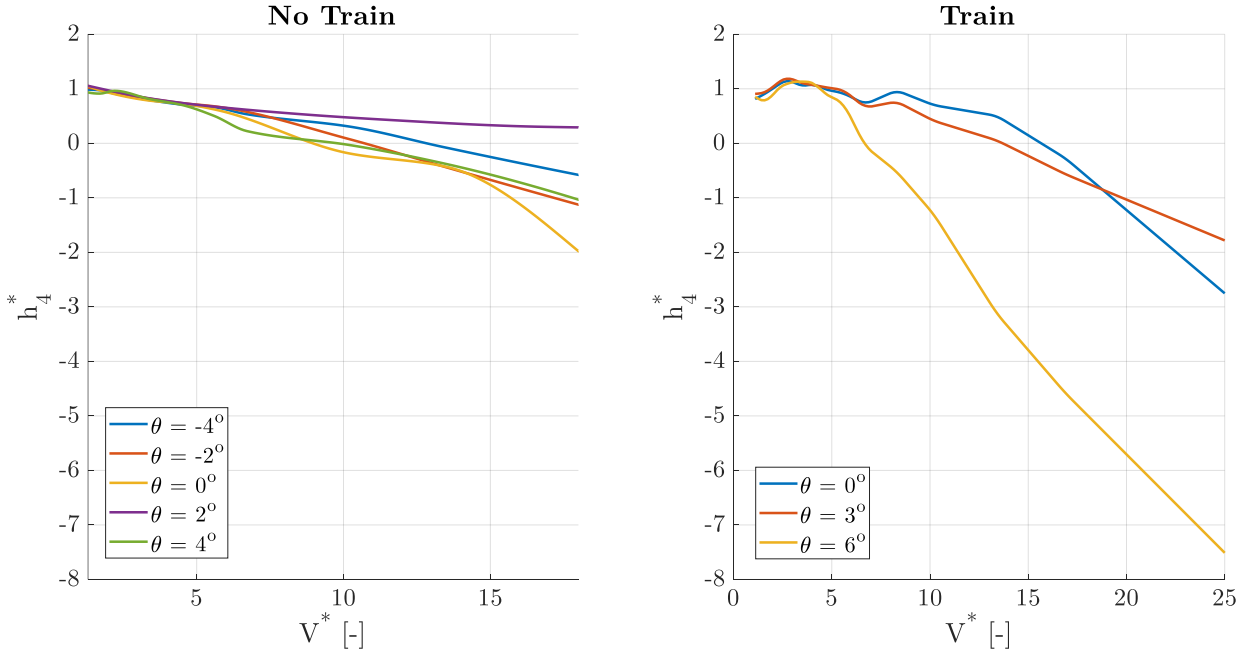

Figure 3.10 h_4^* of the BB3 with a train and without it.

Some observations can be done regarding the behavior of the flutter derivatives at high V^* with respect to the aerodynamic static coefficients. For the BB3 section with a train, we unfortunately

count with information up to V^*=18 only, and for different angles of attack than for the section with a train. It is seen particularly that h_1^* (Figure 3.7) converges to K_L+C_D as expected (Table 3.1). For the section without a train, h_1^* goes from 4 to 4.5 at high V^*, while for the section with a train, h_1^* goes from 3 to 6.5 at high V^*, thus exhibiting a h_1^* at θ=6° of more than the double that at θ=0°. Flutter derivative a_2^* (Figure 3.4) also denotes a stronger dependence in the angle of attack for the section with a train than without it. It is seen that at high V^*, a_2^* for the BB3 section without a train varies from 0.25 to 0.45, almost doubling itself. Meanwhile a_2^* for the BB3 section without a train varies from 0.5 to 2.4, almost five times as much. The aforementioned flutter derivatives h_1^* and a_2^* correspond to the diagonal positions of z and θ degrees of freedom, respectively, in the aeroelastic damping matrix $[R_a]$ (equation (1-51)). In consequence, a variation in these coefficients leads to a modification in the damping of the system, a situation commented in the following paragraph. A special attention is paid to flutter derivative h_4^* (Figure 3.10). It is noted that a very high variability is present in the section with a train than in the section without it. As a matter of fact, h_4^* in the section without a train assumes values ranging from -2 to 0.3, while in the section with a train it assumes values ranging from -7.5 to -2. The importance of h_4^* lies in the fact that it is the diagonal term for the z degree of freedom inside the $[K_a]$ matrix (equation (1-50)). Hence, a stronger dependence of h_4^* in θ_0 implies a stronger dependence of the natural frequency in θ_0. This effect is however shadowed by the fact that h_4^* is divided by V_ω^{*2} in $[K_a]$, and the structural stiffness within $[K_{st}]$ is predominant in the definition of the natural frequency of the deck.

A deeper insight can be explored by taking a look into the transfer functions of the self-excited forces, expressed in equations (1-47) to (1-49), and result as follows:

$$\frac{L^{se}}{-\frac{\dot{z}}{V}} = \frac{1}{2}\rho V^2 B\left(h_1^* + i\frac{\pi^2}{V^*}h_4^*\right) \tag{3-1}$$

$$\frac{L^{se}}{\theta} = \frac{1}{2}\rho V^2 B\left(h_3^* - i\frac{2\pi}{V^*}h_2^*\right) \tag{3-2}$$

$$\frac{M^{se}}{-\frac{\dot{z}}{V}} = \frac{1}{2}\rho V^2 B^2 \left(a_1^* + i\frac{\pi^2}{V^*}a_4^*\right) \tag{3-3}$$

$$\frac{M^{se}}{\theta} = \frac{1}{2}\rho V^2 B^2 \left(a_3^* - i\frac{2\pi}{V^*}a_2^*\right) \tag{3-4}$$

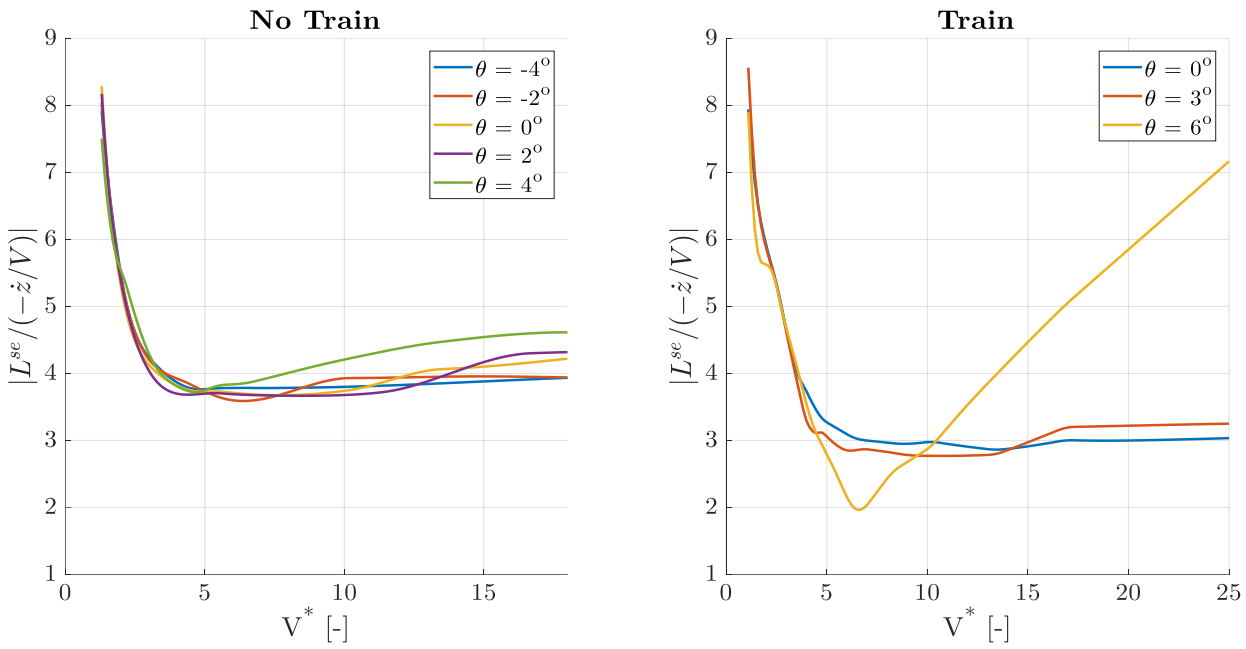

Figure 3.11. Modulus of L-z transfer function of the BB3 section with a train and without it.

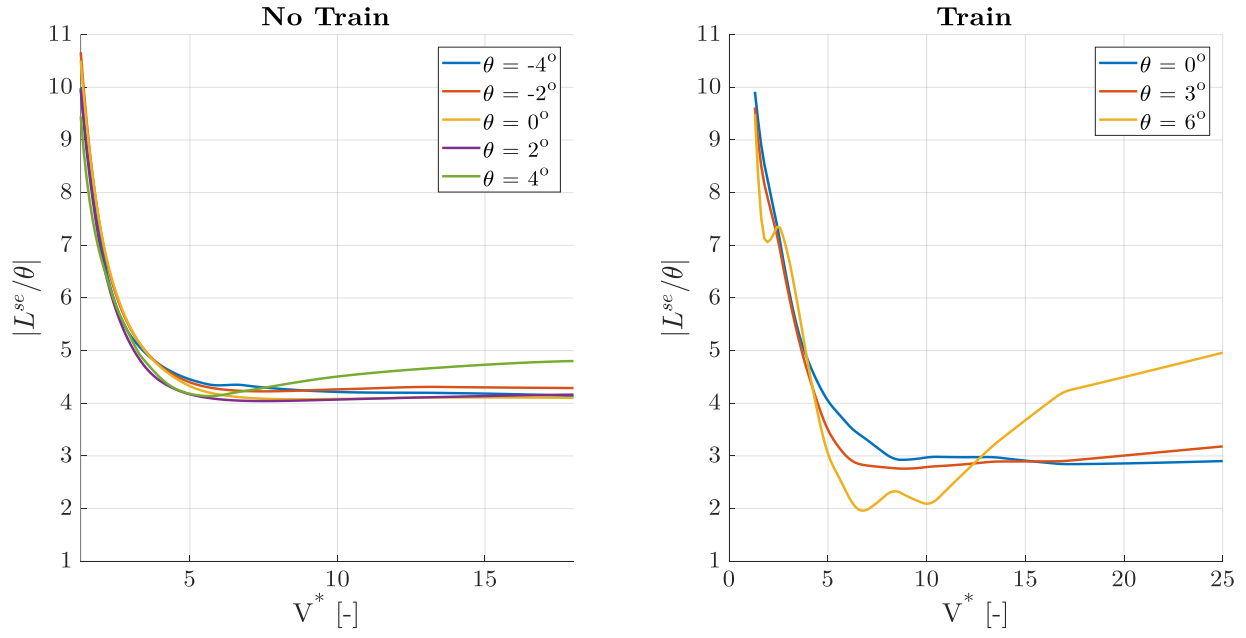

Figure 3.12. Modulus of L-θ transfer function of the BB3 section with a train and without it.

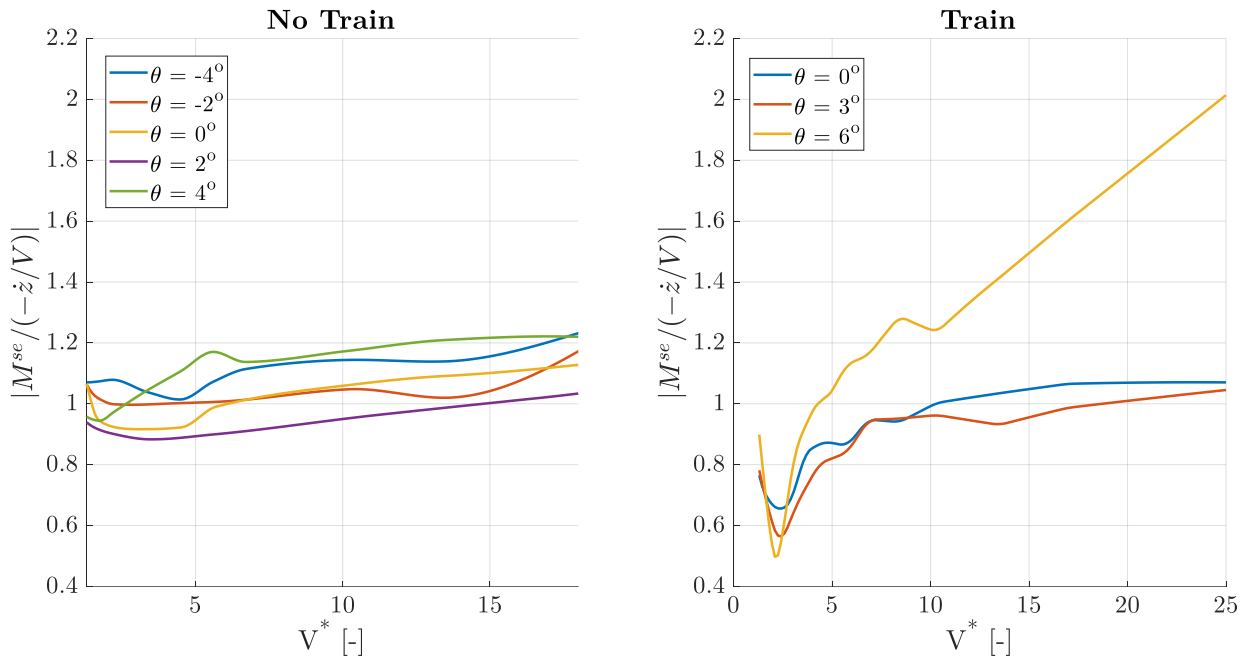

Figure 3.13. Modulus of M-z transfer function of the BB3 section with a train and without it.

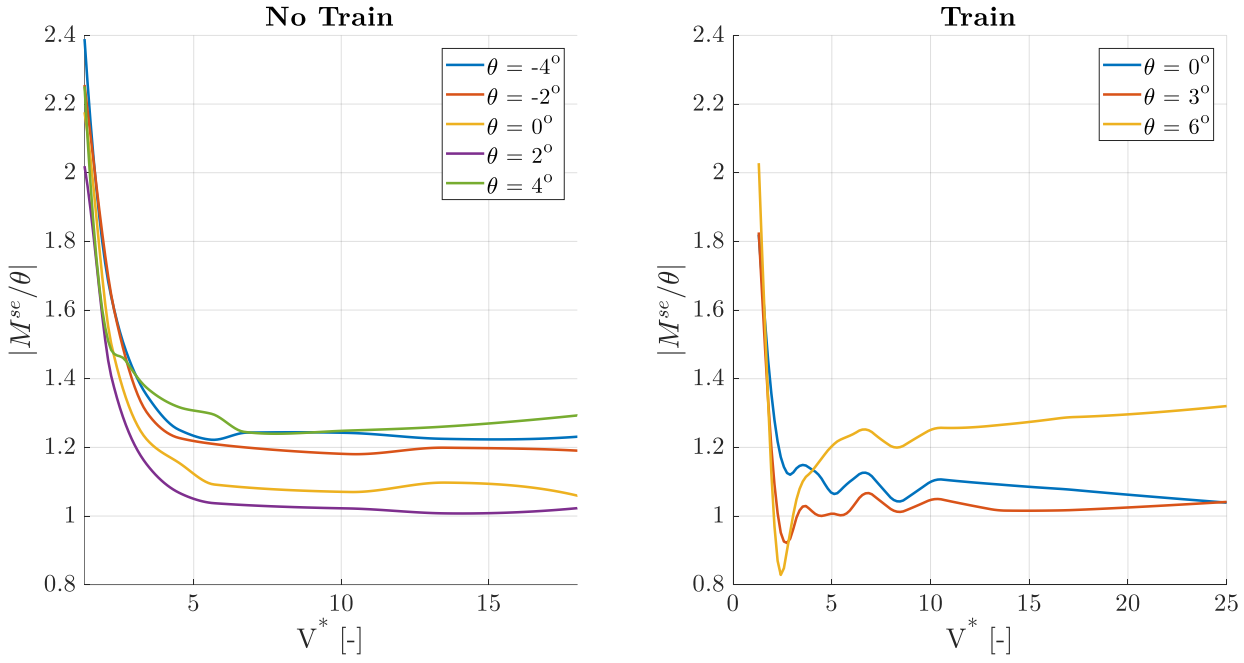

Figure 3.14. Modulus of M-θ transfer function of the BB3 section with a train and without it.

Figures Figure 3.11 through Figure 3.14 illustrate the greater dependence of the self-excited forces L^{se} and M^{se} in the mean angle of attack in the BB3 sectional model with a train with respect to the BB3 sectional model without the train.

Aerodynamic Admittance Functions

The modulus of the aerodynamic admittance functions for both sections are illustrated in figures Figure 3.15 and Figure 3.16. At high V^*, where the QST is valid, it is noticed a significant divergence of the $|\chi_{Lw}|$ and $|\chi_{Mw}|$ for a mean angle of attack of θ=6º. Thus, the buffeting forces will have a greater amplitude at large positive angles of attack for the BB3 section with a train than for the BB3 section without it.

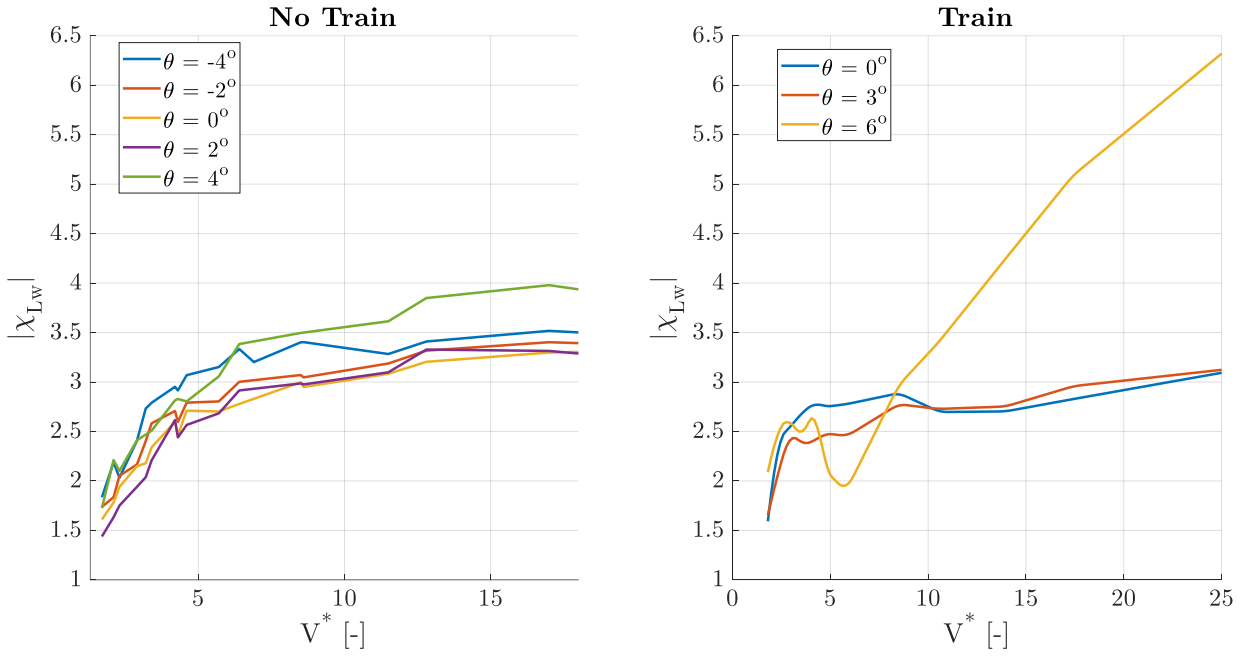

Figure 3.15. Amplitude of Lift admittance function for the BB3 section with a train and without it.

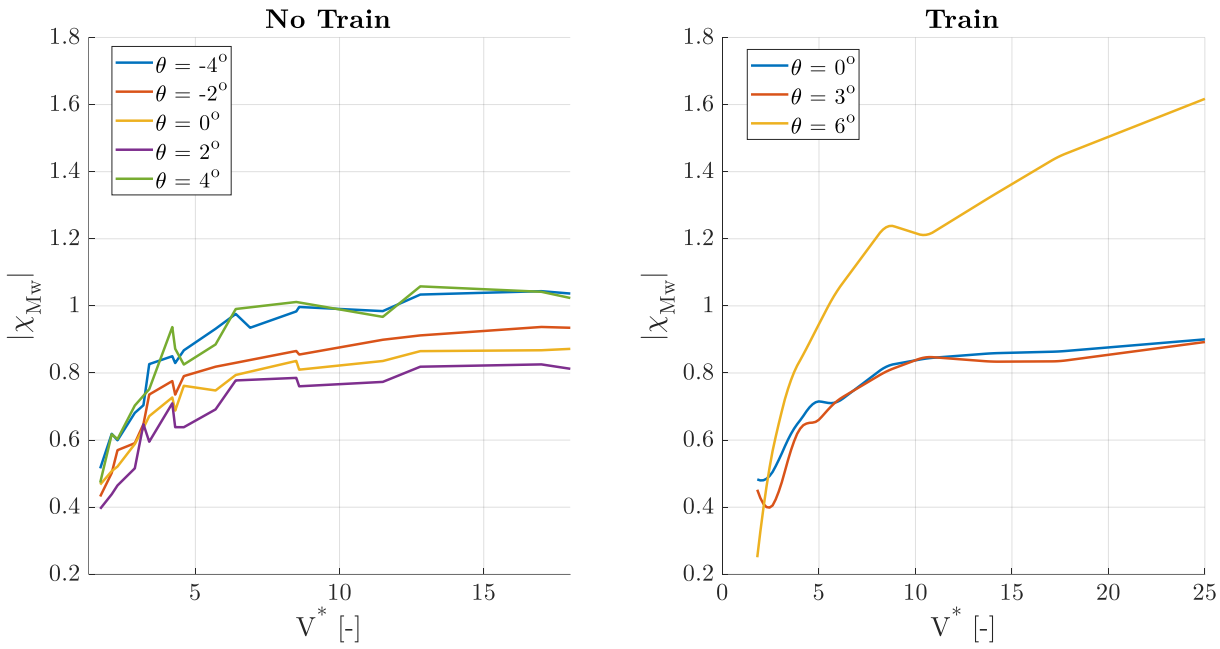

Figure 3.16. Amplitude of Moment admittance function for the BB3 section with a train and without it.

3.3 Forced Motion Tests

In the previous section, the aerodynamic coefficients that allow us to write the equation of motion of the problem (equation (1-46)) have been discussed. Given the major discrepancies in the aerodynamic coefficients between the BB3 section with a train and without it, it is consequently expected a different behavior for the two sections under an equivalent wind turbulence excitation.

The experimental setup for the forced motion tests of the BB3 section without a train resulted in different natural frequencies and damping ratios than those of *configuration 1* and *configuration 2* for the BB3 section with a train (Table 2.5). The springs configuration over the BB3NT provides the following (A. Pellegri 2017) modal parameters:

Modal Parameters

$m_{y,z}$ (kg/m)	17.42
I_θ (kg m)	2.59
f_z (Hz)	2.27
f_θ (Hz)	3.54
ξ_z (%)	0.17
ξ_θ (%)	0.20

Table 3.2. Modal parameters of the two configurations of the elastically suspended BB3NT.

The forced motion tests conducted over the elastically suspended BB3NT sectional model were intended to excite the z and θ degrees of freedom, both independently and simultaneously, along with a low frequency component able to dramatically affect the magnitude of the low frequency component of the angle of attack oscillations α_{LF}. The forced motion tests conducted over the BB3NT sectional model whose results will be compared to those obtained from the forced motion tests over the BB3T model are displayed in Table 3.3. Among the forced motion tests realized over the BB3T section, the following have been chosen from Table 2.6 and Table 2.7 given that they illustrate clearly the aerodynamic non-linearities present in the problem. Likewise, they also resemble the tests of BB3NT in that a low frequency component of the wind input is present concurrent with a high frequency component exciting either the z or θ degrees of freedom, or both at the same time.

No Train						Train					
Test	***V*** **[m/s]**	***f*** **[Hz]**	**A [cm]**	**phase [º]**	***V**** **[-]**	**Test**	***V*** **[m/s]**	***f*** **[Hz]**	**A [cm]**	**phase [º]**	***V**** **[-]**
NT-1	10	0.10	6	-	85.47	**1-1**	13.30	0.05	3	-	227.4
		3.40	2	0	2.51			2.20	1	-	5.17
NT-2	10	0.10	6	-	85.47	**1-2**	13.30	0.10	2.5	-	113.7
		2.20	1.5	0	3.89			2.20	1	0	5.17
NT-3	15	0.10	6	-	128.21	**1-3**	13.30	0.025	2.5	-	454.7
		3.30	1.5	0	3.89			2.20	1	0	5.17
NT-4	11.7	0.10	4	-	100.00	**2-1**	14.10	0.05	3.5	-	241.03
		2.65	1.5	0	3.77			1.75	0.3	0	6.89

Table 3.3. Forced motion tests conducted over BB3NT.

It is to be recalled that the forced motion tests for the BB3T sectional model were conducted around a mean rotation of θ_0=+3º. This was done in accordance to the fact that C_M=0 at θ_0=+3º, and this way, a static rotation is avoided. In consequence, the angles of attack α_{LF} depicted in figuresFigure 3.18 to Figure 3.28 are around 3º, and this value has to be added up to α_{LF} to obtain the "real" deck angle of attack.

On the following, a discussion is presented on the different responses obtained by the BB3NT and the BB3T. Firstly, the vertical incoming turbulence w of each test is displayed. Secondly, the α_{LF} times history is presented along with the unsteady motion of the sectional model, i.e. z_{HF} and θ_{HF}. Then, the α_{LF} times history is presented along with the high frequency components of the force coefficients $C_{L,HF}$ and $C_{M,HF}$. At last, a deep insight in the aerodynamic coefficients (static coefficients, flutter derivatives, admittance functions) is performed in order to explain the obtained response of the sectional model. Each test conducted over the BB3NT is compared to another test conducted over the BB3T.

NT-1 and 1-1

The NT-1 test conducted over the BB3NT excites the θ degree of freedom at high frequency. Meanwhile, the 1-1 test conducted over the BB3T excites a structural mode that couples the motion in z and θ, situation is discussed in section 2.4.3. The incoming turbulence and the deck's response for each test are depicted in the following.

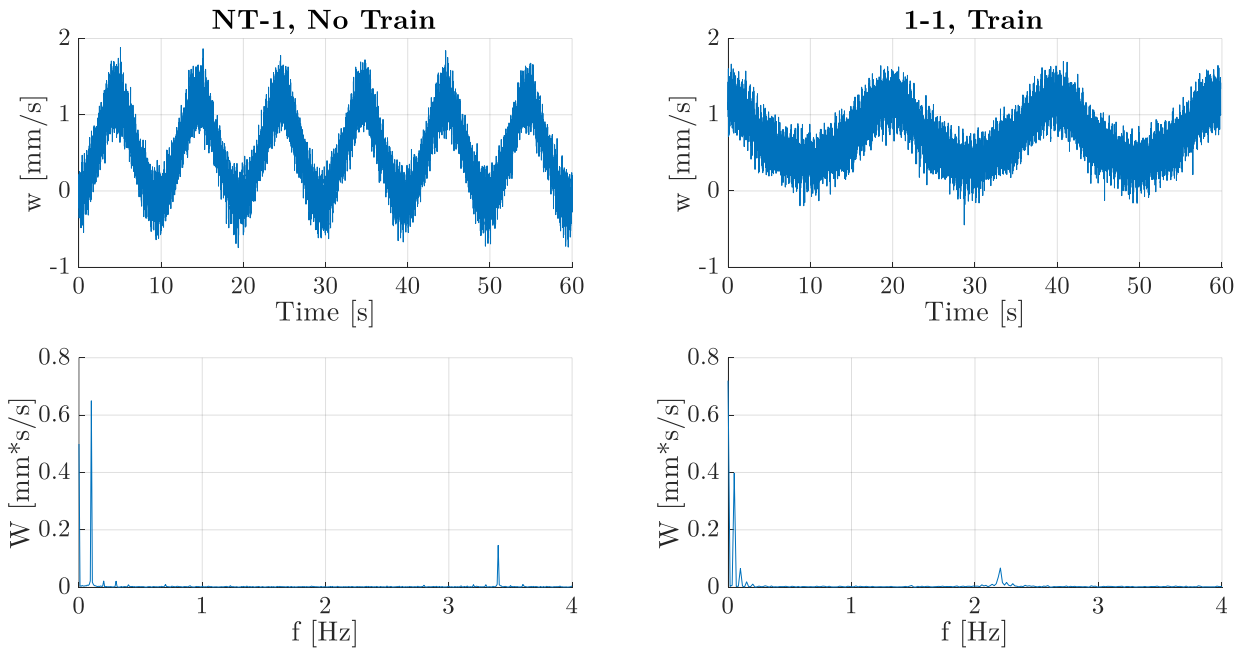

Figure 3.17. Incoming wind turbulence; tests NT-1 and 1-1.

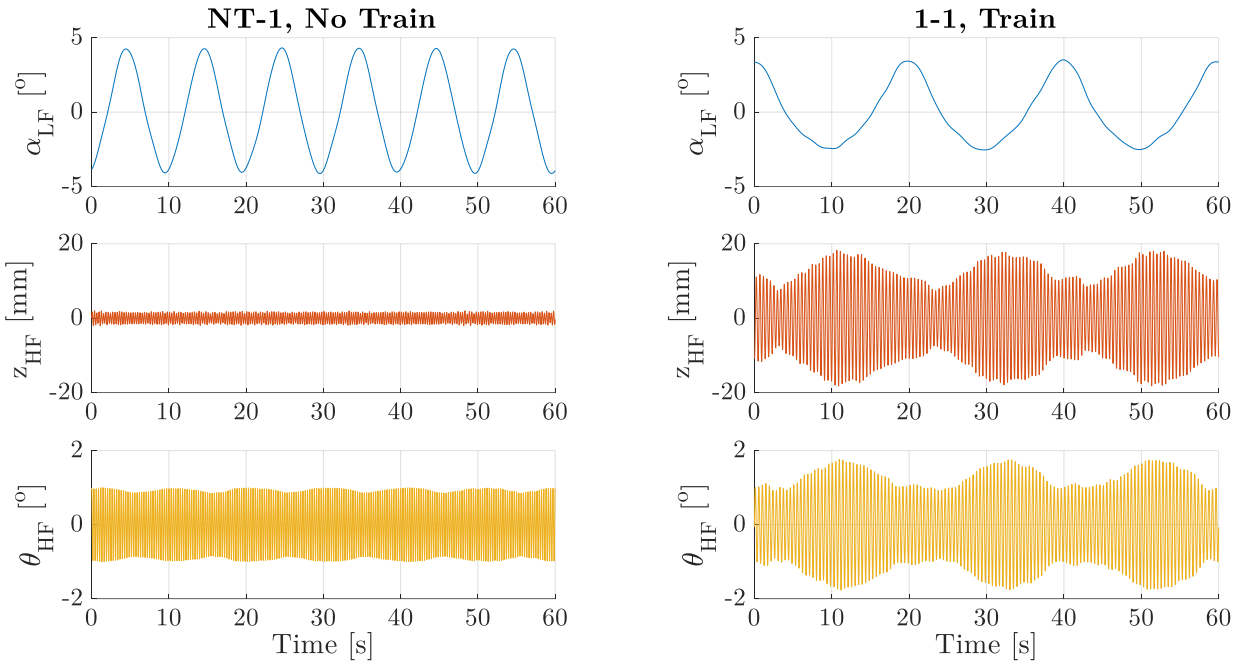

Figure 3.18. α_{LF}, z_{HF}, and θ_{HF}; tests NT-1 and 1-1.

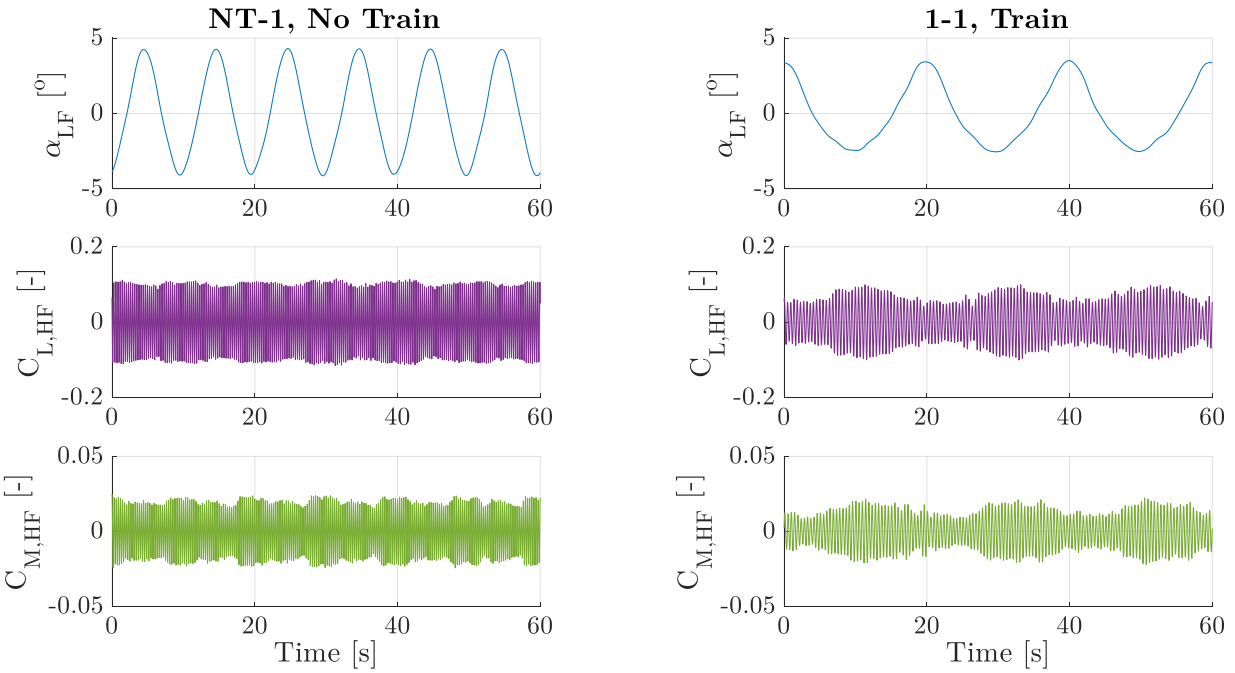

Figure 3.19. $C_{L,LF}$, and $C_{M,LF}$; tests NT-1 and 1-1.

We can observe a stronger dependence of the deck's unsteady motion (z_{HF} and θ_{HF}) on the low frequency fluctuations of the angle of attack α_{LF} in the BB3T than in BB3NT. As a matter of fact, at its lowest amplitude, θ_{HF} in the BB3T assumes a magnitude of 0.9°, and at its highest amplitude it assumes a magnitude of 1.8°, doubling itself. The same variation in θ_{HF} in the BB3NT is of less than 10%, thus being much less significant. A similar trend happens in z_{HF} in BB3T, whose largest magnitude is of 18 mm, more than the double that its lowest magnitude at 7 mm. This dependence of the unsteady motion on α_{LF} in the BB3T can be explained by the flutter derivatives a_2^* (Figure 3.4) and h_1^* (Figure 3.7) at V^*=5.17. We notice that a_2^* varies from 0.35 at α=0° to 0.7 at α=6° for the BB3T, while that a_2^* varies from 0.19 at α=-4° to 0.27 at α=+4° for the BB3NT at V^*=2.51. In the BB3T the maximum amplitudes of unsteady motion take place at the lowest value of α_{LF}, ≅0.5° (after summing up θ_0=3°); while the minimum amplitudes of unsteady motion take place at the lowest value of α_{LF}, ≅6.5° (after summing up θ_0=3°). This is in accordance to the fact that a_2^* is directly related to the damping of the θ motion, and it assumes high values at high angles of attack, and assumes low values at low angles of attack.

Regarding the trend of the aerodynamic force coefficients, it is noted that $C_{L,HF}$ and $C_{M,HF}$ in BB3T at its highest amplitude doubles its value at its lowest amplitude, while in BB3NT its variability is very low. Reference can be done to the admittance functions (Figure 3.15 and Figure 3.16). The non-linear dependence of $|\chi_{Mw}|$ and $|\chi_{Lw}|$ at low V^* on the angle of attack is more notorious in the BB3T than in BB3NT, where $|\chi_{Mw}|$ and $|\chi_{Lw}|$ assume more constant values.

NT-2 and 1-2

The NT-2 test conducted over the BB3NT excites the z degree of freedom at high frequency. Meanwhile, the 1-2 test conducted over the BB3T excites a structural mode that couples the motion in z and θ. The low frequency component of both tests has the same frequency at 0.10 Hz. The incoming turbulence and the deck's response for each test are depicted in the following.

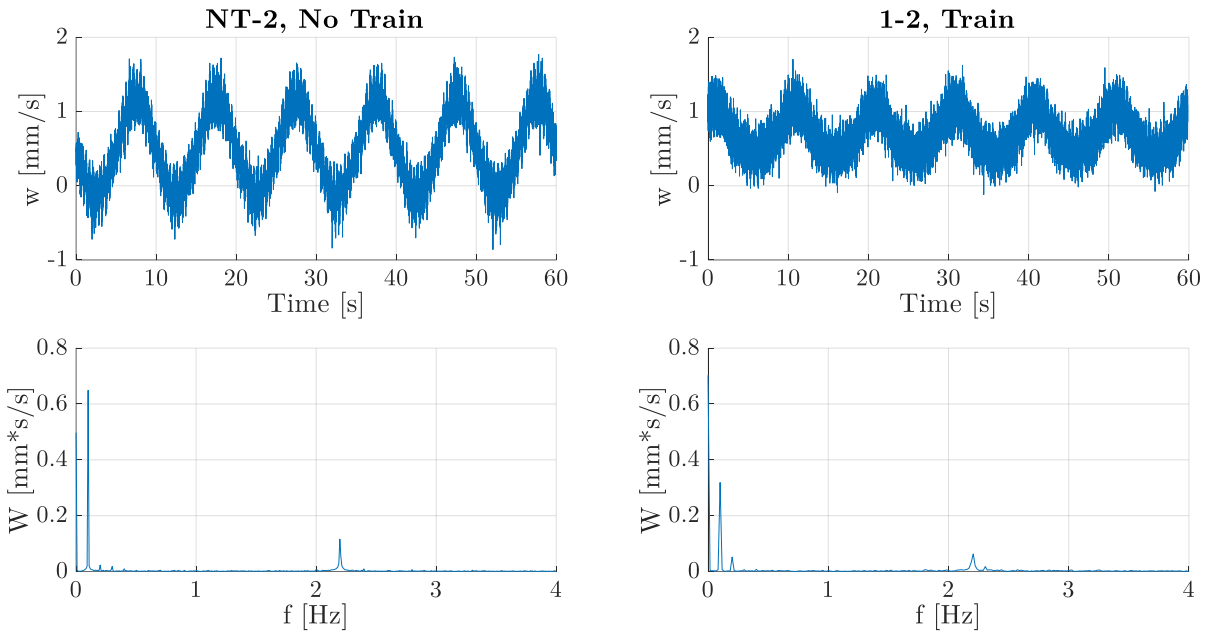

Figure 3.20. Incoming wind turbulence; tests NT-2 and 1-2.

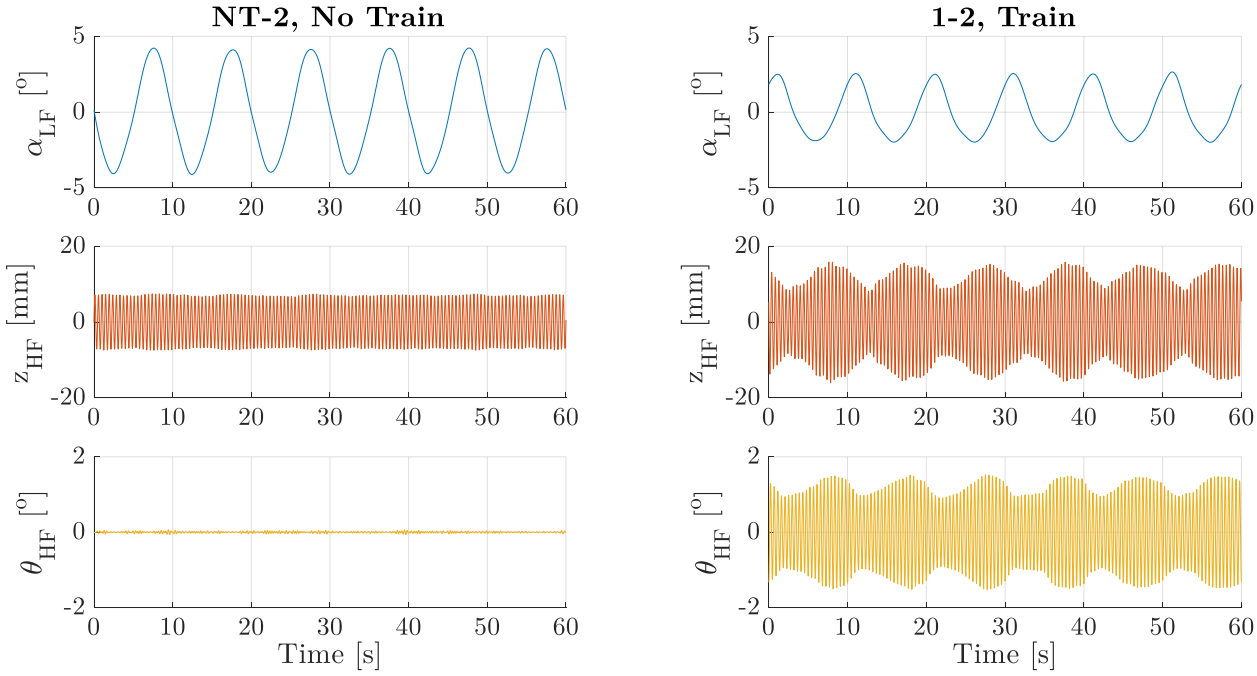

Figure 3.21. α_{LF}, z_{HF}, and θ_{HF}; tests NT-2 and 1-2.

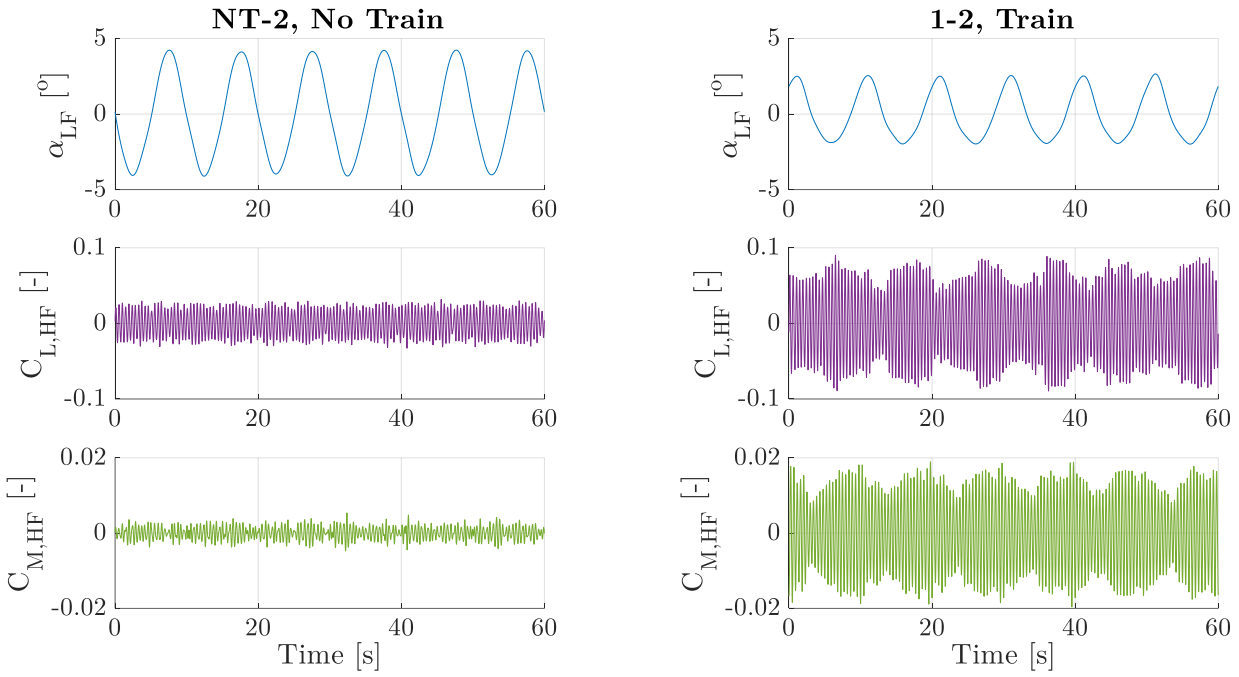

Figure 3.22. $C_{L,LF}$, and $C_{M,LF}$; tests NT-2 and 1-2.

Again, the dependence of the deck's unsteady motion (z_{HF} and θ_{HF}) on α_{LF} is significantly more notorious in BB3T than in BB3NT. As a matter of fact, z_{HF} can easily be reproduced with a sinusoidal function with constant amplitude. This is evident in h_1^* (Figure 3.7), directly related to the damping of the z degree of freedom, for BB3NT, where at V^*=3.89 its value varies from 3.4 at α=-4° to 3.3 at α=+4°, the range of oscillations of α_{LF} in NT-2. In contrast, h_1^* for BB3T at V^*=5.17 displays a highly non-linear dependence on α, varying from 2.0 at α=+6° to 2.8 at α=0°.

The same trend is visible in the aerodynamic force coefficients, which depict a strong relation with α_{LF} for BB3T and is rather constant for the BB3NT. The magnitude of $|\chi_{Lw}|$ (Figure 3.15) for BB3NT at V*=3.89 varies from 2.5 at α=-4° to 2.7 at α=+4°, while the magnitude of $|\chi_{Lw}|$ for BB3T at V*=5.17 varies from 2.1 at α=6° to 2.8 at α=0°, a greater variation.

NT-3 and 1-3

The NT-3 test conducted over the BB3NT as well as the 1-3 test conducted over the BB3T excites a structural mode that couples the motion in z and θ, mainly due to the high incoming mean wind speed. The low frequency component of the 1-13 test is 0.25 Hz, a frequency 4 times lower than the low frequency component of the NT-3 test. The incoming turbulence and the deck's response for each test are depicted in the following.

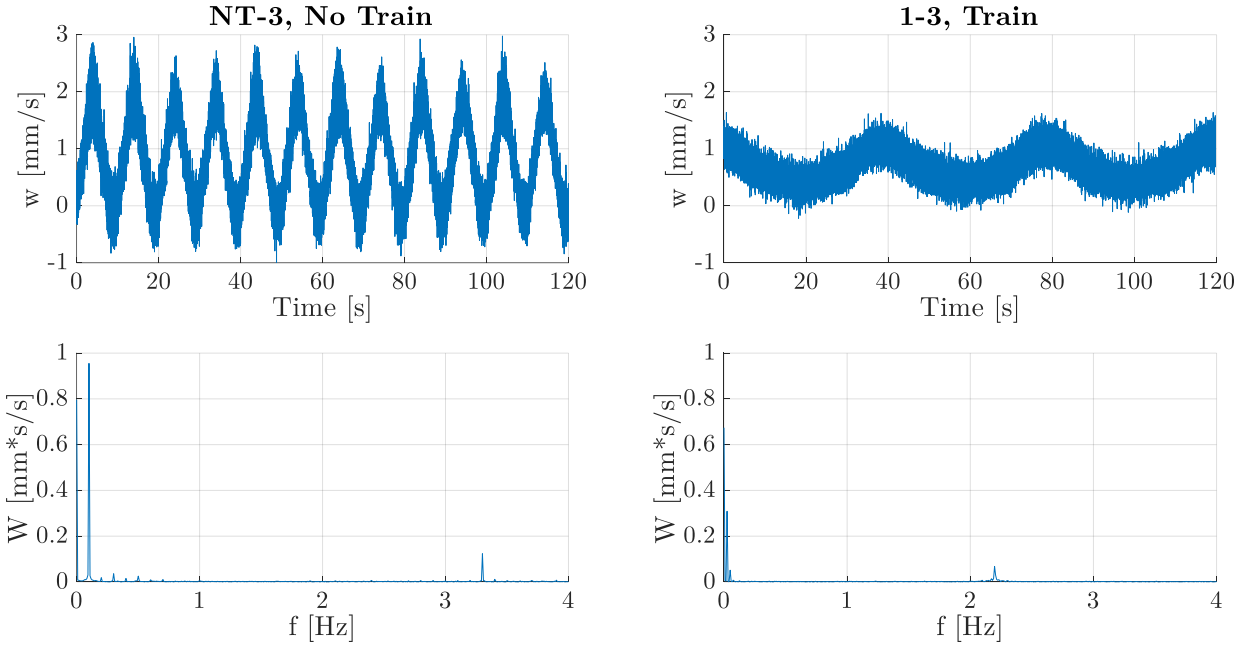

Figure 3.23. Incoming wind turbulence; tests NT-3 and 1-3.

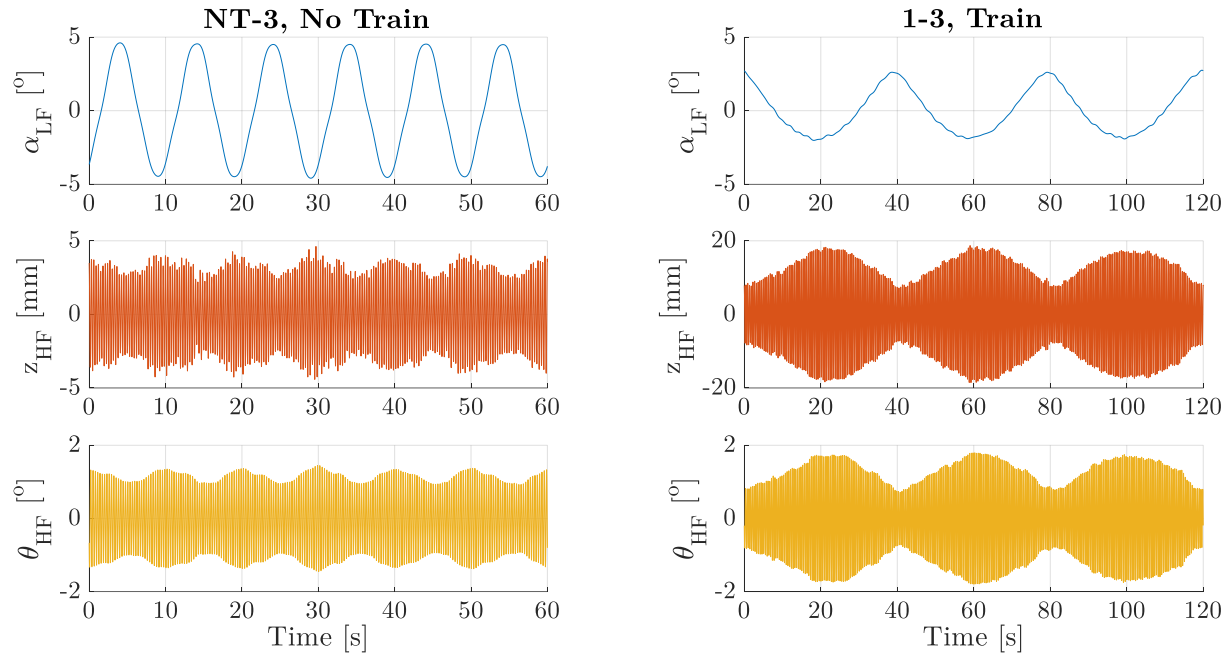

Figure 3.24. α_{LF}, z_{HF}, and θ_{HF}; tests NT-3 and 1-3.

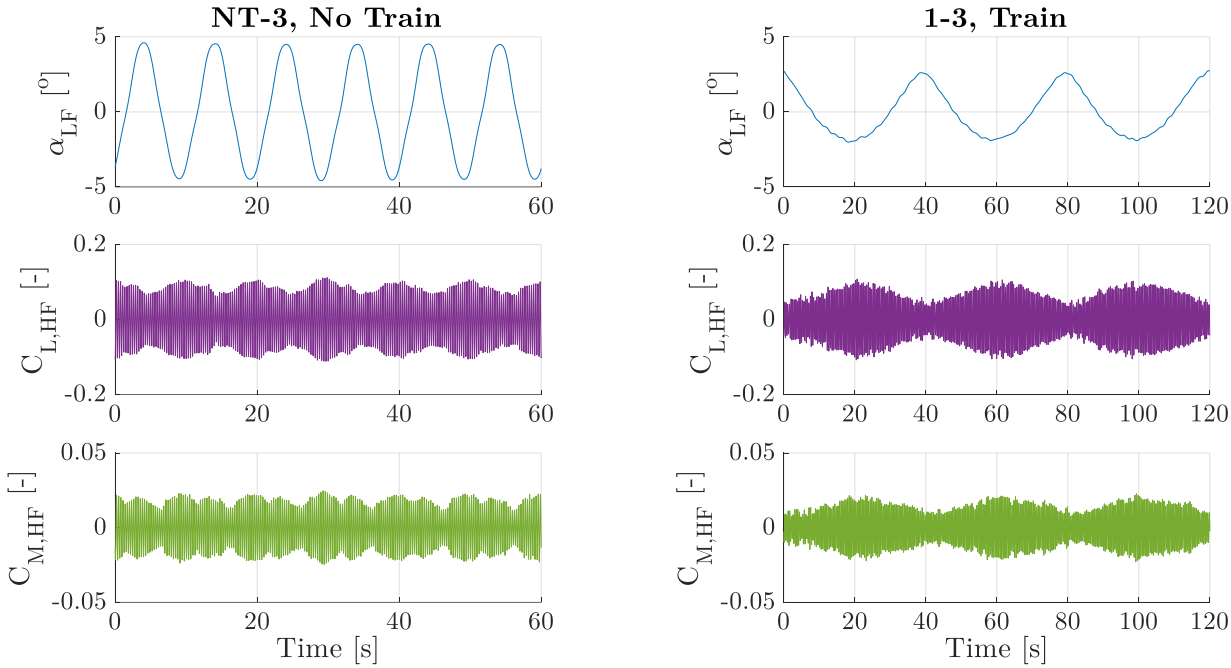

Figure 3.25. $C_{L,LF}$, and $C_{M,LF}$; tests NT-3 and 1-3.

At a very low frequency component of the wind input for the test 1-3, we have the possibility to examine more closely the dependence of the high frequency response components with the instantaneous α_{LF}. In this case, α_{LF} oscillates from 1° to 5.5° (after summing up θ_0=3°). It is very clear that at α_{LF}=5.5° (its maximum) all the response quantities - motion and force coefficients - are at its minimum, and vice versa: at α_{LF}=1° (its maximum) all the response quantities are at its maximum. The explanation is the same as the ones provided above: at V^*=5.17 h_1^* varies from 2.2 at α=6° to 2.7 at α=0°. This implies that after α_{LF} approaches its maximum value (5.5°), h_1^* is low (and consequently, the damping ratio is low as well) and the amplitude of z fluctuations start to increase. This happens until α_{LF} reaches its minimum (1°) where h_1^* is higher and the amplitude of z fluctuations start to decrease. This behavior is not so easily explained when analyzing a_2^*, given that at V^*=5.17 it varies from 0.35 at α=0° to 0.66 at α=6°. It is however recalled that at V_m=13.30 m/s the structural mode at *configuration 1* for BB3T coupled the motions from z and θ.

On the other hand, test NT-3 depicts for the first time a significant dependence from the unsteady response components on α_{LF}. Although V^*=3.89 as in test NT-2, this is achieved at a higher mean wind speed (15 m/s) in which the structural damping is generally low, hence allowing a greater dependence on the aeroelastic damping. Thus, θ goes from 0.9° at its minimum to 1.4° at its maximum. For BB3NT, a_2^* that at V^*=3.89 it varies from 0.22 at α=-4° to 0.32 at α=4°.

NT-4 and 2-1

The NT-4 test conducted over the BB3NT as well as the 2-1 test conducted over the BB3T excites a structural mode that couples the motion in z and θ, mainly due to the high incoming mean wind speed. The low frequency component of the 2-1 test is 0.5 Hz, a frequency 2 times lower than the low frequency component of the NT-4 test. Test 2-1 is conducted at 14.10 m/s which is very close to the flutter velocity of *configuration 2* of the BB3T, which is 14.65 m/s. The incoming turbulence and the deck's response for each test are depicted in the following.

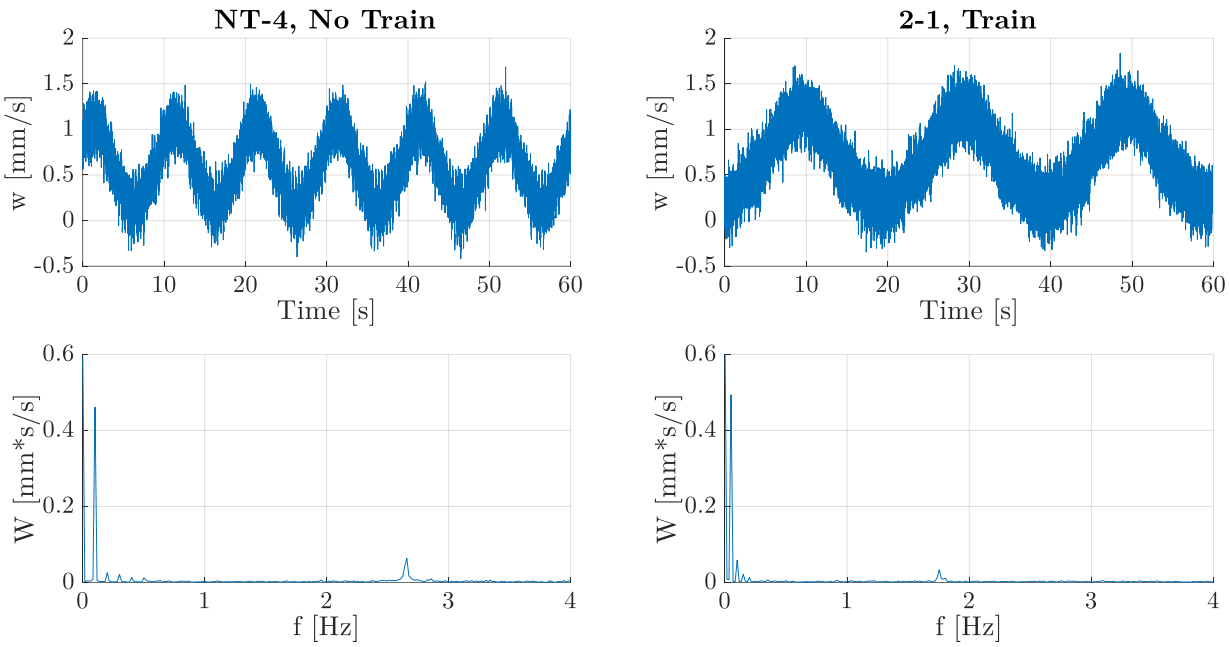

Figure 3.26. Incoming wind turbulence; tests NT-4 and 2-1.

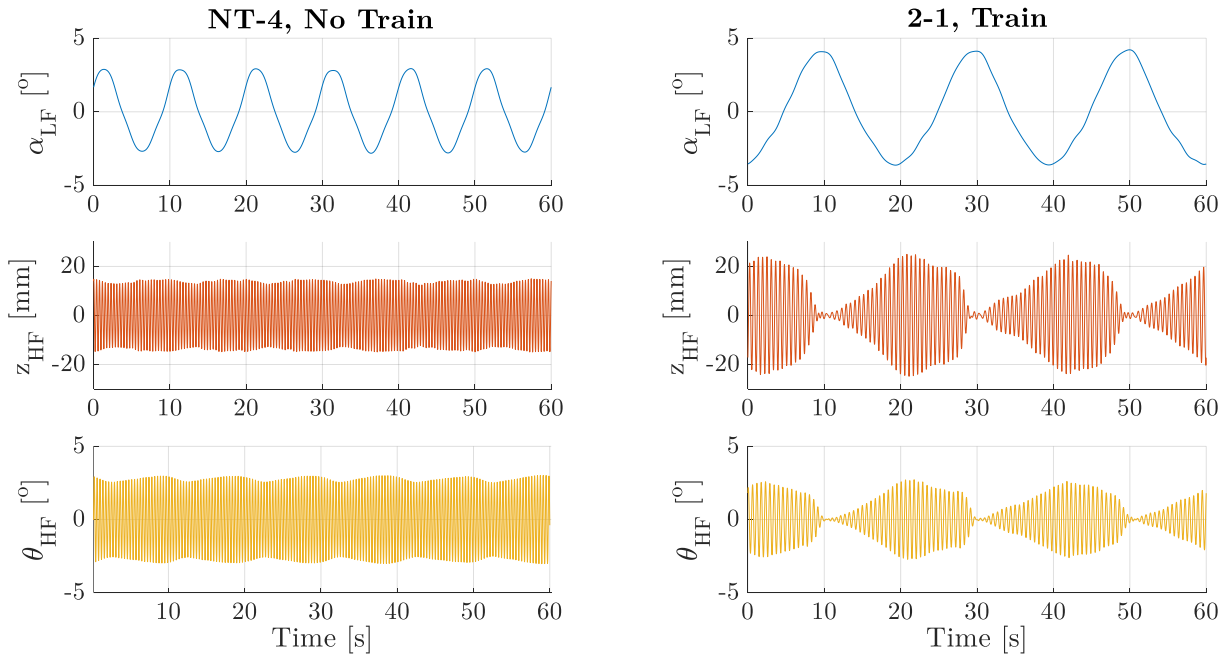

Figure 3.27. α_{LF}, z_{HF}, and θ_{HF}; tests NT-4 and 2-1.

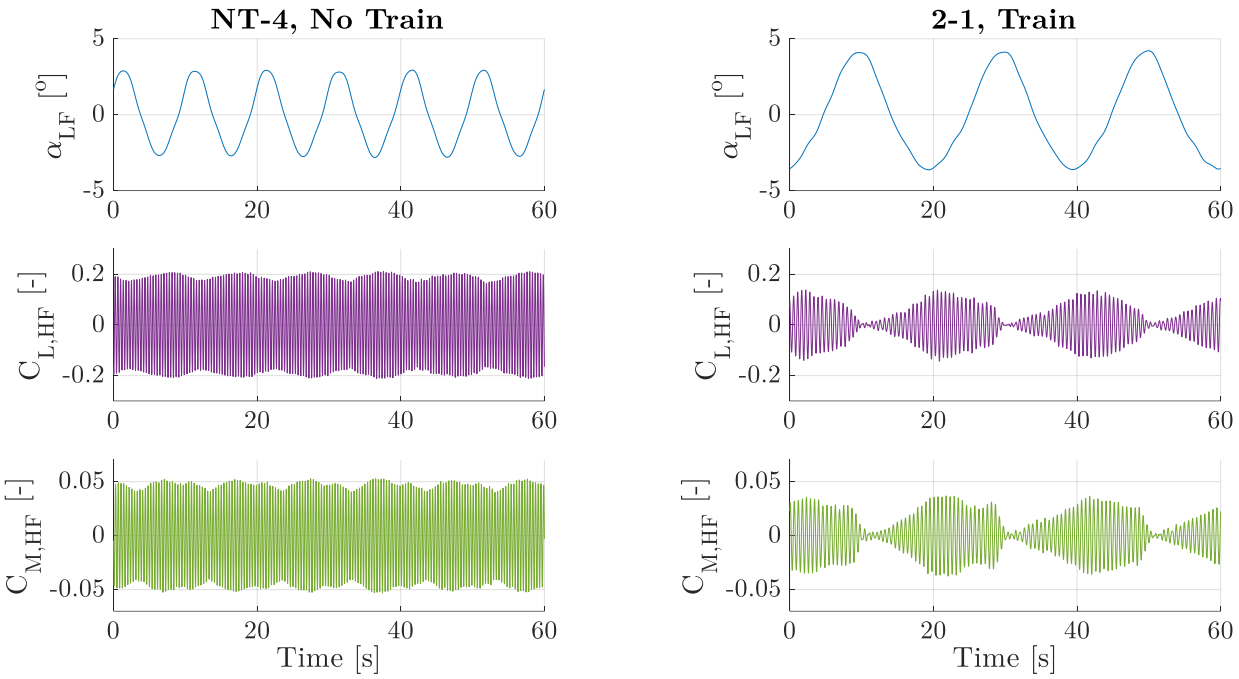

Figure 3.28. $C_{L,LF}$, and $C_{M,LF}$; tests NT-4 and 2-1.

Test 2-1 is particularly interesting in that it is close to flutter instability where the structural damping is zero. Thus, the amplitudes of the motion depend entirely on α_{LF}, which fluctuates from -0.5° to +7° (after summing up θ_0=3°). At α_{LF}=+7°, the amplitudes of the oscillations rapidly decrease to almost zero, followed up by a dramatic increase up to when α_{LF}=-0.5°. Again, the flutter derivatives a_2^* and h_1^* of the BB3T might give us some insights. At V^*=6.89 h_1^* and a_2^* have a strong non-linear dependence on α.

The BB3NT is also excited close to flutter instability. It is noticed that for the first time, both motion components z and θ are excited simultaneously. However, although the structural damping at this high speed (V_m=11.10 m/s for configuration 2 of BB3NT) is considerably low, the dependence on α_{LF} is not as significant as in the BB3T sectional model, and the amplitudes of vibration do not vary as much.

3.4 New non-linear rheological model

Having now presented the non-negligible non-linear relationship between the aerodynamic forces and the angle of attack, a new method, as an extension to the band-superposition approach (section 1.3), is proposed in order to account for the evident non-linearities.

The new method here proposed is based on a non-linear QSTC, which well describes the non-linearities at high V^* and in order to well reproduce the behavior of the bridge also at low reduced velocities where the QSTC is not valid, a rheologic approach is used in time-domain to describe both the motion-dependent (or self-excited) as well as the turbulence dependent (or buffeting) aerodynamic forces. The aerodynamic matrices $[K_a]$ and $[R_a]$, and $[A_m]$ identified through dynamic wind tunnel tests with free motion or forced motion methods are dependent on the reduced velocity V^* (see section 2.4). These are the aeroelastic matrices that contain the flutter derivatives and the aerodynamic admittance functions. The linearization of the aerodynamic forces of the QSTC around the angle of attack α_0 gives rise to the matrices $[K_{aQ}]$, $[R_{aQ}]$, and $[A_{mQ}]$ that are constant, independent from the reduced velocity V^* but dependent only on the static angle of attack α_0. New aerodynamic matrices are defined as the difference between the matrices $[K_a]$ and $[R_a]$, and $[A_m]$ and the constant QSTC matrices $[K_{aQ}]$, $[R_{aQ}]$, and $[A_{mQ}]$. Consequently, the new difference matrices dependent on the reduced velocity: $[K_{aD}]$, $[R_{aD}]$, and $[A_{mD}]$, converge to zero at high reduced velocities. Rheological models are used to transform from the frequency-domain to the time-domain the $[K_{aD}]$, $[R_{aD}]$, and $[A_{mD}]$ matrices, which are dependent on the reduced velocity and on the angle of attack around which they are defined. The rheologic approach adds new degrees of freedom reproducing the fluid-structure interaction. The angle of attack α_0 around which the flutter derivatives and the admittance matrix coefficients are identified, is reproduced by the different parameters of the rheological models themselves, that become a function of the angle of attack α_0 only.

The modification of the new approach with respect to the BS approach are:

- No separation of the wind bands

- No superposition between LF and HF responses
- No separated integrations

In replacement to the above features of the BS approach, the new model proposes a “one-shot” integration which gathers all the response contributions at once made of:

- Static deflection
- LF response
- HF response

Chapter 4

Non-linear analytical approach

4.1 Introduction

The method as described in section **Error! Reference source not found.** employs the non-linear QSTC and the rheological model approach in order to compute the complete response of the bridge deck in time-domain, through a one-shot integration, taking into account the non-linear effect of the aerodynamic forces mainly related to the variation of the angle of attack of the wind and of the deck rotation (S. O. G. Diana n.d.). The method is therefore able to describe the static equilibrium position, the low-frequency response, and the high-frequency response of the bridge simultaneously.

In the present chapter, the analytical formulation of the new proposed approach is presented. Special attention is paid in the formulation of the rheological models which allow us to describe the aerodynamic transfer functions i.e. the flutter derivatives and admittance functions, in the time-domain.

4.2 Non-linear formulation

The main aspects related to the definition of the non-linear aerodynamic forces have already been introduced in the description of the QSTC in section 1.2.1. It is recalled that the QST assumes that the non-linear aerodynamic forces, acting on the section of the bridge deck, dependent on the motion and on the incoming turbulence are defined by the static aerodynamic coefficients that are measured in the wind tunnel on a rigid sectional deck model as a function of the angle of attack α. The linearization procedure of the non-linear aerodynamic forces allows them to be

written as expressed in equations (1-40) through (1-45). For practical purposes, the aerodynamic forces expressed through the QSTC are here rewritten, in which the aerodynamic matrices have been renamed with the additional subsubscript 'Q' to denote that these are the matrices coming from the QSTC:

$$\begin{aligned}\underline{F}_{aero,Q} = \underline{F}_{aero,Q_0} &+ \frac{1}{2}\rho BLV^2 \begin{bmatrix} 0 & 0 & K_{D_0} \\ 0 & 0 & K_{L_0} \\ 0 & 0 & BK_{M_0} \end{bmatrix} \begin{bmatrix} \bar{y} \\ \bar{z} \\ \bar{\theta} \end{bmatrix} \\ &- \frac{1}{2}\rho BLV \begin{bmatrix} 2C_{D_0} & (K_{D_0} - C_{L_0}) & (K_{D_0} - C_{L_0})B_{1y} \\ 2C_{L_0} & (K_{L_0} + C_{D_0}) & (K_{L_0} + C_{D_0})B_{1z} \\ 2BC_{M_0} & BK_{M_0} & BK_{M_0}B_{1\theta} \end{bmatrix} \begin{bmatrix} \dot{y} \\ \dot{z} \\ \dot{\theta} \end{bmatrix} \\ &+ \frac{1}{2}\rho BLV^2 \begin{bmatrix} 2C_{D_0} & K_{D_0} - C_{L_0} \\ 2C_{L_0} & K_{L_0} + C_{D_0} \\ 2C_{M_0} & BK_{M_0} \end{bmatrix} \begin{bmatrix} \frac{u}{V} \\ \frac{w}{V} \end{bmatrix} \\ &= \underline{F}_{aero,Q_0} + \left[K_{aero_Q}\right]\underline{\bar{x}} + \left[R_{aero_Q}\right]\underline{\dot{x}} + [A_{m_Q}]\underline{b}\end{aligned} \tag{4-1}$$

The $\left[K_{aero_Q}\right]$ and $\left[R_{aero_Q}\right]$ matrices multiplied by $\underline{\bar{x}}$ and $\underline{\dot{x}}$ define the linearized aerodynamic forces function of the motion, while the $[A_{m_Q}]$ matrix multiplied by $\underline{b}$ defines the linearized aerodynamic forces function of the incoming turbulence. This formulation holds true for high reduced velocities V^*. All the parameters needed to define the $\left[K_{aero_Q}\right]$, $\left[R_{aero_Q}\right]$ and $\left[A_{m_Q}\right]$ matrices must be identified through static wind tunnel tests, and are independent from V^*.

To consider the reduced velocity dependence, the matrices $[K_{aero}]$, $[R_{aero}]$ and $[A_m]$ were introduced in section 1.2.3. The parameters contained in these matrices are identified through dynamic wind tunnel tests. A harmonic motion is imposed on the deck section in the y, z and θ directions measuring the flutter derivatives coefficients of $[K_{aero}]$ and $[R_{aero}]$ for different V^* and θ_0. The aerodynamic admittance functions for $[A_m]$ are measured by employing an active turbulence generator and modifying the incoming flow for different V^* and θ_0 (see section 2.4.2). The $[K_{aero}]$, $[R_{aero}]$ and $[A_m]$ matrices are expressed in the previous chapter in equations (1-50), (1-51) and (1-52), rewritten in the following for practical purposes:

$$[K_{aero}] = -\frac{1}{2}\rho BLV^2 \begin{bmatrix} p_6^* \frac{\pi}{2V_\omega^{*2}} \frac{1}{B} & p_4^* \frac{\pi}{2V_\omega^{*2}} \frac{1}{B} & p_3^* \\ h_6^* \frac{\pi}{2V_\omega^{*2}} \frac{1}{B} & h_4^* \frac{\pi}{2V_\omega^{*2}} \frac{1}{B} & h_3^* \\ a_6^* \frac{\pi}{2V_\omega^{*2}} & a_4^* \frac{\pi}{2V_\omega^{*2}} & a_3^* \end{bmatrix} \tag{4-2}$$

$$[R_{aero}] = \frac{1}{2}\rho BLV \begin{bmatrix} p_5^* & p_1^* & p_2^* \\ h_5^* & h_1^* & h_2^* \\ a_5^* B & a_1^* B & a_2^* B \end{bmatrix} \tag{4-3}$$

$$[A_m] = \frac{1}{2}\rho BLV^2 \begin{bmatrix} \chi_{yu}^* & \chi_{yw}^* \\ \chi_{zu}^* & \chi_{zw}^* \\ B\chi_{\theta u}^* & B\chi_{\theta w}^* \end{bmatrix} \tag{4-4}$$

In the approach here presented, however, the aerodynamic coefficients cannot be used as they are measured since a non-linear QSTC approach is already implemented is already implemented to compute the static and dynamic response of the bridge deck. Since it is valid for the high reduced velocity (equivalent to low frequency), is therefore already well described by the non-linear QSTC model, only a correction for low V^* (equivalent to high frequency) is necessary. New aerodynamic matrices called difference (subscript D) are defined as the difference between the experimental coefficients measured in the wind tunnel, reported in equations (4-2), (4-3) and (4-4) and the QSTC values, reported in equation (4-1), for each angle of attack θ_0. Therefore, in the new approach here presented, the aerodynamic coefficients at low reduced velocity are described through the difference between the $[K_{aero}]$, $[R_{aero}]$, $[A_m]$ and $\left[K_{aero_Q}\right]$, $\left[R_{aero_Q}\right]$,$\left[A_{m_Q}\right]$ matrices, respectively as:

$$\begin{gathered} \left[K_{aero_D}\right] = [K_{aero}] - \left[K_{aero_Q}\right] \\ \left[R_{aero_D}\right] = [R_{aero}] - \left[R_{aero_Q}\right] \\ \left[A_{m_D}\right] = [A_m] - \left[A_{m_Q}\right] \end{gathered} \tag{4-5}$$

The new difference matrices: $\left[K_{aero_D}\right]$, $\left[R_{aero_D}\right]$, and similarly the admittance $\left[A_{m_D}\right]$ converge to zero at high reduced velocities. In this case, the new aerodynamic matrices are considered as a correction of the non-linear QSTC.

These matrices are dependent on V^* and on the angle of attack θ_0 around which the flutter derivatives and the admittance coefficients are measured in the wind tunnel. These matrices multiplied by the displacement vector $\underline{\bar{x}}$, the velocity $\underline{\dot{x}}$ and the incoming turbulence vector $\underline{b}$ give the $\underline{F_{aero_D}}$ aerodynamic forces, the correction of the forces calculated by the QSTC theory. The aerodynamic forces $\underline{F_{aero_D}}$ are defined as:

$$\underline{F_{aero_D}} = \underline{F_{aero_D}}(V_m, \underline{\bar{x}}, \underline{\dot{x}}, \underline{b}) = \left[K_{aero_D}\right]\underline{\bar{x}} + \left[R_{aero_D}\right]\underline{\dot{x}} + \left[A_{m_D}\right]\underline{b} \tag{4-6}$$

These forces add a contribution in order to consider the wrong description of the response at low reduced velocity of the QSTC. So, the overall aerodynamic forces $\underline{F_{aero}}$ considered in the new approach are written as the sum of the non-linear aerodynamic forces of the QSTC defined in equation (4-1) and the $\underline{F_{aero_D}}$ aerodynamic forces.

$$\underline{F_{aero}} = \underline{F_{aero_Q}}\left(V_m, \underline{\bar{x}}, \underline{\dot{x}}, \underline{b}\right) + \left[K_{aero_D}\right]\underline{\bar{x}} + \left[R_{aero_D}\right]\underline{\dot{x}} + \left[A_{m_D}\right]\underline{b} \tag{4-7}$$

Since the matrices $\left[K_{aero_D}\right]$, $\left[R_{aero_D}\right]$, and $\left[A_{m_D}\right]$ are dependent on the reduced velocity, this means they are defined in the frequency-domain, it is necessary to carry out a change of domain to deal with the equations in the time-domain. Rheological models are used at each angle of attack θ_0 and for each section of the bridge to change from frequency to time-domain. The aerodynamic forces $\underline{F_{aero_D}}$ are defined in the frequency-domain as:

$$\underline{F_{aero_D}}(\Omega) = \left(\left[K_{aero_D}(\Omega)\right] + i\Omega\left[R_{aero_D}(\Omega)\right]\right)\underline{X_0}e^{i\Omega t} + \left[A_{m_D}(\Omega)\right]\underline{B_0}e^{i\Omega t} \tag{4-8}$$

Each term of the matrix $\underline{F_{aero_D}}(\Omega)$ is a transfer function between the output force delivered to the bridge section and the input that could be either the displacement of the section $\underline{\bar{x}}$ or the turbulent component $\underline{b}$.

It is therefore possible to define nine transfer functions for the motion-induced forces and six transfer functions for the turbulence-induced forces. Simple mechanical models (masses, springs

and dampers) are used in order to have a rheological model (RM) that produces the frequency response function described by the aerodynamic transfer function under discussion. By introducing the mechanical models and connecting them to the bridge deck, the degrees of freedom of rheological models are introduced into the overall system. Thus, the initial structural matrices of the whole bridge are expanded: they now contain the degrees of freedom of the bridge ad the degrees of freedom of the RM for each section of the bridge deck. The dynamic contribution in time-domain introduced by the additional degrees of freedom describes the fluid interaction with the deck motions: the motion-dependent and the turbulence-dependent aerodynamic forces.

4.3 Rheological model approach

The use of the RM is aimed at reproducing the aerodynamic transfer functions $\underline{F_{aero}}_D(\Omega)$ in terms of module and phase or real and imaginary (equation (4-8)). Once identified the aerodynamic transfer functions, known in the frequency-domain through wind tunnel tests at fixed mean angles of attack, the aerodynamic forces are modelled in the time-domain with the RM parameters. Once the RM parameters are identified, it is possible to switch from the frequency-domain to the time-domain, as explained in the following.

This objective is pursued by modelling each component of force using different mechanical oscillators of the order 0, 1 and 2 placed in parallel, as depicted in Figure 4.1. Motion-dependent and turbulent-dependent aerodynamic forces are modelled independently, and their effects are summed up. The identification procedure consists in identifying the number and the order of the systems for each aerodynamic transfer function and the optimal value of the RM parameters for each angle of attack θ_0.

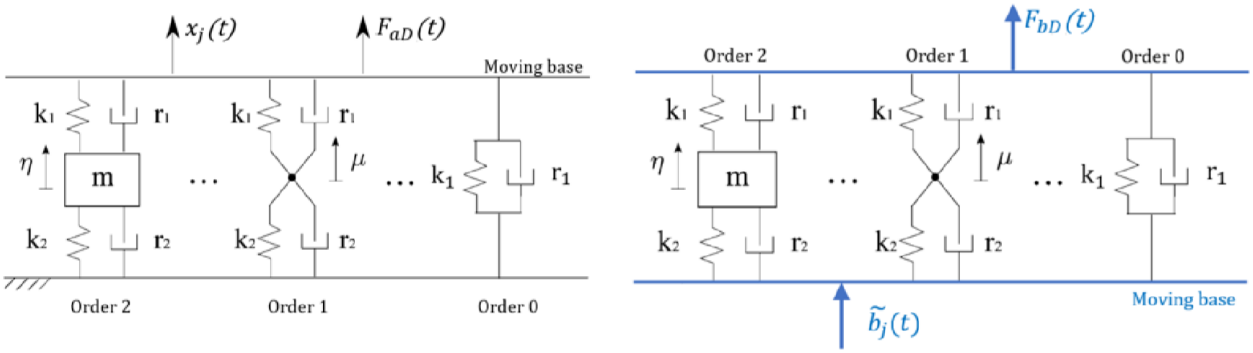

Figure 4.1. Rheological models: motion induced forces left side; turbulence induced forces right side.

Rheological model order 0

Is a simple spring-damper system whose equation is:

$$F^0_{aero_D} = k_1 x_j + r_1 \dot{x}_j \tag{4-9}$$

Where $F^0_{aero_D}$ is the generic force delivered to the section of the bridge, x_j the generic component of motion and k_l and r_l are the stiffness and damping values of the system. No additional degrees of freedom are introduced in the system with the RM order 0. The transfer function is:

$$\frac{F^0_{aero_D}}{x_j} = k_1 + i\Omega r_1 \tag{4-10}$$

Where Ω is the frequency.

Rheological model order 1

Is characterized by two zero order systems placed in series; it adds a degree of freedom to the problem. The equations of the system are:

$$F^1_{aero_D} = k_1 x_j + r_1 \dot{x}_j - k_1 \mu - r_1 \dot{\mu} \tag{4-11}$$

$$(k_1 + k_2)\mu + (r_1 + r_2)\dot{\mu} = k_1 x_j + r_1 \dot{x}_j \tag{4-12}$$

Where the coordinate μ represents the additional degree of freedom introduced by each system of order 1. The transfer function between the force delivered to the bridge and the bridge's motion is defined as follows:

$$\frac{F^1_{aero_D}}{x_j} = \frac{(k_2 + i\Omega r_2)(k_2 + i\Omega r_1)}{(k_1 + k_2) + i\Omega(r_1 + r_2)} \tag{4-13}$$

Rheological model order 2

A mass is added in middle of two systems of order 1 placed in series to insert the dependence of the second derivative of the input. Also, in this case an additional degree of freedom η is added to the problem. The equations of the system are:

$$F^2_{aero_D} = k_1 x_j + r_1 \dot{x}_j - k_1 \eta - r_1 \dot{\eta} \tag{4-14}$$

$$m\ddot{\eta} + (r_1 + r_2)\dot{\eta} + (k_1 + k_2)\eta = k_1 x_j + r_1 \dot{x}_j \tag{4-15}$$

The transfer function is defined as:

$$\frac{F^2_{aero_D}}{x_j} = \frac{(k_1 + i\Omega r_1)(-m\Omega^2 + i\Omega r_2 + k_2)}{-m\Omega^2 + i\Omega(r_1 + r_2) + (k_1 + k_2)} \tag{4-16}$$

The aerodynamic forces transfer function $\underline{F_{aero_D}}(\Omega)$ in equation (4-8) can be subdivided into self-excited and buffeting forces:

$$\underline{F^{se}_{aero_D}}(\Omega) = \left(\left[K_{aero_D}(\Omega)\right] + i\Omega\left[R_{aero_D}(\Omega)\right]\right)\underline{X_0} e^{i\Omega t} \tag{4-17}$$

$$\underline{F^{buff}_{aero_D}}(\Omega) = [A_{m_D}(\Omega)]\underline{B_0} e^{i\Omega t} \tag{4-18}$$

In conclusion, to model the motion induced forces, the RM systems here defined are appropriately calibrated and combined to obtain the nine aerodynamic transfer functions $\underline{F^{se}_{aero_D}}(\Omega)$ that link the degrees of freedom $\langle y\ z\ \theta \rangle$ of the section of the bridge with the motion-dependent aerodynamic forces, while to model the buffeting forces, the RM systems are calibrated and combined to obtain the six transfer functions $\underline{F^{buff}_{aero_D}}(\Omega)$ that link the incoming turbulence $\langle \frac{u}{V}\ \frac{w}{V} \rangle$ with the buffeting forces.

The nine aerodynamic transfer functions, written as employed in the numerical code, corresponding to the self-excited forces which the transfer functions of the rheological models are aimed to reproduce, are defined as:

$$\frac{D^{se}}{-\frac{\dot{y}}{V}} = \frac{1}{2}\rho V^2 B\left(p_5^* + i\frac{\pi^2}{V^*}p_6^*\right) \tag{4-19}$$

$$\frac{D^{se}}{-\frac{\dot{z}}{V}} = \frac{1}{2}\rho V^2 B\left(p_1^* + i\frac{\pi^2}{V^*}p_4^*\right) \tag{4-20}$$

$$\frac{D^{se}}{\theta} = \frac{1}{2}\rho V^2 B\left(p_3^* - i\frac{2\pi}{V^*}p_2^*\right) \tag{4-21}$$

$$\frac{L^{se}}{-\frac{\dot{y}}{V}} = \frac{1}{2}\rho V^2 B\left(h_5^* + i\frac{\pi^2}{V^*}h_6^*\right) \tag{4-22}$$

$$\frac{L^{se}}{-\frac{\dot{z}}{V}} = \frac{1}{2}\rho V^2 B\left(h_1^* + i\frac{\pi^2}{V^*}h_4^*\right) \tag{4-23}$$

$$\frac{L^{se}}{\theta} = \frac{1}{2}\rho V^2 B\left(h_3^* - i\frac{2\pi}{V^*}h_2^*\right) \tag{4-24}$$

$$\frac{M^{se}}{-\frac{\dot{y}}{V}} = \frac{1}{2}\rho V^2 B^2\left(a_5^* + i\frac{\pi^2}{V^*}a_6^*\right) \tag{4-25}$$

$$\frac{M^{se}}{-\frac{\dot{z}}{V}} = \frac{1}{2}\rho V^2 B^2\left(a_1^* + i\frac{\pi^2}{V^*}a_4^*\right) \tag{4-26}$$

$$\frac{M^{se}}{\theta} = \frac{1}{2}\rho V^2 B^2\left(a_3^* - i\frac{2\pi}{V^*}a_2^*\right) \tag{4-27}$$

Which are derived from the PoliMi notation of the self-excited forces with flutter derivatives, expressed in equations (1-47) to (1-49).

On the other hand, the six transfer functions of the buffeting forces, written as they appear in the numerical code, derived from equation (1-56), and which the transfer functions of the rheological models are aimed to reproduce, are defined as:

$$\frac{D^{buff}}{\frac{u}{V}} = \frac{1}{2}\rho V^2 B\chi_{Du}^* \tag{4-28}$$

$$\frac{D^{buff}}{\frac{w}{V}} = \frac{1}{2}\rho V^2 B\chi_{Dw}^* \tag{4-29}$$

$$\frac{L^{buff}}{\frac{u}{V}} = \frac{1}{2}\rho V^2 B\chi_{Lu}^* \tag{4-30}$$

$$\frac{L^{buff}}{\frac{w}{V}} = \frac{1}{2}\rho V^2 B \chi^*_{lw} \tag{4-31}$$

$$\frac{M^{buff}}{\frac{u}{V}} = \frac{1}{2}\rho V^2 B^2 \chi^*_{Mu} \tag{4-32}$$

$$\frac{M^{buff}}{\frac{w}{V}} = \frac{1}{2}\rho V^2 B^2 \chi^*_{Mw} \tag{4-33}$$

The identification procedure consists in identifying the number and the type order of systems and the value of the parameters for the selected angle of attack θ_0. Identified the number and the order of rheological systems for the designated transfer function, a cost function is optimized to minimize the residue between the rheological transfer function and the experimental aerodynamic one (equations (4-19) through (4-33)): Starting with the optimization at θ_0=0, subsequently, the other angles of attack are identified imposing a rate of variation to the optimal parameters identified for the angle of attack θ_0=0 and minimizing again the cost function. Naturally, it is a good practice to identify each transfer function using as few rheological models as possible, in order to avoid excessive increase of the degrees of freedom of the overall system.

The identification of the parameters: masses, dampers and springs of the models is performed through a constrained minimization of the mean square deviation between the model transfer function TF_{model} obtained from the rheological models and the corresponding experimental aerodynamic one TF_{aero} (equations (4-19) through (4-33)).

The purpose of the process is therefore the minimization of the objective function:

$$obj = \frac{\sum_{i=1}^{n} \sqrt{Re(TF_{model} - TF_{aero})^2 + Im(TF_{model} - TF_{aero})^2}}{n} \tag{4-34}$$

Where n is the length of the vector of the transfer function.

The introduction of constraints in the minimization procedure is aimed not only at imposing the desired stability margin of individual systems, but also at ensuring congruence with the QSTC: for high values of V^* the TF must converge to zero, being a difference from the linearized QSTC values. The poles of the RM systems must be in the negative part of the complex plane (stability)

and must not be too far from the natural frequencies of the bridge (comparable dynamics). Other constraints could be introduced in the optimization in order to have parameters not so far away from the modal parameters of the bridge and to impose a limit on the rate of variation of the optimal parameters at θ_0=0 when other angles of attack are analyzed. A deeper explanation on the identification procedure is exposed in chapter **Error! Reference source not found.**.

Self-excited forces

Once the parameters of the rheological models have been obtained, and the number of additional degrees of freedom is defined, the rheological models must be coupled with the structural properties of the bridge deck. Subsequently, the global response of the bridge is computed integrating numerically the dynamic equations using a Runge-Kutta classical 4th order solver or Crank-Nicholson and a state-space formulation (discussed in Appendix A).

Thus, an assembly procedure in which the additional degrees of freedom are linked to the bridge deck, and consequently the RM's parameters are gathered with the structural properties of the bridge deck, must take place. Through this assembly procedure, described exhaustively in Appendix A, the global matrices are defined, and it is possible to rewrite the modal equation of motion, given in equation (1-16) and expressed here for practical purposes:

$$[A_{tot}]\dot{\underline{z}} + [B_{tot}]\underline{z} = \underline{0} \tag{4-35}$$

Where the state vector $\underline{z}$ is employed:

$$\underline{z} = \begin{bmatrix} \dot{\underline{x}} \\ \dot{\underline{\eta}} \\ \underline{x} \\ \underline{\eta} \\ \underline{\mu} \end{bmatrix}, \qquad \dot{\underline{z}} = \begin{bmatrix} \ddot{\underline{x}} \\ \ddot{\underline{\eta}} \\ \dot{\underline{x}} \\ \dot{\underline{\eta}} \\ \dot{\underline{\mu}} \end{bmatrix} \tag{4-36}$$

In this way, equation (4-35) is solved with a Runge-Kutta 4th order numerical solver and the time histories of the deck's degrees of freedom $\underline{x}$ and the additional degrees of freedom contained in the rheological models $\underline{\eta}$ and $\underline{\mu}$, are computed. Once this is done, the computation of the difference

motion-induced aerodynamic forces vector $\underline{F_{aero}}_D$ is performed by summing up the forces induced on each of the rheological models of order 0, 1 and 2 i.e. as follows:

$$\underline{F_{aero}^{se}}_D = \underline{F_{aero}^{se,0}}_D + \underline{F_{aero}^{se,1}}_D + \underline{F_{aero}^{se,2}}_D \tag{4-37}$$

Buffeting forces

In contrast to the computation of the difference motion-induced aerodynamic forces, in which the time histories of the additional degrees of freedom are obtained prior to the calculation of the $\underline{F_{aero}}_D$ vector, the buffeting forces are computed right away from the state-space formulation of the problem. The assembly of the global matrices and the derivation of the state-space formulation is described in detail in Appendix A. The equation to be solved is the following:

$$\underline{F_{aero}^{buff}}_D = [A_f]\underline{\dot{z}} + [B_f]\underline{z} + [C_f]\underline{\dot{\psi}} + [D_f]\underline{\psi} \tag{4-38}$$

Where the state vector $\underline{z}$ is:

$$\underline{z} = \begin{bmatrix} \underline{\dot{\eta}} \\ \underline{\eta} \\ \underline{\mu} \end{bmatrix}, \qquad \underline{\dot{z}} = \begin{bmatrix} \underline{\ddot{\eta}} \\ \underline{\dot{\eta}} \\ \underline{\dot{\mu}} \end{bmatrix} \tag{4-39}$$

And the vector $\underline{\psi}$ contains the incoming turbulence:

$$\underline{\psi} = \begin{bmatrix} \psi_u \\ \psi_w \end{bmatrix} = \begin{bmatrix} \underline{u} \\ \overline{V} \\ \underline{w} \\ \overline{V} \end{bmatrix} \tag{4-40}$$

Conclusions

In this thesis we have focused our attention on identifying the problem of non-linearities in the relationship of the aerodynamic forces with the deck's motion, more specifically on the angle of attack α. The buffeting response to turbulent wind was contrasted for the BB3 section with a train and without it. Thus, it was seen that the presence of the train induces a significant non-linear dependence of the aerodynamic forces on α_{LF}. This evidence is expressed in the higher variability of the aerodynamic coefficients in α, starting from the static aerodynamic coefficients and its derivatives, going through the flutter derivatives and the aerodynamic admittance functions. Each of these coefficients was compared to those for the BB3 section alone, and major differences were noticed. In the end, the buffeting response obtained from the forced motion tests exhibited the expected behavior, i.e. and increased dependence on α_{LF}. More specifically, the damping values provided by the flutter derivatives exert a significant influence over the response of the bridge deck, in terms of both motion and aerodynamic forces, at its high frequency band.

In order to account for such non-linearities, the development of a non-linear time-domain method for the prediction of buffeting response of long-span bridges through the definition of several rheological models is proposed. This method represents a new approach for the definition of the non-linear aerodynamic forces providing a revision of the band-superposition concept. The proposed numerical model should be able to describe the non-linearities of both low and high frequency bands in a "one-shot" integration, meaning that all the contributions are modeled and computed within the same integrational time step. Moreover, the compensation provided by the rheological models, coming from the "difference" transfer functions, happened to be in the high frequency band where the fluctuations of the angle of attack are known to be small enough to linearize the problem and apply the superposition principle. Summarizing, the main aspects of the proposed model are the following: no separation of the wind bands, no superposition between LF and HF response, no separated integrations. The choice of developing a method in the time domain

was mandatory to consider all the non-linear issues related to the definition of the aerodynamic forces.

On the other hand, the transfer functions defining the aerodynamic forces, flutter derivatives and admittance functions, are expressed exclusively in the frequency domain, and to reproduce their information in the time domain it was necessary the introduction of rheological models. The identification and tuning procedure of the parameters of the RM can be furtherly discussed.

As part of the IABSE benchmark project, the step 2 (for which this thesis is a part of) intends to perform a numerical validation of sectional models within the wind tunnel. In this thesis, the non-linearities were studied by including a scaled-train to the rigid model, however, in the upcoming steps, the study of the non-linearities have to be extended to the full aeroelastic model.

A future deepening study on the non-linearities of the sectional model under discussion is suggested by validating the proposed numerical model with the experimental records of the forced motion tests. A previous study (Brusamolino 2019) validated a similar numerical model containing rheological models with the buffeting response of the BB3 section without a train obtaining successful results. Thus, a further validation on the non-linear BB3 sectional model is an open issue. It is also interesting to compare the results obtained by the band superposition approach adopted at PoliMi with the developed model.

Appendix A

State-space formulation of the problem

The state-space formulation of the equation of motion (1-16) which includes the degrees of freedom coming from the identified rheological models is here developed. For this aim, global matrices must be assembled in order to write the final form that must be numerically integrated employing the Runge-Kutta 4th order classical solver.

1. Self-excited forces

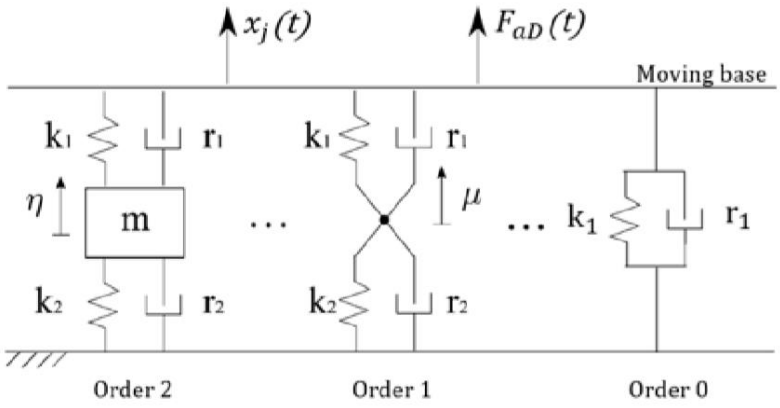

Figure A-1. Rheological models, motion induced forces.

The modal equations of motion are

$$[M_s]\underline{\ddot{x}} + [R_s]\underline{\dot{x}} + [K_s]\underline{x} = \underline{f_x} \tag{A-1}$$

In which $\underline{x} = [y\ z\ \theta]^T$ is the vector containing the modal degrees of freedom of the deck. The forces vector $\underline{f_x}$ is

$$\underline{f_x} = \begin{bmatrix} f_y \\ f_z \\ f_\theta \end{bmatrix} = \begin{bmatrix} \cos(\alpha) & -\sin(\alpha) & 0 \\ \sin(\alpha) & \cos(\alpha) & 0 \\ 0 & 0 & 1 \end{bmatrix} \begin{bmatrix} f_D(\alpha) \\ f_L(\alpha) \\ f_M(\alpha) \end{bmatrix} = [\Lambda]\underline{f_C} \tag{A-2}$$

$$\underline{f_C} = \frac{1}{2}\rho B V_m^2 \begin{bmatrix} 1 & 0 & 0 \\ 0 & 1 & 0 \\ 0 & 0 & B \end{bmatrix} \begin{bmatrix} C_D(\alpha) \\ C_L(\alpha) \\ C_M(\alpha) \end{bmatrix} = [Q] \begin{bmatrix} C_D(\alpha) \\ C_L(\alpha) \\ C_M(\alpha) \end{bmatrix} \tag{A-3}$$

$$\begin{bmatrix} C_D(\alpha) \\ C_L(\alpha) \\ C_M(\alpha) \end{bmatrix} = [L_2]^T \underline{f_2} + [L_1]^T \underline{f_1} + [L_0]^T \underline{f_0} \tag{A-4}$$

In which:

- $\underline{f_2}$ are the forces coming from the 2nd order rheological model;
- $\underline{f_1}$ are the forces coming from the 1st order rheological model;
- $\underline{f_0}$ are the forces coming from the 0 order rheological model.

2nd Order rheological model forces

Assuming that at least one 2nd order rheological model is used at each force component, it can be written:

$$\begin{bmatrix} C_D(\alpha) \\ C_L(\alpha) \\ C_M(\alpha) \end{bmatrix}_2 = \begin{bmatrix} l_{Dy} & 0 & 0 \\ l_{Dz} & 0 & 0 \\ l_{D\theta} & 0 & 0 \\ 0 & l_{Ly} & 0 \\ 0 & l_{Lz} & 0 \\ 0 & l_{L\theta} & 0 \\ 0 & 0 & l_{My} \\ 0 & 0 & l_{Mz} \\ 0 & 0 & l_{M\theta} \end{bmatrix}^T \begin{bmatrix} f_{Dy} \\ f_{Dz} \\ f_{D\theta} \\ f_{Ly} \\ f_{Lz} \\ f_{L\theta} \\ f_{My} \\ f_{Mz} \\ f_{M\theta} \end{bmatrix} = [L_2]^T \underline{f_2} \tag{A-5}$$

Each force component within the $\underline{f_2}$ vector f_{ij}, where $i = D,\ L,\ M$ and $j = y,\ z,\ \theta$, are now given by the rheological models as

$$\underline{f_{ij}} = [K_{ij}]\,\underline{\eta_{ij}} + [R_{ij}]\underline{\dot{\eta}_{ij}} - [K_{ij}]\,\underline{\psi_{ij}} - [R_{ij}]\underline{\dot{\psi}_{ij}} \tag{A-6}$$

$$[\widetilde{M}_{ij}]\,\underline{\ddot{\eta}_{ij}} + [\tilde{R}_{ij}]\underline{\dot{\eta}_{ij}} + [\widetilde{K}_{ij}]\,\underline{\eta_{ij}} - [R_{ij}]\underline{\dot{\psi}_{ij}} - [K_{ij}]\,\underline{\psi_{ij}} = \underline{0} \tag{A-7}$$

In which $\underline{\eta_{ij}}$ is the n x 1 vector (in which n is the number of 2nd order rheological models) of the additional degrees of freedom of the rheological models; $[\widetilde{M}_{ij}]$, $[K_{ij}]$ and $[R_{ij}]$ are n x n diagonal matrices containing the added mass, stiffness and damping parameters obtained from the identification; $[\tilde{R}_{ij}]$, and $[\widetilde{K}_{ij}]$ are n x n diagonal matrices containing the sum of the damping and stiffness coming from the two dashpots and two springs (figure A-1) in each oscillator, respectively; and $\underline{\psi_{ij}}$ is the n x 1 vector of the actual deformation of the rheological systems which is linked to the deck's degrees of freedom through the following expressions

$$\underline{\psi_{ij}} = \underline{l_{ij}}\psi_j \tag{A-8}$$

$$\psi_j = \underline{d_j}^T \underline{\dot{x}} + \underline{e_j^T}\, \underline{x} \tag{A-9}$$

$$\underline{\psi_{ij}} = \underline{d_j}^T \underline{\dot{x}} + \underline{e_j^T}\, \underline{x} \tag{A-10}$$

Where

$$[D] = \left[\underline{D_{iy}}^T \underline{D_{iz}}^T \underline{D_{i\theta}}^T\right] = \begin{bmatrix} -\frac{1}{V} & 0 & 0 \\ 0 & -\frac{1}{V} & 0 \\ 0 & 0 & 0 \end{bmatrix} \tag{A-11}$$

$$[E] = \left[\underline{E_{iy}}^T \underline{E_{iz}}^T \underline{E_{i\theta}}^T\right] = \begin{bmatrix} -\frac{1}{V} & 0 & 0 \\ 0 & -\frac{1}{V} & 0 \\ 0 & 0 & 0 \end{bmatrix} \tag{A-12}$$

Substituting equation (A-10) into equations (A-6) and (A-7), it gives

$$\underline{f_{ij}} = [K_{ij}]\,\underline{\eta_{ij}} + [R_{ij}]\underline{\dot{\eta}_{ij}} - [K_{ij}]\left(\underline{D_{ij}}^T \underline{\dot{x}} + \underline{E_{ij}^T}\, \underline{x}\right) - [R_{ij}]\left(\underline{D_{ij}}^T \underline{\ddot{x}} + \underline{E_{ij}^T}\, \underline{\dot{x}}\right) \tag{A-13}$$

$$[\widetilde{M}_{ij}]\,\underline{\ddot{\eta}_{ij}} + [\tilde{R}_{ij}]\underline{\dot{\eta}_{ij}} + [\widetilde{K}_{ij}]\,\underline{\eta_{ij}} - [R_{ij}]\left(\underline{D_{ij}}^T \underline{\ddot{x}} + \underline{E_{ij}^T}\, \underline{\dot{x}}\right) - [K_{ij}]\left(\underline{D_{ij}}^T \underline{\dot{x}} + \underline{E_{ij}^T}\, \underline{x}\right) = \underline{0} \tag{A-14}$$

Which can be rearranged as

$$\underline{f_{ij}} = [R_{ij}]\underline{\dot{\eta}_{ij}} + [K_{ij}]\,\underline{\eta_{ij}} - [R_{ij}]\underline{D_{ij}}^T \underline{\ddot{x}} - \left([K_{ij}]\underline{D_{ij}}^T + [R_{ij}]\underline{E_{ij}^T}\right)\underline{\dot{x}} - [K_{ij}]\underline{E_{ij}^T}\, \underline{x} \tag{A-15}$$

$$[\widetilde{M}_{ij}]\,\underline{\ddot{\eta}_{ij}} + [\tilde{R}_{ij}]\underline{\dot{\eta}_{ij}} + [\widetilde{K}_{ij}]\,\underline{\eta_{ij}} - [R_{ij}]\underline{D_{ij}}^T \underline{\ddot{x}} - \left([K_{ij}]\underline{D_{ij}}^T + [R_{ij}]\underline{E_{ij}^T}\right)\underline{\dot{x}} - [K_{ij}]\underline{E_{ij}^T}\, \underline{x} = \underline{0} \tag{A-16}$$

By grouping the terms that multiply the $\underline{x}$ vector and its time derivatives

$$\underline{f_{ij}} = [R_{ij}]\underline{\dot{\eta}_{ij}} + [K_{ij}]\,\underline{\eta_{ij}} - [A_{ij}]\underline{\ddot{x}} - [B_{ij}]\underline{\dot{x}} - [C_{ij}]\,\underline{x} \tag{A-17}$$

$$[\widetilde{M}_{ij}]\,\underline{\ddot{\eta}_{ij}} + [\tilde{R}_{ij}]\underline{\dot{\eta}_{ij}} + [\widetilde{K}_{ij}]\,\underline{\eta_{ij}} - [A_{ij}]\underline{\ddot{x}} - [B_{ij}]\underline{\dot{x}} - [C_{ij}]\,\underline{x} = \underline{0} \tag{A-18}$$

Now, considering the whole set of 9 forces and assuming that at least one 2nd order rheological model is used for each force component, the vector of added degrees of freedom is

$$\underline{\eta} = \begin{bmatrix} \underline{\eta_{Dy}} \\ \underline{\eta_{Dz}} \\ \underline{\eta_{D\theta}} \\ \underline{\eta_{Ly}} \\ \underline{\eta_{Lz}} \\ \underline{\eta_{L\theta}} \\ \underline{\eta_{My}} \\ \underline{\eta_{Mz}} \\ \underline{\eta_{M\theta}} \end{bmatrix} \tag{A-19}$$

Equations (A-17) and (A-18) can be rewritten as

$$\underline{f_2} = [R_2]\underline{\dot{\eta}} + [K_2]\underline{\eta} - [A_2]\underline{\ddot{x}} - [B_2]\underline{\dot{x}} - [C_2]\,\underline{x} \tag{A-20}$$

$$[\widetilde{M}_2]\underline{\ddot{\eta}} + [\tilde{R}_2]\underline{\dot{\eta}} + [\widetilde{K}_2]\underline{\eta} - [A_2]\underline{\ddot{x}} - [B_2]\underline{\dot{x}} - [C_2]\,\underline{x} = \underline{0} \tag{A-21}$$

Substituting equation (A-20) into equation (A-4), it is obtained that the global forces produced by the 2nd order rheological model are

$$\underline{f_{x,2}} = [\Lambda][Q][L_2]^T\underline{f_2} \tag{A-22}$$

Hence, the equation of motion (A-1) is rewritten as

$$[M_s]\underline{\ddot{x}} + [R_s]\underline{\dot{x}} + [K_s]\underline{x} = [\Lambda][Q][L_2]^T\left([R_2]\underline{\dot{\eta}} + [K_2]\underline{\eta} - [A_2]\underline{\ddot{x}} - [B_2]\underline{\dot{x}} - [C_2]\underline{x}\right) \tag{A-23}$$

Equations (A-21) and (A-24) can be formulated in matrix form as

$$\begin{bmatrix} [M_s] + [\Lambda][Q][L_2]^T[A_2] & [0] \\ -[A_2] & [\widetilde{M}_2] \end{bmatrix}\begin{bmatrix} \underline{\ddot{x}} \\ \underline{\ddot{\eta}} \end{bmatrix} + \begin{bmatrix} [R_s] + [\Lambda][Q][L_2]^T[B_2] & -[\Lambda][Q][L_2]^T[R_2] \\ -[B_2] & [\tilde{R}_2] \end{bmatrix}\begin{bmatrix} \underline{\dot{x}} \\ \underline{\dot{\eta}} \end{bmatrix} + \begin{bmatrix} [K_s] + [\Lambda][Q][L_2]^T[C_2] & -[\Lambda][Q][L_2]^T[K_2] \\ -[C_2] & [\widetilde{K}_2] \end{bmatrix}\begin{bmatrix} \underline{x} \\ \underline{\eta} \end{bmatrix} = \underline{0} \tag{A-25}$$

Which is simplified as

$$\begin{bmatrix} [M_s]+[M_2^{aero}] & [0] \\ -[A_2] & [\widetilde{M}_2] \end{bmatrix}\begin{bmatrix} \ddot{\underline{x}} \\ \ddot{\underline{\eta}} \end{bmatrix}+\begin{bmatrix} [R_s]+[R_2^{aero}] & [R_\eta^{aero}] \\ -[B_2] & [\tilde{R}_2] \end{bmatrix}\begin{bmatrix} \dot{\underline{x}} \\ \dot{\underline{\eta}} \end{bmatrix} + \begin{bmatrix} [K_s]+[K_2^{aero}] & [K_\eta^{aero}] \\ -[C_2] & [\widetilde{K}_2] \end{bmatrix}\begin{bmatrix} \underline{x} \\ \underline{\eta} \end{bmatrix} = \underline{0} \tag{A-26}$$

1st Order rheological model forces

Following the same approach as for 2nd order rheological forces, the following equations are written

$$\begin{bmatrix} C_D(\alpha) \\ C_L(\alpha) \\ C_M(\alpha) \end{bmatrix}_1 = [L_1]^T \underline{f_1} \tag{A-27}$$

$$\underline{f_{ij}} = [K_{ij}]\,\underline{\mu_{ij}} + [R_{ij}]\underline{\dot{\mu}_{ij}} - [K_{ij}]\,\underline{\psi_{ij}} - [R_{ij}]\underline{\dot{\psi}_{ij}} \tag{A-28}$$

$$[\tilde{R}_{ij}]\underline{\dot{\eta}_{ij}} + [\widetilde{K}_{ij}]\,\underline{\eta_{ij}} - [R_{ij}]\underline{\dot{\psi}_{ij}} - [K_{ij}]\,\underline{\psi_{ij}} = \underline{0} \tag{A-29}$$

In which $\underline{\mu_{ij}}$ is the n x 1 vector (in which n is the number of 1st order rheological models) of the additional degrees of freedom of the rheological models. $\underline{\psi_{ij}}$ is linked to the deck's degrees of freedom through equations (A-8) – (A-12).

$$\underline{f_{ij}} = [R_{ij}]\underline{\dot{\mu}_{ij}} + [K_{ij}]\,\underline{\mu_{ij}} - [A_{ij}]\ddot{\underline{x}} - [B_{ij}]\dot{\underline{x}} - [C_{ij}]\,\underline{x} \tag{A-30}$$

$$[\tilde{R}_{ij}]\underline{\dot{\mu}_{ij}} + [\widetilde{K}_{ij}]\,\underline{\mu_{ij}} - [A_{ij}]\ddot{\underline{x}} - [B_{ij}]\dot{\underline{x}} - [C_{ij}]\,\underline{x} = \underline{0} \tag{A-31}$$

Considering the whole set of 9 forces and assuming that at least one 1st order rheological model is used for each force component, the vector of added degrees of freedom is

$$\underline{\mu} = \begin{bmatrix} \underline{\mu_{Dy}} \\ \underline{\mu_{Dz}} \\ \underline{\mu_{D\theta}} \\ \underline{\mu_{Ly}} \\ \underline{\mu_{Lz}} \\ \underline{\mu_{L\theta}} \\ \underline{\mu_{My}} \\ \underline{\mu_{Mz}} \\ \underline{\mu_{M\theta}} \end{bmatrix} \tag{A-32}$$

So that equations (A-30) and (A-31) can be rewritten as

$$\underline{f_1} = [R_1]\underline{\dot{\mu}} + [K_1]\underline{\mu} - [A_1]\ddot{\underline{x}} - [B_1]\dot{\underline{x}} - [C_1]\,\underline{x} \tag{A-33}$$

$$[\tilde{R}_1]\underline{\dot{\mu}} + [\tilde{K}_1]\underline{\mu} - [A_1]\underline{\ddot{x}} - [B_1]\underline{\dot{x}} - [C_1]\,\underline{x} = \underline{0} \tag{A-34}$$

Substituting equation (A-33) into equation (A-4), it is obtained that the global forces produced by the 1st order rheological model are

$$\underline{f}_{x,1} = [\Lambda][Q][L_1]^T \underline{f}_1 \tag{A-35}$$

Equations (A-34) and the equation of motion (A-1) can be formulated in matrix form as

$$\begin{aligned}\begin{bmatrix}[M_s] + [\Lambda][Q][L_1]^T[A_1] & [0] \\ -[A_1] & [0]\end{bmatrix}\begin{bmatrix}\underline{\ddot{x}} \\ \underline{\ddot{\mu}}\end{bmatrix} \\ + \begin{bmatrix}[R_s] + [\Lambda][Q][L_1]^T[B_1] & -[\Lambda][Q][L_1]^T[R_1] \\ -[B_1] & [\tilde{R}_1]\end{bmatrix}\begin{bmatrix}\underline{\dot{x}} \\ \underline{\dot{\mu}}\end{bmatrix} \\ + \begin{bmatrix}[K_s] + [\Lambda][Q][L_1]^T[C_1] & -[\Lambda][Q][L_1]^T[K_1] \\ -[C_1] & [\tilde{K}_1]\end{bmatrix}\begin{bmatrix}\underline{x} \\ \underline{\mu}\end{bmatrix} = \underline{0}\end{aligned} \tag{A-36}$$

Which is simplified as

$$\begin{aligned}\begin{bmatrix}[M_s] + [M_1^{aero}] & [0] \\ -[A_1] & [0]\end{bmatrix}\begin{bmatrix}\underline{\ddot{x}} \\ \underline{\ddot{\mu}}\end{bmatrix} + \begin{bmatrix}[R_s] + [R_1^{aero}] & [R_\mu^{aero}] \\ -[B_1] & [\tilde{R}_1]\end{bmatrix}\begin{bmatrix}\underline{\dot{x}} \\ \underline{\dot{\mu}}\end{bmatrix} \\ + \begin{bmatrix}[K_s] + [K_1^{aero}] & [K_\mu^{aero}] \\ -[C_1] & [\tilde{K}_1]\end{bmatrix}\begin{bmatrix}\underline{x} \\ \underline{\mu}\end{bmatrix} = \underline{0}\end{aligned} \tag{A-37}$$

0 Order rheological model forces

Following the same approach as for 2nd and 1st order rheological forces, the following equations are written

$$\begin{bmatrix}C_D(\alpha) \\ C_L(\alpha) \\ C_M(\alpha)\end{bmatrix}_0 = [L_0]^T\,\underline{f}_0 \tag{A-38}$$

$$\underline{f}_{ij} = -[K_{ij}]\,\underline{\psi}_{ij} - [R_{ij}]\underline{\dot{\psi}}_{ij} \tag{A-39}$$

In which no additional degrees of freedom are inserted in the model and $\underline{\psi}_{ij}$ is linked to the deck's degrees of freedom through equations (A-8) – (A-12).

$$\underline{f}_{ij} = -[A_{ij}]\underline{\ddot{x}} - [B_{ij}]\underline{\dot{x}} - [C_{ij}]\,\underline{x} \tag{A-40}$$

Considering the whole set of 9 forces and assuming that at least one 2nd order rheological model is used for each force component, equation (A-40) is rewritten as

$$\underline{f_0} = -[A_0]\underline{\ddot{x}} - [B_0]\underline{\dot{x}} - [C_0]\,\underline{x} \tag{A-41}$$

Substituting equation (A-41) into equation (A-4), it is obtained that the global forces produced by the 2nd order rheological model are

$$\underline{f_{x,0}} = [\Lambda][Q][L_1]^T\underline{f_0} \tag{A-42}$$

The equation of motion is then rewritten as

$$[[M_s] + [\Lambda][Q][L_1]^T[A_0]]\underline{\ddot{x}} + [[R_s] + [\Lambda][Q][L_1]^T[B_0]]\underline{\dot{x}} + [[K_s] + [\Lambda][Q][L_1]^T[C_0]]\underline{x} = \underline{0} \tag{A-43}$$

Which is simplified as

$$[M_s + [M_0^{aero}]]\underline{\ddot{x}} + [R_s + [R_0^{aero}]]\underline{\dot{x}} + [K_s + [K_0^{aero}]]\underline{x} = \underline{0} \tag{A-44}$$

In conclusion, the forces of each rheological model are summed up and equations (A-26), (A-37), and (A-44) are arranged into a single matrix equation:

$$\begin{aligned}
&\begin{bmatrix} [M_s] + [M_0^{aero}] + [M_1^{aero}] + [M_2^{aero}] & [0] & [0] \\ -[A_2] & [\widetilde{M}_2] & [0] \\ -[A_1] & [0] & [0] \end{bmatrix}\begin{bmatrix} \underline{\ddot{x}} \\ \underline{\ddot{\eta}} \\ \underline{\ddot{\mu}} \end{bmatrix} \\
&+\begin{bmatrix} [R_s] + [R_0^{aero}] + [R_1^{aero}] + [R_2^{aero}] & -[R_\eta^{aero}] & -[R_\mu^{aero}] \\ -[B_2] & [\tilde{R}_2] & [0] \\ -[B_1] & [0] & [\tilde{R}_1] \end{bmatrix}\begin{bmatrix} \underline{\dot{x}} \\ \underline{\dot{\eta}} \\ \underline{\dot{\mu}} \end{bmatrix} \\
&+\begin{bmatrix} [K_s] + [K_0^{aero}] + [K_1^{aero}] + [K_2^{aero}] & -[K_\eta^{aero}] & -[K_\mu^{aero}] \\ -[C_2] & [\widetilde{K}_2] & [0] \\ -[C_1] & [0] & [\widetilde{K}_1] \end{bmatrix}\begin{bmatrix} \underline{x} \\ \underline{\eta} \\ \underline{\mu} \end{bmatrix} = \underline{0}
\end{aligned} \tag{A-45}$$

The *state vector* $\underline{z}$ is now defined:

$$\underline{z} = \begin{bmatrix} \underline{\dot{x}} \\ \underline{\dot{\eta}} \\ \underline{x} \\ \underline{\eta} \\ \underline{\mu} \end{bmatrix}, \qquad \underline{\dot{z}} = \begin{bmatrix} \underline{\ddot{x}} \\ \underline{\ddot{\eta}} \\ \underline{\dot{x}} \\ \underline{\dot{\eta}} \\ \underline{\dot{\mu}} \end{bmatrix} \tag{A-46}$$

So that equation (A-45) is rearranged into

$$\begin{bmatrix} [\tilde{M}_s] & [0] & [0] & [0] & -[R_\mu^{aero}] \\ -[A_2] & [\tilde{M}_2] & [0] & [0] & [0] \\ [0] & [0] & [I] & [0] & [0] \\ [0] & [0] & [0] & [I] & [0] \\ -[A_1] & [0] & [0] & [0] & [\tilde{R}_1] \end{bmatrix} \begin{bmatrix} \ddot{\underline{x}} \\ \ddot{\underline{\eta}} \\ \dot{\underline{x}} \\ \dot{\underline{\eta}} \\ \dot{\underline{\mu}} \end{bmatrix}$$

$$+ \begin{bmatrix} [\tilde{R}_s] & -[R_\eta^{aero}] & [\tilde{K}_s] & -[K_\eta^{aero}] & -[K_\mu^{aero}] \\ -[B_2] & [\tilde{R}_2] & -[C_2] & [\tilde{K}_2] & [0] \\ -[I] & [0] & [0] & [0] & [0] \\ [0] & -[I] & [0] & [0] & [0] \\ -[B_1] & [0] & -[C_1] & [0] & [\tilde{K}_1] \end{bmatrix} \begin{bmatrix} \dot{\underline{x}} \\ \dot{\underline{\eta}} \\ \underline{x} \\ \underline{\eta} \\ \underline{\mu} \end{bmatrix} \tag{A-47}$$

$$= \underline{0}$$

At last, the state-space formulation of the problem is summarized as:

$$[A_{tot}]\dot{\underline{z}} + [B_{tot}]\underline{z} = \underline{0} \tag{A-48}$$

2. Buffeting forces

With a similar approach as for the self-excited forces, the state-space formulation of the buffeting forces is presented. Equations (A-2) through (A-4) remain the same. The number of degrees of freedom to which the fictitious rheological models are connected to the real problem are in this case 2 (u and w components of the wind speed) instead as 3 (y, z and θ) for the case of the self-excited forces. Hence, the definition of the $[L]^T$ matrices and $\underline{f}$ vector will be different.

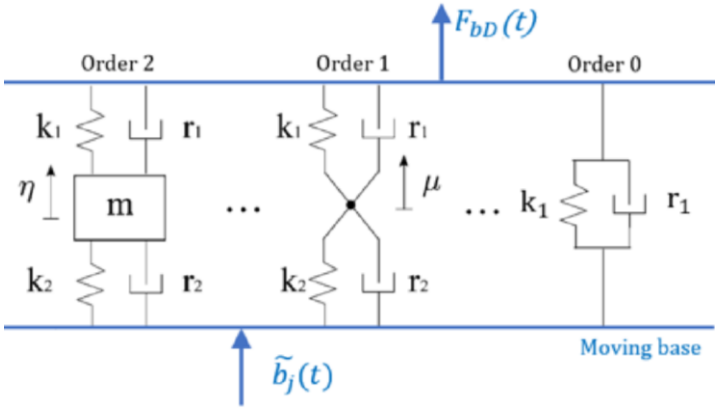

Figure A-2. Rheological models, motion induced forces.

2nd Order rheological model forces

Assuming that at least one 2nd order rheological model is used at each force component, it can be written:

$$\begin{bmatrix} C_D(\alpha) \\ C_L(\alpha) \\ C_M(\alpha) \end{bmatrix}_2 = \begin{bmatrix} l_{Du} & 0 & 0 \\ l_{Dw} & 0 & 0 \\ 0 & l_{Lu} & 0 \\ 0 & l_{Lw} & 0 \\ 0 & 0 & l_{Mu} \\ 0 & 0 & l_{M\theta} \end{bmatrix}^T \begin{bmatrix} f_{Du} \\ f_{Dw} \\ f_{Lu} \\ f_{Lw} \\ f_{Mu} \\ f_{Mw} \end{bmatrix} = [L_2]^T \underline{f_2} \tag{A-49}$$

Each force component f_{ij} within the $\underline{f_2}$ vector, where $i = D,\ L,\ M$ and $j = u,\ w$, are now given by the rheological models as

$$\underline{f_{ij}} = [K_{ij}]\,\underline{\eta_{ij}} + [R_{ij}]\underline{\dot{\eta}_{ij}} - [K_{ij}]\,\underline{\psi_{ij}} - [R_{ij}]\underline{\dot{\psi}_{ij}} \tag{A-50}$$

$$[\widetilde{M}_{ij}]\,\underline{\ddot{\eta}_{ij}} + [\tilde{R}_{ij}]\underline{\dot{\eta}_{ij}} + [\widetilde{K}_{ij}]\,\underline{\eta_{ij}} - [R_{ij}]\underline{\dot{\psi}_{ij}} - [K_{ij}]\,\underline{\psi_{ij}} = \underline{0} \tag{A-51}$$

In which $\underline{\eta_{ij}}$ is the n x 1 vector (where n is the number of 2nd order rheological models) of the additional degrees of freedom of the rheological models; $[\widetilde{M}_{ij}]$, $[K_{ij}]$ and $[R_{ij}]$ are n x n diagonal matrices containing the added mass, stiffness and damping parameters obtained from the identification; $[\tilde{R}_{ij}]$, and $[\widetilde{K}_{ij}]$ are n x n diagonal matrices containing the sum of the damping and stiffness coming from the two dashpots and two springs (figure A-2) in each oscillator, respectively; and $\underline{\psi_{ij}}$ is the n x 1 vector of the actual deformation of the rheological systems which is linked to the u and w wind speed components through the following expressions

$$\underline{\tilde{\psi}} = \begin{bmatrix} \underline{\psi_{Du}} \\ \underline{\psi_{Dw}} \\ \underline{\psi_{Lu}} \\ \underline{\psi_{Lw}} \\ \underline{\psi_{Mu}} \\ \underline{\psi_{Mw}} \end{bmatrix} = \begin{bmatrix} l_{Du} & 0 \\ 0 & l_{Dw} \\ l_{Lu} & 0 \\ 0 & l_{Lw} \\ l_{Mu} & 0 \\ 0 & l_{Mw} \end{bmatrix} \begin{bmatrix} \psi_u \\ \psi_w \end{bmatrix} = [L_\psi]\underline{\psi} \tag{A-52}$$

$$\psi_u = \frac{u}{V}, \qquad \psi_w = \frac{w}{V} \tag{A-53}$$

Considering the whole set of 6 forces and assuming that at least one 2nd order rheological model is used for each force component, the vector of added degrees of freedom is

$$\underline{\eta} = \begin{bmatrix} \underline{\eta_{Du}} \\ \underline{\eta_{Dw}} \\ \underline{\eta_{Lu}} \\ \underline{\eta_{Lw}} \\ \underline{\eta_{Mu}} \\ \underline{\eta_{Mw}} \end{bmatrix} \tag{A-54}$$

Equations (A-50) and (A-51) can be rewritten as

$$\underline{f_2} = [R_2]\underline{\dot{\eta}} + [K_2]\underline{\eta} - [R_2][L_\psi]\underline{\dot{\psi}} - [K_2][L_\psi]\,\underline{\psi} \tag{A-55}$$

$$\left[\widetilde{M}_2\right]\underline{\ddot{\eta}} + [\tilde{R}_2]\underline{\dot{\eta}} + \left[\widetilde{K}_2\right]\underline{\eta} - [R_2][L_\psi]\underline{\dot{\psi}} - [K_2][L_\psi]\,\underline{\psi} = \underline{0} \tag{A-56}$$

Which are simplified as

$$\underline{f_2} = [R_2]\underline{\dot{\eta}} + [K_2]\underline{\eta} - \left[R_{2\psi}\right]\underline{\dot{\psi}} - [K_{2\psi}]\,\underline{\psi} \tag{A-57}$$

$$\left[\widetilde{M}_2\right]\underline{\ddot{\eta}} + [\tilde{R}_2]\underline{\dot{\eta}} + \left[\widetilde{K}_2\right]\underline{\eta} - \left[R_{2\psi}\right]\underline{\dot{\psi}} - [K_{2\psi}]\,\underline{\psi} = \underline{0} \tag{A-58}$$

Substituting equation (A-55) into equation (A-4), it is obtained that the global forces produced by the 2nd order rheological model are

$$\underline{f_{x,2}} = [\Lambda][Q][L_2]^T\underline{f_2} \tag{A-59}$$

1st Order rheological model forces

Following the same approach as for 2nd order rheological forces, the following equations are written

$$\begin{bmatrix} C_D(\alpha) \\ C_L(\alpha) \\ C_M(\alpha) \end{bmatrix}_1 = [L_1]^T\,\underline{f_1} \tag{A-60}$$

$$\underline{f_{ij}} = \left[K_{ij}\right]\underline{\mu_{ij}} + \left[R_{ij}\right]\underline{\dot{\mu}_{ij}} - \left[K_{ij}\right]\underline{\psi_{ij}} - \left[R_{ij}\right]\underline{\dot{\psi}_{ij}} \tag{A-61}$$

$$\left[\tilde{R}_{ij}\right]\underline{\dot{\eta}_{ij}} + \left[\widetilde{K}_{ij}\right]\underline{\eta_{ij}} - \left[R_{ij}\right]\underline{\dot{\psi}_{ij}} - \left[K_{ij}\right]\underline{\psi_{ij}} = \underline{0} \tag{A-62}$$

In which $\underline{\mu_{ij}}$ is the n x 1 vector (in which n is the number of 1st order rheological models) of the additional degrees of freedom of the rheological models. $\underline{\psi_{ij}}$ is linked to the u and w wind velocity components through equations (A-52) – (A-53). Considering the whole set of 6 forces and assuming

that at least one 1st order rheological model is used for each force component, the vector of added degrees of freedom is

$$\underline{\mu} = \begin{bmatrix} \underline{\mu_{Du}} \\ \underline{\mu_{Dw}} \\ \underline{\mu_{Lu}} \\ \underline{\mu_{Lw}} \\ \underline{\mu_{Mu}} \\ \underline{\mu_{Mw}} \end{bmatrix} \tag{A-63}$$

So that equations (A-63) and (A-64) can be rewritten as

$$\underline{f_1} = [R_1]\underline{\dot{\mu}} + [K_1]\underline{\mu} - [R_{1\psi}]\underline{\dot{\psi}} - [K_{1\psi}]\,\underline{\psi} \tag{A-64}$$

$$[\tilde{R}_1]\underline{\dot{\mu}} + [\tilde{K}_1]\underline{\mu} - [R_{1\psi}]\underline{\dot{\psi}} - [K_{1\psi}]\,\underline{\psi} = \underline{0} \tag{A-65}$$

Substituting equation (A-66) into equation (A-4), it is obtained that the global forces produced by the 1st order rheological model are

$$\underline{f_{x,1}} = [\Lambda][Q][L_1]^T \underline{f_1} \tag{A-66}$$

0 Order rheological model forces

Following the same approach as for 2nd order rheological forces, the following equations are written

$$\begin{bmatrix} C_D(\alpha) \\ C_L(\alpha) \\ C_M(\alpha) \end{bmatrix}_0 = [L_0]^T f_0 \tag{A-67}$$

$$\underline{f_{ij}} = -[K_{ij}]\,\underline{\psi_{ij}} - [R_{ij}]\underline{\dot{\psi}_{ij}} \tag{A-68}$$

In which no additional degrees of freedom are inserted in the model and $\underline{\psi_{ij}}$ is linked to the u and w wind velocity components through equation (A-52) – (A-53) so that equations (A-68) can be rewritten as

$$\underline{f_0} = -[R_{0\psi}]\underline{\dot{\psi}} - [K_{0\psi}]\,\underline{\psi} \tag{A-69}$$

Substituting equation (A-69) into equation (A-4), it is obtained that the global forces produced by the 0 order rheological models are

$$\underline{f_{x,0}} = [\Lambda][Q][L_0]^T \underline{f_0} \tag{A-70}$$

In conclusion, equations (A-58) and (A-66) can be arranged as

$$\begin{bmatrix}[\widetilde{M}_2] & [0]\\ [0] & [0]\end{bmatrix}\begin{bmatrix}\underline{\ddot{\eta}}\\ \underline{\ddot{\mu}}\end{bmatrix}+\begin{bmatrix}[\tilde{R}_2] & [0]\\ [0] & [\tilde{R}_1]\end{bmatrix}\begin{bmatrix}\underline{\dot{\eta}}\\ \underline{\dot{\mu}}\end{bmatrix}+\begin{bmatrix}[\widetilde{K}_2] & [0]\\ [0] & [\widetilde{K}_1]\end{bmatrix}\begin{bmatrix}\underline{\eta}\\ \underline{\mu}\end{bmatrix}=\begin{bmatrix}[R_{2\psi}]\underline{\dot{\psi}}+[K_{2\psi}]\,\underline{\psi}\\ [R_{1\psi}]\underline{\dot{\psi}}+[K_{1\psi}]\,\underline{\psi}\end{bmatrix} \tag{A-71}$$

Introducing the *state-vector* $\underline{z}$

$$\underline{z}=\begin{bmatrix}\underline{\dot{\eta}}\\ \underline{\eta}\\ \underline{\mu}\end{bmatrix},\qquad \underline{\dot{z}}=\begin{bmatrix}\underline{\ddot{\eta}}\\ \underline{\dot{\eta}}\\ \underline{\dot{\mu}}\end{bmatrix} \tag{A-72}$$

Equation (A-71) can be rewritten

$$\begin{bmatrix}[\widetilde{M}_2] & [0] & [0]\\ [0] & [I] & [0]\\ [0] & [0] & [\tilde{R}_1]\end{bmatrix}\begin{bmatrix}\underline{\ddot{\eta}}\\ \underline{\dot{\eta}}\\ \underline{\dot{\mu}}\end{bmatrix}+\begin{bmatrix}[\tilde{R}_2] & [\widetilde{K}_2] & [0]\\ -[I] & [0] & [0]\\ [0] & [0] & [\widetilde{K}_1]\end{bmatrix}\begin{bmatrix}\underline{\dot{\eta}}\\ \underline{\eta}\\ \underline{\mu}\end{bmatrix}=\begin{bmatrix}[R_{2\psi}]\\ [0]\\ [R_{1\psi}]\end{bmatrix}\underline{\dot{\psi}}+\begin{bmatrix}[K_{2\psi}]\\ [0]\\ [K_{1\psi}]\end{bmatrix}\underline{\psi} \tag{A-73}$$

Recalling equation (A-4)

$$\begin{aligned}\underline{f_x}&=[\Lambda][Q][L_2]^T\underline{f_2}+[\Lambda][Q][L_1]^T\underline{f_1}+[\Lambda][Q][L_0]^T\underline{f_0}\\ &=[\Lambda][Q]([L_2]^T[R_2]\underline{\dot{\eta}}+[L_2]^T[K_2]\underline{\eta}-[L_2]^T[R_{2\psi}]\underline{\dot{\psi}}-[L_2]^T[K_{2\psi}]\underline{\psi}\\ &\quad+[L_1]^T[R_1]\underline{\dot{\mu}}+[L_1]^T[K_1]\underline{\mu}-[L_1]^T[R_{1\psi}]\underline{\dot{\psi}}-[L_1]^T[K_{1\psi}]\underline{\psi}\\ &\quad-[L_0]^T[R_{0\psi}]\underline{\dot{\psi}}-[L_0]^T[K_{0\psi}]\,\underline{\psi})\end{aligned} \tag{A-74}$$

$$\begin{aligned}&\underline{f_x}\\ &=[\Lambda][Q]\Bigg([[0]\quad[L_2]^T[R_2]\quad[L_1]^T[R_1]]\underline{\dot{z}}+[[0]\quad[L_2]^T[K_2]\quad[L_1]^T[K_1]]\underline{z}\\ &-\begin{bmatrix}[L_2]^T[R_{2\psi}]+[L_1]^T[R_{1\psi}]+[L_0]^T[R_{0\psi}] & [L_2]^T[K_{2\psi}]+[L_1]^T[K_{1\psi}]+[L_0]^T[K_{0\psi}]\end{bmatrix}\begin{bmatrix}\underline{\dot{\psi}}\\ \underline{\psi}\end{bmatrix}\Bigg)\end{aligned} \tag{A-75}$$

Simplifying equation (A-75), the state-space formulation of the buffeting forces is obtained with its global matrices:

$$\underline{f_x}=[A_f]\underline{\dot{z}}+[B_f]\underline{z}+[C_f]\underline{\dot{\psi}}+[D_f]\underline{\psi} \tag{A-76}$$

Bibliography

A. Jain, N.P. Jones, RH. Scanlan. "Coupled aeroelastic and aerodynamic response of long-span bridges." *Journal of Wind Engineering and Industrial Aerodynamics*, 1996: 60:69-80.

A. Pellegri, A. Tornielli. "A Frequency Domain Method for Buffeting Analysis of Long-Span Bridges." *Politesi. Archivio digitale delle tesi di laurea e di dottorato* (Politecnico di Milano), 2017.

Brusamolino, A. "A Time-Domain Approach Based on Rheological Models for he Buffeting Response of Long-Span bridges." *Politesi. Archivio difitale delle tesi di laurea e di dottorato*, 2019.

G. Diana, D. Rocchi, T. Argentini. "An experimental validation of a band superposition model of the aerodynamic forces acting on multi-box deck sections." *Journal of Wind Engineering and Industrial Aerodynamics*, 2013: 113:40-58.

G. Diana, D. Rocchi, T. Argentini, and S. Muggiasca. "Aerodynamic instability of a bridge deck section model: linear and non-linear approach to force modeling." *Journal of Wind Engineering and Industrial Aerodynamics*, 2010: 98:363-374.

G. Diana, F. Cheli, A. Collina, A. Zasso, and J.M. Brownjohn. "Suspension bridge parameter identification in full scale test." *8th ICWE Conf.* London, Ontario, 1991.

G. Diana, F. Resta, A. Zasso, M. Belloli, and D. Rocchi. "Forced motion and free motion aeroelastic tests on a newconcept dynamometric section model of the Messina suspension bridge." *Journal of Wind Engineering and Industrial Aerodynamics*, 2004: 92:441-462.

G. Diana, F. Resta, and D. Rocchi. "A new numerical approach to reproduce bridge aerodynamic non-linearities in time domain." *Journal of Wind Engineering and Industrial Aerodynamics*, 2008: 96:1871-1884.

G. Diana, M. Falco, S. Bruni, A. Cigada, G.L. Larose, A. Damsgaard, and A. Collina. "Comparisons between wind tunnel tests on a full aeroelastic model of the proposed bridge over stretto di Messina and numerical results." (Journal of Wind Engineering and Industrial Aerodynamics) 1995: 54-55:101-113.

G. Diana, S. Bruni, D. Rocchi. "A numerical and experimental investigation on aerodynamic non-linearities in bridge response to turbulent wind." *EACWE 4*. Prague, 11-15 July 2005.

G. Diana, S. Omarini. "A non-linear method to compute the buffeting response of a bridge. Validation of the model through wind tunnel tests." *Journal of Wind Engineering and Industrial Aerodynamics*, n.d.

"http://www.wintunnel.polimi.it/facility." *PoliMi Wind Tunnel.* n.d.

N.N. Minh, T. Miyata, H. Yamada, Y. Sanada. "Numerical simulation of wind turbulence and buffeting analysis of long span bridges." *Journal of Wind Engineering and Industrial Aerodynamics*, 1999: 83:301-315.

X. Chen, A. Kareem. "New frontiers in aerodynamic tayloring of long span bridges: an advanced analysis framework." *Journal of Wind Engineering and Industrial Aerodynamics*, 2003: 91:1511-1528.

Zasso, A. "Flutter derivatives: Advantages of a new representation convention." *Journal of Wind Engineering and Industrial Aerodynamics*, 1996: 60:35-47.

Acknowledgements

In the first place, some special words of gratitude go to professor Daniele Rocchi who allowed me to develop this thesis, and for all the teachings and knowledge that this work has given me. My special gratitude as well goes to Dott. Tommaso Argentini and Simone Omarini, for your patience and support on this work and the words of advice you have provided me.

I would like to thank my group of colleagues that rapidly became my friends for being present all these years in my journey at Politecnico di Milano, spending moments of laughter and hard work together. You made these years more exciting!

At last, but not least, I want to thank my family for being at my side in every moment and supporting me unconditionally in this project. Certainly, the unusual moments in which I have written this thesis during the lockdown has been confusing, but gave me the chance to work on it by your side.